Effects of Crystallographic Texture and Applied Strain Rate on the Cyclic Behavior of Nickel-Titanium

by

Kyubum Kim

A dissertation submitted in partial fulfillment
of the requirements for the degree of
Doctor of Philosophy
(Mechanical Engineering)
in the University of Michigan
2013

Doctoral Committee:
Assistant Professor Samantha Hayes Daly, Chair
Professor J. Wayne Jones
Assistant Professor Jason P. McCormick
Professor Jwo Pan
Professor John A. Shaw

Acknowledgements

First, I would like to extend a very sincere thanks to my advisor, Professor Samantha Daly for her support and guidance throughout this program. Thanks to my colleagues, Benjamin Reedlunn, Adam Kammers, Michael Kimiecik, Jared Tracy, Jason Geathers, and Joyce Gong whose support was pivotal to its completion. I would like to acknowledge Professor John Shaw and Ellen Arruda for facilitating the completion of this dissertation.

I gratefully acknowledge the financial support of the US Department of Energy, Office of Basic Energy Sciences (contract No. DE-SC0003996 monitored by Dr. John Vetrano), who funded the experiments and analysis detailed in this thesis. I also thank the Horace J. Rackham School of Graduate Studies and the University of Michigan for the start-up funding that allowed the initiation of this work in 2009.

I would like to thank to my friends, Jeongyong Choi and In-ho Lee, I cannot have done this without you.

Lastly, special thanks to my family, especially to my wife, Ok Jae Lee for her sincere dedication and emotional support throughout this program.

Table of Contents

List of Tables

Table

List of Figures

Figure

Abstract

Shape memory alloys (SMAs) are utilized in a wide range of applications due to their unique characteristics, most notably the shape memory effect and superelasticity. In spite of intensive research, much is still unknown about the solid-to-solid, diffusionless phase transformation from a cubic austenite phase to a monoclinic martensite phase that is responsible for these properties, and the complex thermo-mechanical interactions that accompany this transformation. The aim of this research was to characterize this phase transformation during displacement-controlled cyclic loading in superelastic nickel-titanium (also known as Nitinol or NiTi), which is the most commonly utilized SMA, with a focus on the effect of globally applied strain rate and crystallographic texture. Experimental studies of thin sheet specimens of polycrystalline NiTi under uniaxial tensile loading were conducted using a combination of digital image correlation (strain fields) and infrared thermography (thermal fields). Specimens were prepared along directions oriented 0° (RD), 45°, and 90° (TD) to the rolling direction of the sheet and subjected to fifty cycles at prescribed strain rates of 10^{-4}, 10^{-3}, and 10^{-2} s^{-1}.

A strong cycle-to-cycle strain similarity was found in the martensite, indicating that local elastic stress fields are driven by a dislocation structure and martensitic nuclei that largely stabilize during the first loading cycle. This cyclic similarity increased when the crystallographic orientation of the test specimen was less favorable for phase transformation. It was also found that on loading, these unfavorably oriented specimens accommodated less axial strain inside the

martensitic deformation band and more axial strain outside of the band. Unfavorable textures also resulted in the nucleation of more martensitic bands, and this became increasingly apparent at faster applied strain rates. At an applied strain rate of 10^{-2} s^{-1}, the cyclic behavior exhibited significantly greater transformation homogeneity and accumulated more latent heat, which affected the macroscopic response between cycles. Thus, testing at 10^{-2} s^{-1} was performed with a 1800 second hold between cycles in order to examine the effect of accumulated latent heat. Other parameters including the evolution of martensite volume fraction and velocity of the bands were examined with respect to strain rate and specimen crystallographic texture.

Chapter 1

Introduction

Smart materials such as shape memory alloys, shape memory polymers, and magnetostrictive and piezoelectric materials are used in a wide range of applications because of their unique characteristics. Among them, shape memory alloys (SMAs) have been intensively studied because of their high work density and their *shape memory* and *superelastic* capabilities. The shape memory effect refers to the reversion of a SMA to its original shape after deformation and subsequent heating of the alloy to above a specified transition temperature. Superelasticity is the ability of a SMA to recover large amounts of strain through solid to solid, diffusionless phase transformation when loading and unloading above a specified transition temperature.

Many superelastic applications require SMAs to be subjected to cyclic loading at varied applied strain rates. In addition, the crystallographic texture of the specimen (i.e., the preferred crystallographic orientation of the sample incurred by standard processes like drawing or rolling) can significantly impact material behavior, such as the amplitude of the stress plateau and the amount of recoverable strain. In order to use the superelastic properties of Nitinol successfully, it is critical to understand the effect of cycling, applied strain rate, and crystallographic texture on the thermo-mechanical behavior of NiTi during stress-induced martensitic phase transformation.

1.1 Motivation

In spite of intensive research for more than 50 years, much is still unknown about the complex local thermo-mechanical interactions that underlie phase transformation in SMAs. The ambient and local temperature, applied strain rate, cycling, and crystallographic texture show complex interactions with each other that are reflected in the macroscopic behavior. Because phase transformation results in large localized deformations, it is important to examine the spatial distribution of transformation as well as the averaged macroscopic stress-strain response. Until recently, the quantitative examination of phase transformation across relatively large fields of view has been difficult due to experimental limitations. Recently, this has become possible by the application of digital image correlation (DIC) to map transformation [1]. DIC is an *in-situ* optical technique used to quantify surface displacements by marker tracking. The full-field strain map obtained by DIC allows the quantitative characterization of the nucleation and propagation of the stress-induced martensitic phase transformation by tracking localized regions of high strain. Here, we utilize a combination of simultaneous full-field strain mapping by stereo digital image correlation (DIC) and full-field thermal mapping by infrared thermography in order to examine stress-induced martensitic phase transformation and its dependence on cycling, applied strain rate, and crystallographic texture. In addition, the interaction between latent heat and the extent of transformation is observed by overlaying infrared thermography with local strain values. This approach enables investigation of transformation characteristics including the relation between local strain and temperature during phase transformation, and how factors such as the cycling, strain rate, latent heat and texture affect the phase transformation.

1.2 Background on Shape Memory Alloys

Three crystallographic phases, termed austenite (A), martensite (M), and R-phase (R), play a significant role in the phase transformation underlying the shape memory effect and superelasticity, as shown schematically in figure 1-1. Austenite has a B2 cubic crystal structure, which is highly symmetric and is stable at high temperatures and low stresses. Martensite has a B19' monoclinic crystal structure, which has lower symmetry and is stable at low temperatures and high stresses. There are 12 correspondence variants of martensite arising from the relationship between the different symmetries of the cubic and monoclinic structures [2]. Additionally, twinned martensite and detwinned martensite can exist, as described by thermal-M and oriented-M in figure 1-1, respectively. The R-phase is an intermediate state and a rhombohedral distortion of the B2 cubic austenite that occurs in some transformations.

The favorable crystallographic phase at a given stress and ambient temperature is determined by the critical transformation temperatures of the material. Because the phase transformation is first order, these can be measured by differential scanning calorimetry (DSC) as shown in figure 1-2 [3]. DSC monitors the heat flow rate to/from a sample in a pan versus an empty reference pan at a constant thermal scanning rate. The vertical axis in figure 1-2 is converted to specific heat. Above the austenite finish temperature (A_f) during heating, austenite is the preferred phase; during cooling below martensite finish temperature (M_f), martensite is preferential.

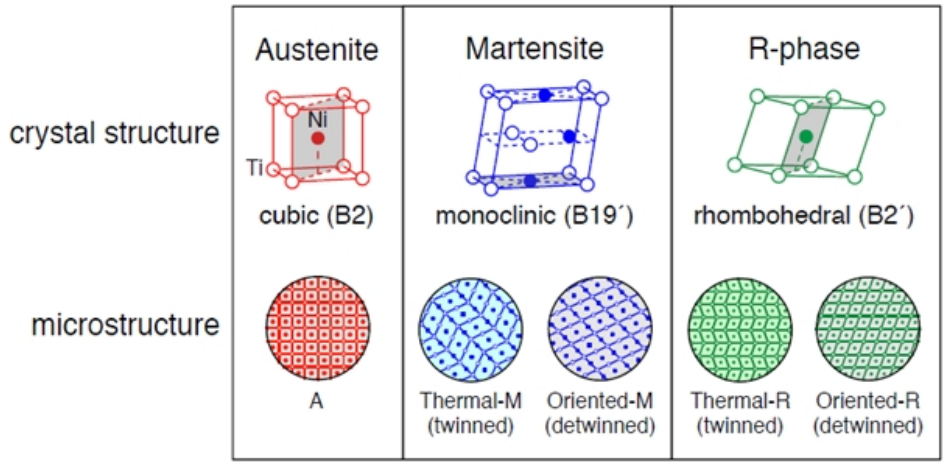

Figure 1-1 Schematics of three primary crystallographic structures and their microstructures. [Figure 2 from 3]

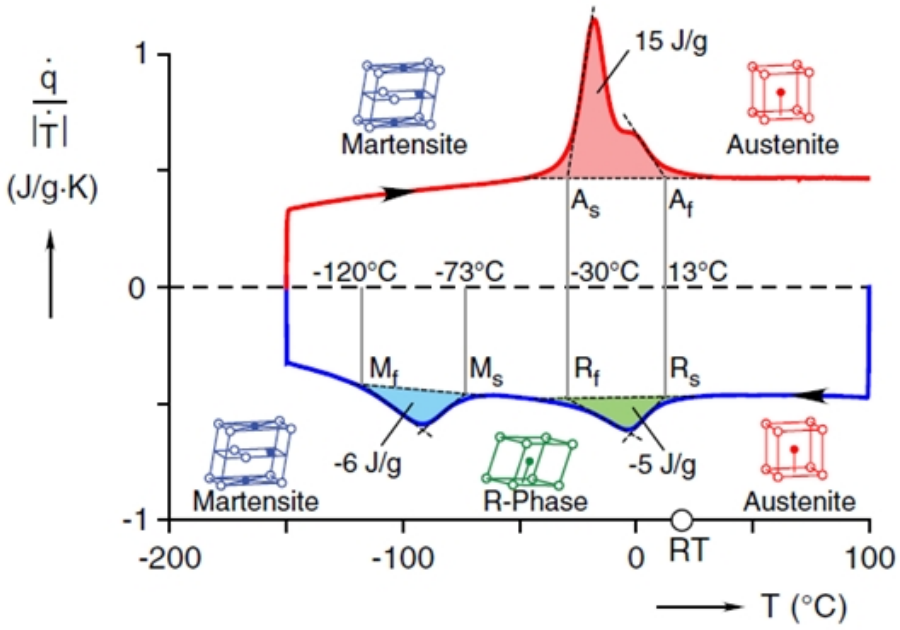

Figure 1-2 Differential scanning calorimetry thermograms of superelastic wire. [Figure 3b from 3]

Both the shape memory effect and superelasticity are caused by a solid-to-solid, diffusionless phase transformation between the austenite and martensite phases, but these effects proceed along different pathways. The three-dimensional graph in figure 1-3 shows the paths of the shape memory and superelastic effects. The path of the shape memory effect follows from point 0 to point 5 in figure 1-3. At point 0, the sample is initially twinned martensite. As the sample is loaded until point 1, the twinned martensite becomes detwinned martensite. When the sample is released, there is only elastic unloading and the sample exhibits more than 4% residual strain, which appears at this point to be plastic deformation. However, as the sample is heated above A_f, the detwinned martensite phase transforms to austenite between points 3 and 4, and there is a reversion of the material to its original shape. When the sample is cooled down to a temperature below M_f, the austenite phase transforms to twinned martensite with no apparent shape change.

Superelasticity occurs at a consistent temperature above A_f, i.e. on the plane from point 5 to point 10 in figure 1-3. The sample is initially in the austenite phase at point 5. As the sample is loaded, the austenite transforms to detwinned martensite between points 6 and 7, and during this transformation there is a constant stress plateau under increasing strain. The transformation proceeds by large bands of localized strain that consist largely of martensite. At the end of the stress plateau, the bands have propagated completely through the specimen and it is considered to be macroscopically martensite. However, although the specimen is considered macroscopically martensite at this point, it has been observed that the specimen is not fully martensite upon the completion of transformation and residual pockets of austenite remain [4, 5].

Upon unloading, the detwinned martensite reverts to the austenite phase with nearly zero strain because the detwinned (stress-induced) martensite is not stable at this temperature. During the load-unload cycle, there is a noticeable hysteresis that can be exploited for damping applications. The ability of the sample to recover large strains with relatively little plastic deformation incurred is referred to as superelasticity, or pseudoelasticity.

Superelastic behavior is sensitive to temperature as shown in the macroscopic stress-strain curves of as-received NiTi wires at various temperatures in isothermal experiments shown in figure 1-4 [6]. In figure 1-4, the green, blue, and red lines indicate the R-phase, martensite, and austenite phases, respectively. When the ambient temperature is below A_f (in this case A_f = 13 ± 2 °C), the curves do not show complete superelastic behavior and exhibit residual strain upon unloading. As the ambient temperature is increased, the stress plateau of phase

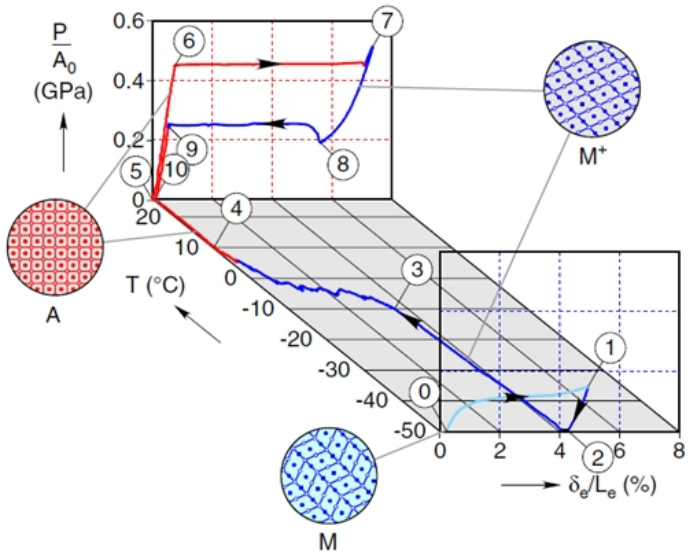

Figure 1-3 Three-dimensional stress-strain-temperature graphs describing the paths of the shape memory effect (0-5) and superelasticity (5-10). [Figure 7 from 3]

transformation shifts vertically upward. Once the temperature reaches A_f, the initial phase becomes macroscopically fully austenite and the curves show superelastic behavior, exhibiting a clear stress plateau and little residual strain. As the operating temperature continues to increase, the height of stress plateau also increases. Noticeable residual strain reappears at high operating temperatures due to plastic deformation with locked-in pockets of residual martensite. Ambient temperature is an important factor when considering the effect of globally applied strain rate on phase transformation during superelasticity because of the interaction between strain rate and latent heat distribution. The effect of strain rate will be discussed in section 1.4.

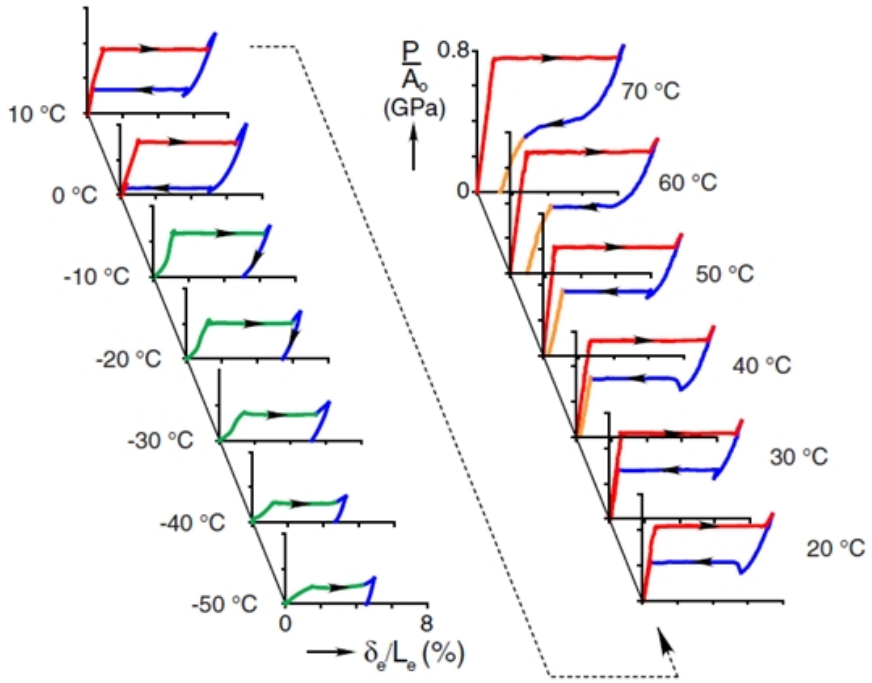

Figure 1-4 Macroscopic stress-strain curves of as-received superelastic wire under isothermal experiments at various temperatures. [Figure 8 from 6]

SMAs utilize either the shape memory effect or superelasticity in many applications in the automotive, robotics, aerospace and biomedical fields. One of the primary applications of SMAs is wire actuators due to their high work density, light weight, and compact size [7, 8]. SMA wire actuators essentially consist of a bias spring, an external spring and a SMA wire as shown in figure 1-5 [7]. The SMA wire is initially martensite phase and is stretched by δ_0 in equilibrium with the bias and external springs. When the wire is subjected to Joule heating, it transforms to the austenite phase contracting and providing work against the external spring by the amount of $\delta - \delta_0$. When the current is disconnected and the wire cools, the length of the wire reverts to the reference condition. In this way, the work against the external spring can be repeated and used to induce motion in applications such as micro circuit breakers and prosthetic limbs [9]. Other applications of the shape memory effect include commercial coupling methods,

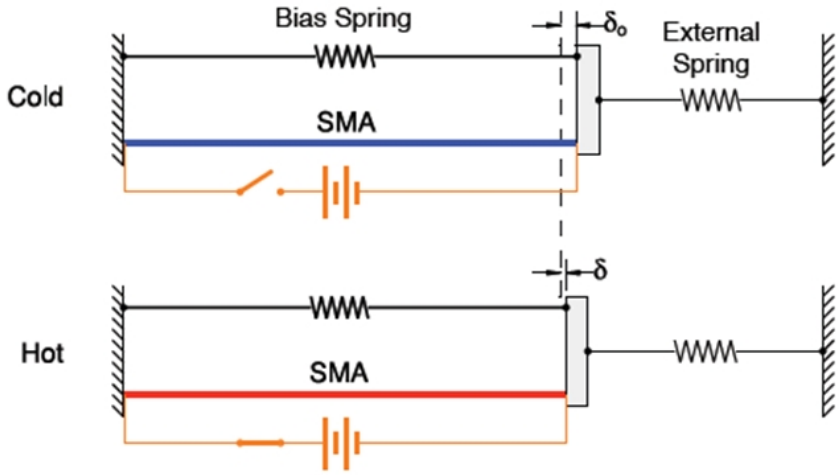

Figure 1-5 Prototype uniaxial SMA /bias spring actuator working against an external spring by joule heating [Figure 1 from 7].

such as CryoFit for aerospace tubing, where the shrinkage of NiTi pipe in warm temperature is used in metal-to-metal couplings for leak free performance [10, 11].

The superelastic effect is utilized in numerous devices, particularly in biomedical applications. In medical devices, superelastic self-expanding stents (see figure 1-6a) to support the arteries of vascular disease patients are made with SMA for its biocompatibility, its ability to maintain a constant load in a large strain range, and an evenly distributed stress field along the radial direction [10]. Additionally, the ability of SMA stents to self-expand inside the body minimizes invasive medical procedures [12]. Dental braces (see figure 1-6b) are also made of SMAs to obtain a narrow range of the correction force, which leads a reduction in length of orthodontic treatments and check-ups [10]. Other examples of the use of Nitinol in daily applications include superelastic eyeglasses frames (see figure 1-6c) and cell phone antennas (see figure 1-6d) [13]. In civil engineering, SMA wires are used for self-centering structures in seismic applications because of their superelasticity, large damping, energy storage capacity [14, 15].

Numerous shape memory alloys, such as AuCd, CuZnAl, CuAlNi, and NiTi, have been discovered since the mid-1900s. SMAs are roughly classified into Fe-based alloys, Cu-based alloys, and Ni-Ti alloys. Because Fe-based alloys do not have a significant two-way effect or superelasticity, Cu-based alloys (such as CuZnAl, CuAlNi, and CuAlBe) and NiTi alloys are largely used in commercial applications. Among them, nearly equiatomic NiTi -- known by its commercial name Nitinol and discovered in 1959 by William J. Buehler of the U.S. Naval Ordnance Laboratory [16]) -- is extensively used in practical applications and is under rigorous

investigation. Polycrystalline NiTi can exhibit approximately 8% shape recovery, 8% superelastic strain above transient temperature (A_f), and near 800 MPa of recovery stress. Additionally, NiTi shows higher work density, 2.5 x 10^7 J/m^3, than other smart materials, which is suitable for the compact designs shown in table 1-1, and has good biocompatibility as well as corrosion resistance [17].

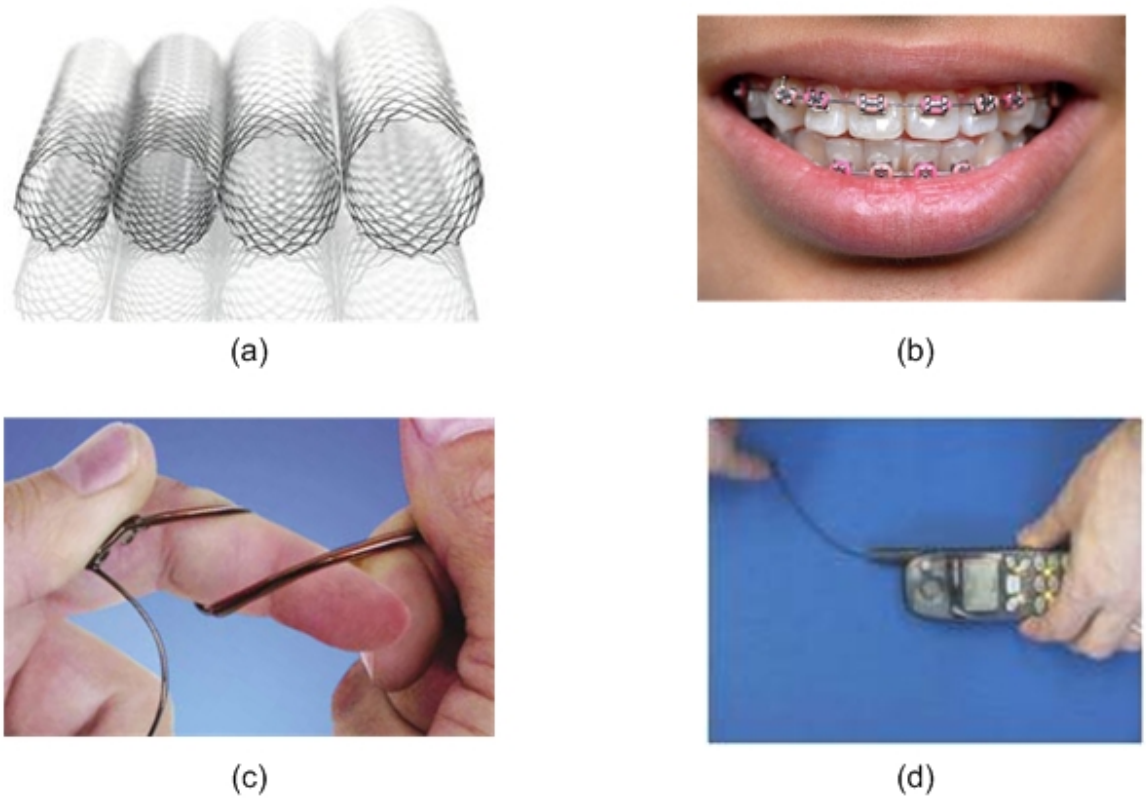

Figure 1-6 Applications of superelastic SMAs: (a) Stent [www.ev3.net], (b) Dental braces [www.business-opportunities.biz], (c) Superelastic eyeglasses frame [todaysmachiningworld.com], and (d) Cell phone antenna [education.mrsec.wisc.edu]

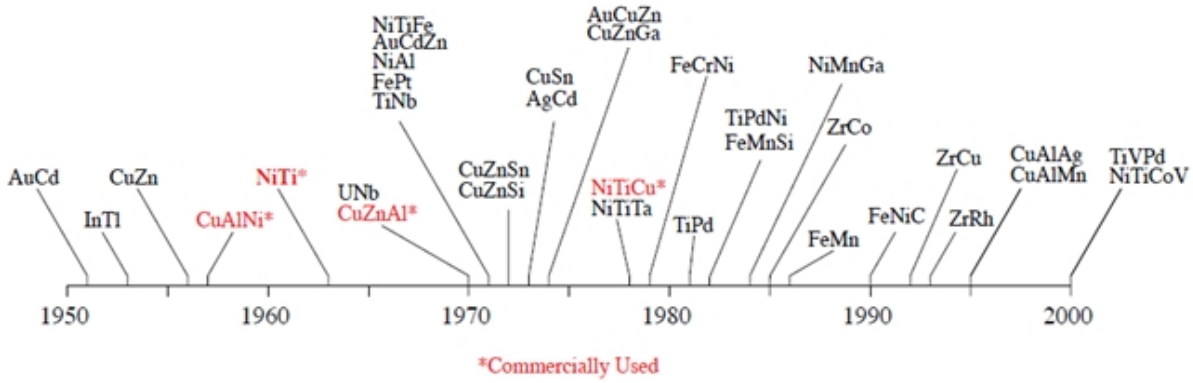

Figure 1-7 History of the discovery of important shape memory alloys. [18]

Table 1- 1 Work per unit volume for various microactuators. [Table 1 from 19]. NiTi SMA has a higher work density than other smart materials and is particularly well-suited for compact design.

Actuator Type	W/v (J/m^3)	Comments
Ni-Ti SMA	2.5×10^7	max, one-time output, 5% strain, 500 MPa
	6.0×10^6	thousands of cycles, 2% strain, 300 MPa
Solid-Liquified Phase Change	4.7×10^6	water (2.2 GPa bulk modulus) acetamide (8% volume change)
Thermo-pneumatic	1.2×10^6	measured values (20N, 50 μm displacement)
Thermal Expansion	4.6×10^5	ideal, nickel on silicon, $\Delta T = 200°C$
Electro-magnetic	4.0×10^5	ideal, variable reluctance
	2.8×10^4	measured, variable reluctance
	1.6×10^3	measured torque, external field
Electro-static	1.8×10^5	ideal, 100 V, 0.5 μm gap
	3.4×10^3	measured, comb drive
	7.0×10^2	measured, integrated force array
Piezoelectric	1.2×10^5	calculated, PZT
	1.8×10^2	calculated, ZnO
Muscle	1.8×10^4	measured, 350 kPa, 10% strain
Microbubble	3.4×10^2	measured, 71 μm diameter

Constitutive modeling has been used to predict SMA material behavior, both for use in finite element methods and to determine relationships between an input microstructure and the resulting macroscopic stress-strain relation. Roughly speaking, two approaches have been developed – internal state variable models and micro-mechanical models. The internal state variable approach has been developed using constitutive equations determined by thermodynamics considering internal state variables and for use in engineering analysis tools including finite element methods. Conversely, micro-mechanical approaches use numerical averaging methods in order to quantitatively examine the relationship between microstructural input variables and the stress-strain response spanning the micro to macro scale. The internal state variable approach is currently more developed for the modeling of cyclic loading, due to the lack of micro-mechanism fatigue theory in SMAs [20]. Recently, Tanaka's phenomenological one-dimensional model has been further developed by Liang and Rogers [21] and Brinson [22]. The model begins with the energy balance (first law of thermodynamics) and the Clausius-Duhem inequality (another expression of the second law of thermodynamics). Tanaka [23] assumes a set of state variables – Green strain, temperature, and the fraction of martensite as an internal state variable – to describe material behavior. Using Helmholtz free energy and the inequality equation, constitutive equations and the dissipated energy term are derived and expressed in rate form using five material constants. This model can show both superelasticity and the shape memory effect. Brinson [22] further developed Tanaka and Liang's models thorough a separation of the martensite fraction as a purely temperature-induced martensite and a stress-induced martensite.

In the micro-mechanical approach, the crystallographic theory of martensitic transformation has been widely studied [24-28]. It was found that the recoverable strain in a polycrystalline SMA depends on both the crystallographic texture of the polycrystal and the change of symmetry during transformation. Crystallographic symmetry is an important factor in determining the recoverable strain in polycrystalline shape memory alloys. It has been shown through the calculation of recoverable strain in various types of polycrystals that transformations with small changes in symmetry, such as cubic to tetragonal, do not show significant amounts of recoverable stain. This is because of the small number of accessible variants, which means that each grain can be rearranged to transform only in limited strain directions. A cubic to monoclinic transformation, such as that of NiTi, shows significant amount of recoverable strains due to high symmetry [24]. In addition, Shu and Bhattacharya [25] calculated recoverable strains using the inner bound (Taylor bound or Voigt's assumption), which is obtained by assuming the same average strain on each grain, and outer bound (Sachs bound or Reuss's assumption), which is obtained by ignoring compatibility between grains and allowing each grain to deform as it prefers. They found that the Taylor bound is conservative in its estimation of the recoverable strain of a cubic-monoclinic transformation by direct comparison with experimental results.

The effect of crystallographic texture on the shape memory effect on Ti-Ni and Cu-Zn-Al alloys has also been studied and it is found that the crystallographic texture which develops during rolling and drawing is favorable for the large recoverable strains in Ti-Ni. Inoue et al. [27] and Miyazaki et al. [28] theoretically calculated the recoverable strain in each grain with lattice parameters during martensitic transformation and found that the maximum recoverable strain

exists near [011] and [111] poles in a standard stereographic triangle but not at the [100] pole. The effect of crystallographic texture on mechanical properties on NiTi will be discussed in detail in section 1.5.

1.3 The Effect of Cycling

Mechanical cycling significantly affects superelastic characteristics of SMAs, such as the critical stress required for phase transformation, the accumulated residual strain, and the amount of hysteresis. Several factors can influence the behavior of nickel-titanium under cyclic loads, including Ni content, heat treatment of the sample prior to testing, temperature and applied strain rate at which the test is conducted, and initial microstructure, among others. An example of the effect of cycling on experimentally obtained macroscopic stress-strain curves of nickel-titanium wire (0.5 mm diameter) are shown in figure 1-8 [29]. The changes of the stress-strain response incurred by cyclic loading can be somewhat controlled by processing; for example, a decrease in the amount of accumulated residual strain can be achieved by suppressing slip during phase transformation through raising the critical stress for slip using an appropriate heat treatment. However, fatigue will eventually cause failure even with appropriate heat treatments that prolong life.

Previous research has intensively examined the effect of mechanical cycling on the characteristics of superelasticity and stability of these characteristics [4, 29-35]. The general effect of cycling is to increase residual strain, and decrease both the critical stress for phase transformation and amount of hysteresis. Miyazaki et al. [29] postulated that slip deformation,

responsible for the accumulation of residual strain, occurs during phase transformation and causes internal stresses that assist in the formation of stress-induced martensite. Thus, the stresses required for the nucleation and propagation of martensite during loading significantly decrease with cycling, but the stresses required for the nucleation and propagation of austenite during unloading remain nominally constant. They observed that the residual strain, stress required for phase transformation, and hysteresis stabilize with cycling, and explained this stabilization by work hardening due to introduction of dislocations. As part of this work, Miyazaki et al. also found that changes in the macroscopic responses incurred by cycling are not caused by elastic cycling of the austenite, but rather by cyclic transformation between the austenite and martensite. Nominally similar macroscopic stress-strain responses were observed for the 1st and 52nd transformation cycles with fifty interim elastic cycles. In addition, optical micrographs of the surface of the NiTi specimens were examined during loading and after unloading, and increases in the amount of residual martensite near the grain boundaries in the

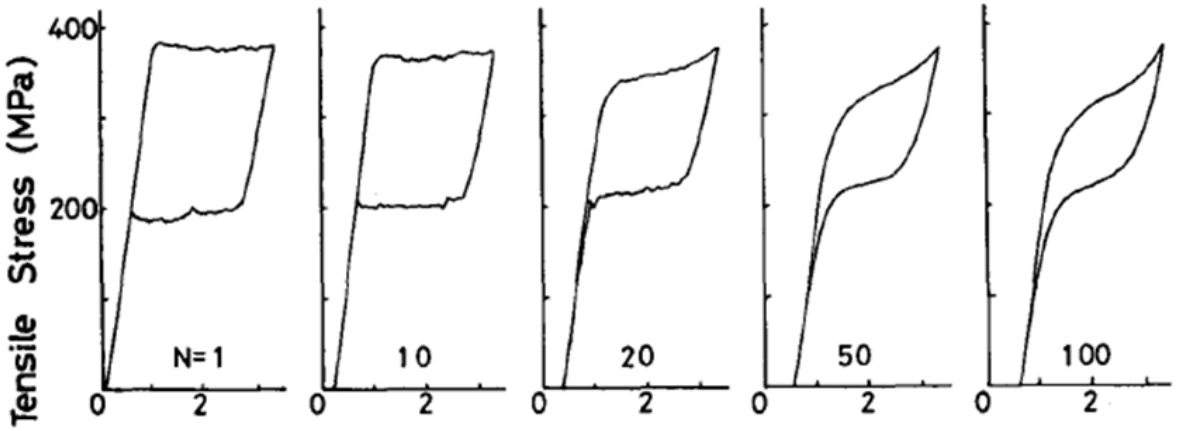

Figure 1-8 Effect of cycling on macroscopic stress-strain curves. [Figure 2b from 29]

unloaded samples after cycling were observed. They concluded that retained martensite plates, caused by slip deformation in the martensite, assist in the formation of the martensite in subsequent cycles and decrease the stress required for phase transformation with cycling [29]. In support of this finding, Brinson et al. [4] also observed residual martensite pockets upon unloading under optical microscopy and determined that these result in the accumulation of residual strain.

Strnadel et al. [31, 32] found that larger nickel content in Ti-Ni shape memory alloys increases the critical stress for slip, resulting in smaller accumulated residual strain. Displacement-controlled and load-controlled cycling tests were conducted for specimens varying in Ni content at temperatures where the specimens had a constant critical stress for phase transformation in the first cycle. Conducting cycling tests with the same transformation stress was performed to give objective results independent of nickel content, which affects critical phase transformation temperatures and thus changes the magnitude of the stress for phase transformation. In order to characterize the stability of the cycling, the residual strain, the critical stress for transformation, and the hysteresis were measured. Higher nickel content (through suitable heat treatment) caused an increase in the critical stress for slip due to increased dislocation activity [31]. If the critical stress for slip is high enough and the material easily undergoes cyclic strain hardening at a given test temperature, the residual strain rapidly reduces and the stress-strain curves stabilize with cycling. Strnadel et al. concluded that the critical stress for slip is the dominant factor in deformation at low cycles but the stress required for phase transformation becomes dominant at high cycles. This was investigated by observing a reversal

in the amount of accumulated residual strain of various nickel-content alloys at the eighth hard loading cycle.

In addition to nickel content, the ambient test temperature also affects the cyclic response of SMAs. In addition to observing the effects of cycling on residual strain and hysteresis corresponding with the findings described above, Nemat-Nasser et al. [30] also examined the effect of testing temperature on the cyclic compression tests of 4.5mm diameter nickel-titanium wire. Compression tests at different ambient temperatures were conducted and it was found that a higher (326K) testing temperature results in a more rapid stabilization than a lower (296K) testing temperature.

Stabilization of the macroscopic response of SMAs, known as shakedown, occurs with cycling [29-32, 34]. The degree of stability can be characterized by factors such as the amplitude of stress required for phase transformation, the amount of accumulated residual strain and the amount of hysteresis. One proposed mechanism for cyclic shakedown is the continuous accumulation of dislocations around defects, which increases internal stresses and assists with the austenite to martensite transformation [29, 31]. Crystallographic orientation and the existence and size of (Ti_3Ni_4) precipitates also affect dislocation activities and consequently the cyclic shakedown characteristics of NiTi [29, 31, 35, 36]. The dependence of macroscopic shakedown under compressive cyclic loading with regard to crystallographic orientation and Ti_3Ni_4 precipitates was examined on specimens of single crystal NiTi containing Ti_3Ni_4 precipitates of various sizes by Gall and Maier [35]. They observed that the crystallographic orientations approaching [100] pole of the stereographic triangle have the highest fatigue resistance, i.e.

limited change in the associated stress-strain curves with cycling. However, orientations approaching the [111] pole have the lowest resistance, i.e. significant changes in the stress-strain curves and large accumulation of residual strain with cycling. With respect to Ti_3Ni_4 precipitates, a smaller precipitate size (10nm) resulted in more fatigue resistance than 500 nm precipitates due to the absence of dislocation activity during cycling.

1.4 The Effect of Strain Rate on Phase Transformation

The first order phase transformation that underlies superelasticity in SMAs causes local self-heating (self-cooling) when the sample is loaded (unloaded). Local temperature directly affects the phase transformation and material behavior as discussed in section 1.2 (for more examples please see [37-42] and the references contained therein). Because the amount of accumulated latent heat varies with applied strain rate, the mechanical response of SMAs, including the stresses required for transformation and the amount of accumulated residual strain, is significantly affected. For example, faster applied strain rates cause an ineffective escape of latent heat, thus causing a corresponding increase in the global stresses required for phase transformation at local hot locations in the specimen. The general effect of strain rate on the macroscopic stress-strain curve is shown in figure 1-9 [40]. For example, the stress required for martensite nucleation, the amount of dissipated energy, and the residual strain increase at higher strain rates, but the stress for reverse phase transformation and the recoverable strain energy decreases. These changes are caused by the trapped latent heat at higher strain rates ($\dot{\varepsilon} \geq 1.667 \times 10^{-3}\ s^{-1}$). However, the material properties such as stress for phase transformation,

dissipated work, and recoverable strain energy are not dependent on strain rates of $\dot{\varepsilon} \leq 3.333 \times 10^{-4}\ s^{-1}$ [40].

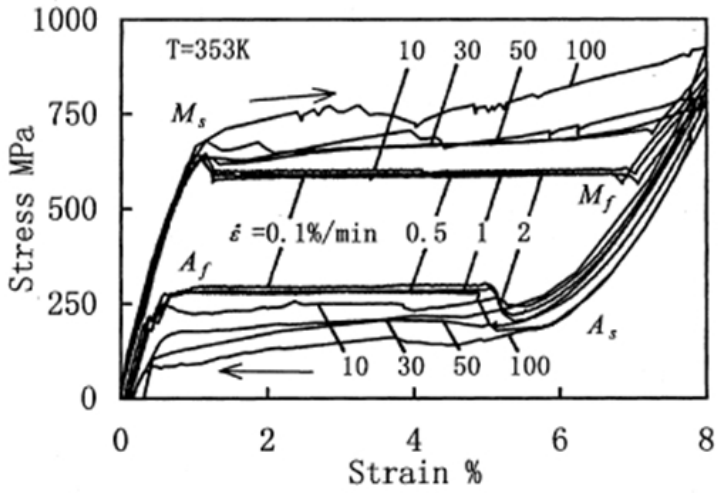

Figure 1-9 Effect of strain rate on the stress-strain curves at T = 353 K. [Figure 1b from 40]

The Clausius-Clapeyron relation is a well-known relation that uses the equivalence of Gibbs free energy in the quasi-static condition to define the relationship between phase transformation temperature and stress. Designating the austenite and martensite phases by α and β, respectively, the characteristic potential is defined as:

$$\phi = U - TS - fL \quad \text{(Eqn. 1)}$$

where U is internal energy [J], T is temperature [K], S is entropy [J/K], f is applied load [N] and L is the length of the gage section [m]. After applying the 1st and 2nd thermodynamic laws, the derivative form of the characteristic potential is expressed by:

$$d\phi = -SdT - Ldf \quad \text{(Eqn. 2)}$$

The Clausius-Clapeyron relation assumes that the free energies of the α and β phases are the same on the phase boundary in order to determine the slope of the phase boundary between the phases. The two-phase coexistence line is defined by:

$$\phi^{\alpha} = \phi^{\beta} \quad \text{(Eqn. 3)}$$

where ϕ^{α} and ϕ^{β} are the characteristic potentials of the α and β phases. Equivalently,

$$d\phi^{\alpha} = d\phi^{\beta} \text{ along } (f^{*}, T^{*}) \quad \text{(Eqn. 4)}$$

where f^* is the applied load and T^* is specimen temperature at the location of phase transformation. Combining equations (2) and (4) yields,

$$\frac{df^{*}}{dT^{*}} = -\frac{(S^{\beta} - S^{\alpha})}{(L^{\beta} - L^{\alpha})} > 0 \quad \text{(Eqn. 5)}$$

where $(S^{\beta} - S^{\alpha}) < 0$ and $(L^{\beta} - L^{\alpha}) > 0$. Because the entropy of the α phase is higher than β phase (austenite, the α phase, is stable at high temperature and martensite, the β phase, is stable at low temperature) and the martensite (monoclinic) is longer than the austenite phase (B2 cubic), the result of equation (5) is that the stress for phase transformation increases as the temperature of transformation increases. The Clausius-Clapeyron relation is only valid under quasi-static conditions and gives insight into the relation between phase transformation stress and

temperature. The stress required for phase transformation increases as temperature increases as seen in the Clausius-Clapeyron relation: $\frac{d\sigma^*}{dT^*} > 0$ [37, 38, 40, 43] at ~6.5 MPa/K [6, 38].

The stress required for nucleation of the martensite phase is affected by both strain rate and cycling. Under quasi-static loading, there is a distinct constant stress plateau during phase transformation. However, at faster strain rates, the amplitude of stress plateau is not constant but continuously increases during forward phase transformation because of trapped latent heat [37, 40]. Tobushi et al. [40] also found that there exist distinct transformation nucleation peaks at the onset of the stress plateau at slow strain rates, and hypothesized that the peaks is due to sufficient time by slow strain rates that allow a stress relaxation. However, the peaks diminish with cycling because the accumulation of martensite makes it easier to transform in cycling. Nemat-Nasser and Guo [30] found that, in experiments performed at extremely fast strain rates (4200 s^{-1}) with Split Hopkinson Bars, the stress plateau disappeared and the macroscopic curve appeared similar to ordinary austenite metal. They hypothesized that the phase transformation changes from a diffusionless and shear-like mechanism to a dislocation-based slip mechanism.

1.5 The Effect of Texture

General processes to produce SMA sheets and wires, including cold-rolling and cold drawing followed by heat treatment, induce preferred microstructural orientations. The crystallographic texture significantly affects superelastic properties, such as the stress required for phase transformation, and the amount of recoverable and residual strain. These are important

factors that need to be considered for the proper use of NiTi in many applications. In previous research, the transformation stress and strain were examined by experiments using SMA samples cut at different angle along to the rolling direction in flat sheet specimens. It was observed that samples cut along the rolling direction exhibited the largest transformation strains and those cut along the transverse direction exhibited the largest transformation stresses [1, 44, 45]. One example of the effect of crystallographic texture on the macroscopic stress-strain response is shown in figure 1-10 [46]. In these experiments by Gao et al. [46], an angular dependence to the rolling direction of the Young's modulus of austenite, transformation stress from austenite to martensite, and superelastic transformation strain was observed. Maximum values of austenite Young's modulus and the transformation stress were found at an angle of 70° to the rolling direction and the maximum transformation strain was measured at an angle of 30° to the rolling direction. Similarly, Zhao et al. [47] examined a TiNiCu alloy under constant load thermal cycling to see how the crystallographic texture plays a role in determining the amount of transformation strain. They observed that the transformation strain remains constant upon 60° to the rolling direction, then rapidly decreases with the orientation towards the transverse direction. Similarly, significant angular dependence of transformation strain in the shape memory alloys has been shown in other research [44, 45, 48].

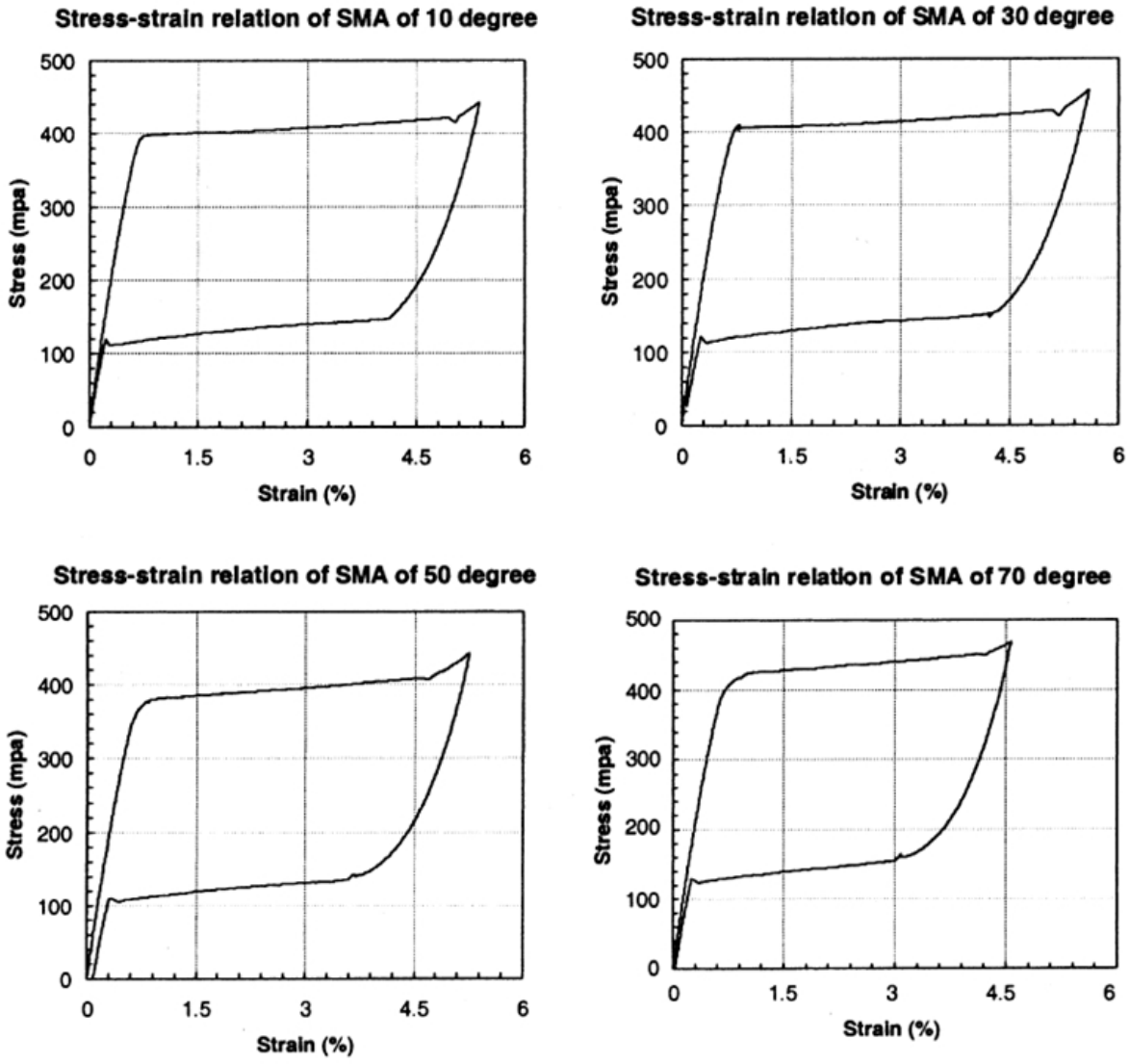

Figure 1-10 Effect of texture on the stress-strain curve. [Figure 1 from 46]

Bhattacharya et al. [24] theoretically explained that a greater change in crystallographic symmetry during transformation shows greater recoverable and residual strains in polycrystalline SMAs due to a greater number of rearranging martensite variants. Shu et al. [25] found that the texture that develops in NiTi during rolling, extrusion, and drawing is extremely favorable for

large recoverable strains, whereas NiTi thin films with an unfavorable {110} or random sputtering texture recover comparatively small strains. Mulder et al. [49] calculated the angular dependence of Schmid factor for slip on the $(001)[100]_M$ system for the four possible martensite phases, which can be caused by $\{110\}\langle 1\bar{1}0\rangle_P$ system of the austenite, and found that the Schmid factor for the transverse direction was close to zero indicating less slip and residual strain. Chang et al. [50] experimentally measured the angular dependence of residual strains and verified the postulate by Mulder et al. The crystallographic texture also results in an asymmetry of tension and compression response of SMAs and has been examined both experimentally and theoretically [51-53]. A model for polycrystalline SMAs applied an approach of constant stress average was developed and showed how the crystallographic orientation affects macroscopic behaviors, such as asymmetric response between tension and compression [51].

The crystallographic texture, which strongly impacts the mechanical properties of SMAs, is itself affected by heat treatments and cold rolling reduction as well as how the specimen is produced, such as by drawing into tubes or rolling into plates. The texture of as-drawn NiTi tubes and rolled plates under various heat treatment conditions were measured and it was found that the texture of both tube and plate specimens, followed by annealing, significantly changed [54]. For NiTi plate, the texture of as-rolled plate was $\{111\}\langle 112\rangle$ and changed to $\{435\}\langle 312\rangle$ after annealing because of grain growth and recrystallization. The effect of cold-rolling reduction and annealing temperature on crystallographic texture, and the angular dependence of transformation strain on NiTi rolled thin plates and sputter-deposited thin films were also examined by Miyazaki et al. [28]. They theoretically calculated the transformation strain in a

single grain using lattice parameters and the contour lines of the same transformation strain was expressed on a standard stereographic triangle of [001]-[011]-[$\bar{1}$11]. In the results on the standard stereographic triangle, the transformation tensile strains near [$\bar{1}$11] and [011] show high strains of 9.9% and 8.4%, respectively, but the transformation strain near [001] has smallest strain of 3.0%. The cold-rolling reduction also affects the degree of texture. Though the largest transformation strain commonly appears from 0° to 35° from the rolling direction for all cold-rolling reduction, the degree of anisotropy on the transformation strain decreases as the cold-rolling reduction increases from 0% to 70%. They explained both the dislocation generation and texture distribution cause the change of the transformation strain by loading direction [28]. The sputter-deposited thin films were examined and they did not show angular dependence on the transformation strain because the thin film has a strong {110} pole normal to the specimen surface. Inoue et al. [27] showed similar calculated results of the transformation strain using lattice constants and compared them with experimental results. The gap between theoretical and experimental results were explained by the increasing number of grain boundaries as the angle approaches 90° to the rolling direction. This was verified by observation of the number of grain boundaries per unit length under the optical microscope. It was hypothesized that the constraints becomes more pronounced as the number of grain boundaries increased and the constraints cause a deviation of the recoverable strain between the theoretical and experimental results.

1.6 Summary

In this chapter, the unique characteristics of SMAs, including their shape memory and superelastic effects, which are both based on a solid-to-solid phase transformation between austenite and martensite, were demonstrated with crucial applications. Next, a background discussion of the effects of cycling, applied strain rate, and crystallographic orientation on phase transformation, including thermo-mechanical effects such as the stress required for transformation and residual strain, was addressed in sections 1.3 to 1.5. In spite of this previous research, much is still unknown about the complex local-thermo mechanical interactions that underlie this transformation. Because the phase transformation causes large localized deformations that release/absorb latent heat, the measurement of simultaneous full-field strain and temperature maps by DIC and infrared thermography are utilized here to examine the spatial distribution of transformation. This experimental approach is described in chapter 2. Through application of this approach, transformation characteristics including cycle-to-cycle strain similarity, phase front velocity, martensite volume fraction and the relation between local strain and temperature are investigated. In chapter 3, the effect of cycling on local deformation fields, including strain similarity in a single cycle and cycle-to-cycle, will be discussed. In chapter 4, the effect of crystallographic orientation on phase transformation characteristics, such as stress for phase transformation, number of localized deformation bands, and cycle-to-cycle strain similarity, are examined. In chapter 5, the effect of applied strain rate on the phase transformation and its relationship to the accumulation of latent heat is also discussed. Finally, conclusions and possibilities for future work are described in chapter 6.

References

[1] S. Daly, G. Ravichandran, and K. Bhattacharya, "Stress-induced martensitic phase transformation in thin sheets of Nitinol," *Acta Materialia*, vol. 55, no. 10, pp. 3593–3600, Jun. 2007.

[2] K. Bhattacharya, "Microstructure of martensite: why it forms and how it gives rise to the shape-memory effect," *Oxford Series on Materials Modelling. Oxford University Press*, NY, first edition, 2003

[3] J. A. Shaw, C. B. Churchill, and M. A. Iadicola, "Tips and tricks for characterizing shape memory alloy wire: part 1 – differential scanning calorimetry and basic phenomena," *Experimental Techniques*, vol. 32, no. 5, pp. 55–62, 2008.

[4] L. C. Brinson, I. Schmidt, and R. Lammering, "Stress-induced transformation behavior of a polycrystalline NiTi shape memory alloy: micro and macromechanical investigations via in situ optical microscopy," *Journal of the Mechanics and Physics of Solids*, vol. 52, no. 7, pp. 1549-1571, Jul. 2004.

[5] M. Kimiecik, J. W. Jones, and S. Daly, "Quantitative studies of microstructural phase transformation in Nickel–Titanium," *Materials Letters*, vol. 95, pp. 25–29, Mar. 2013.

[6] C. B. Churchill, J. A. Shaw, and M. A. Iadicola, "Tips and tricks for characterizing shape memory alloy wire: part 2 – fundamental isothermal responses," *Experimental Techniques*, vol. 33, no. 1, pp. 51–62, 2009.

[7] J. A. Shaw and C. B. Churchill, "A reduced-order thermomechanical model and analytical solution for uniaxial shape memory alloy wire actuators," *Smart Materials and Structures*, vol. 18, no. 6, p. 065001, Jun. 2009.

[8] K. Ikuta, M. Tsukamoto, and S. Hirose, "Shape memory alloy servo actuator system with electric resistance feedback and application for active endoscope," Proceedings, *IEEE International Conference*, vol. 1, pp. 427 –430, 1988.

[9] Dynalloy, Inc. www.dynalloy.com

[10] D. Mantovani, "Shape memory alloys: properties and biomedical applications," *JOM*, vol. 52, no. 10, pp. 36–44, Oct. 2000.

[11] Aerofit, Inc. www.aerofit.com

[12] T. Duerig, A. Pelton, and D. Stöckel, "An overview of nitinol medical applications," *Materials Science and Engineering: A*, vol. 273–275, no. 0, pp. 149–160, Dec. 1999.

[13] J. Van Humbeeck, "Non-medical applications of shape memory alloys," *Materials Science and Engineering: A*, vol. 273–275, no. 0, pp. 134–148, Dec. 1999.

[14] M. Dolce and D. Cardone, "Mechanical behaviour of shape memory alloys for seismic applications 2. Austenite NiTi wires subjected to tension," *International Journal of Mechanical Sciences*, vol. 43, no. 11, pp. 2657–2677, Nov. 2001.

[15] J. McCormick and R. DesRoches, "Characterization and optimization of shape memory alloy behavior for seismic vibration control applications in buildings", *The 14th world conference on earthquake engineering*, Oct. 2008.

[16] G. B. Kauffman and I. Mayo, "The story of Nitinol: the serendipitous discovery of the memory metal and its applications," *The Chemical Educator*, vol. 2, no. 2, pp. 1–21, 1997.

[17] J. Ryhänen, E. Niemi, W. Serlo, E. Niemelä, P. Sandvik, H. Pernu, and T. Salo, "Biocompatibility of nickel-titanium shape memory metal and its corrosion behavior in human cell cultures," *Journal of Biomedical Materials Research*, vol. 35, no. 4, pp. 451–457, 1997.

[18] M. Schwartz. "Encyclopedia of Smart Materials," vol. 1, *John Wiley and Sons*, New York, NY, 2002.

[19] P. Krulevitch, A. P. Lee, P. B. Ramsey, J. C. Trevino, J. Hamilton, and M. A. Northrup, "Thin film shape memory alloy microactuators," *Journal of Microelectromechanical Systems*, vol. 5, no. 4, pp. 270 –282, Dec. 1996.

[20] K. A. Gall, "NiTi experiments versus modeling: where do we stand?," *Proceedings of SPIE*, vol. 3992, pp. 536-547, 2000.

[21] C. Liang and C. A. Rogers, "One-Dimensional Thermomechanical Constitutive Relations for Shape Memory Materials," Journal of Intelligent Material Systems and Structures, vol. 1, no. 2, pp. 207 –234, Apr. 1990.

[22] L. C. Brinson, "One-dimensional constitutive behavior of shape memory alloys: thermomechanical derivation with non-constant material functions and redefined martensite internal variable," *Journal of Intelligent Material Systems and Structures*, vol. 4, no. 2, pp. 229 –242, Apr. 1993.

[23] K. Tanaka, "A thermomechanical sketch of shape memory effect: one-dimensional tensile behavior", *Res Mechanica*, vol. 18, no. 3, pp. 251-263, 1986.

[24] K. Bhattacharya and R. V. Kohn, "Symmetry, texture and the recoverable strain of shape-memory polycrystals," *Acta Materialia*, vol. 44, no. 2, pp. 529–542, Feb. 1996.

[25] Y. C. Shu and K. Bhattacharya, "The influence of texture on the shape-memory effect in polycrystals," *Acta materialia*, vol. 46, no. 15, pp. 5457–5473, 1998.

[26] K. Gall, H. Sehitoglu, Y. I. Chumlyakov, and I. V. Kireeva, "Tension–compression asymmetry of the stress–strain response in aged single crystal and polycrystalline NiTi," *Acta Materialia*, vol. 47, no. 4, pp. 1203–1217, Mar. 1999.

[27] H. Inoue, N. Miwa, and N. Inakazu, "Texture and shape memory strain in TiNi alloy sheets," *Acta Materialia*, vol. 44, no. 12, pp. 4825-4834, Dec. 1996.

[28] S. Miyazaki, V. H. No, K. Kitamura, A. Khantachawana, and H. Hosoda, "Texture of Ti-Ni rolled thin plates and sputter-deposited thin films," *International Journal of Plasticity*, vol. 16, pp. 1135-1154, 2000.

[29] S. Miyazaki, T. Imai, Y. Igo, and K. Otsuka, "Effect of cyclic deformation on the pseudoelasticity characteristics of Ti-Ni alloys," *Metallurgical Transactions A*, vol. 17, no. 1, pp. 115-120, 1986.

[30] S. Nemat-Nasser and W. G. Guo, "Superelastic and cyclic response of NiTi SMA at various strain rates and temperatures," *Mechanics of Materials*, vol. 38, no. 5-6, pp. 463-474.

[31] B. Strnadel, S. Ohashi, H. Ohtsuka, T. Ishihara, and S. Miyazaki, "Cyclic stress-strain characteristics of Ti-Ni and Ti-Ni-Cu shape memory alloys," *Materials Science and Engineering A*, vol. 202, no. 1-2, pp. 148-156, Nov. 1995.

[32] B. Strnadel, S. Ohashi, H. Ohtsuka, S. Miyazaki, and T. Ishihara, "Effect of mechanical cycling on the pseudoelasticity characteristics of Ti-Ni and Ti-Ni-Cu alloys," *Materials Science and Engineering A*, vol. 203, no. 1-2, pp. 187-196, Nov. 1995.

[33] H. Sehitoglu, R. Anderson, I. Karaman, K. Gall, and Y. Chumlyakov, "Cyclic deformation behavior of single crystal NiTi," *Materials Science and Engineering A*, vol. 314, no. 1-2, pp. 67-74, Sep. 2001.

[34] M. A. Iadicola and J. A. Shaw, "The effect of uniaxial cyclic deformation on the evolution of phase transformation fronts in pseudoelastic NiTi wire," *Journal of Intelligent Material Systems and Structures*, vol. 13, no. 2-3, pp. 143 -155, Feb. 2002.

[35] K. Gall and H. J. Maier, "Cyclic deformation mechanisms in precipitated NiTi shape memory alloys," *Acta Materialia*, vol. 50, no. 18, pp. 4643-4657, Oct. 2002.

[36] K. Melton and O. Mercier, "Fatigue of NiTi thermoelastic martensites," *Acta Metallurgica*, vol. 27, no. 1, pp. 137–144, Jan. 1979.

[37] J. A. Shaw and S. Kyriakides, "Thermomechanical aspects of NiTi," *Journal of the Mechanics and Physics of Solids*, vol. 43, no. 8, pp. 1243-1281, Aug. 1995.

[38] P. G. McCormick and Y. Liu, “Thermodynamic analysis of the martensitic transformation in NiTi-II. Effect of transformation cycling,” *Acta Metall. Mater.*, vol. 42, no. 7, pp. 2407-2413, Jul. 1994.

[39] J. A. Shaw, “Simulations of localized thermo-mechanical behavior in a NiTi shape memory alloy,” *International Journal of Plasticity*, vol. 16, no. 5, pp. 541-562, Apr. 2000.

[40] H. Tobushi, Y. Shimeno, T. Hachisuka, and K. Tanaka, “Influence of strain rate on superelastic properties of TiNi shape memory alloy,” *Mechanics of Materials*, vol. 30, no. 2, pp. 141-150, Oct. 1998.

[41] S. Miyazaki, K. Otsuka, and Y. Suzuki, “Transformation pseudoelasticity and deformation behavior in a Ti-50.6at%Ni alloy,” *Scripta Metallurgica*, vol. 15, no. 3, pp. 287-292, Mar. 1981.

[42] I. Schmidt, “A phenomenological model for superelastic NiTi wires based on plasticity with focus on strain-rate dependency caused by temperature,” *Journal of Engineering Materials and Technology*, vol. 128, no. 3, pp. 279-284, Jul. 2006.

[43] J. A. Shaw and S. Kyriakides, “On the nucleation and propagation of phase transformation fronts in a NiTi alloy,” *Acta Materialia*, vol. 45, no. 2, pp. 683-700, Feb. 1997.

[44] Y. Fukui, T. Inamura, H. Hosoda, K. Wakashima, and S. Miyazaki, “Mechanical properties of a Ti-Nb-Al shape memory alloy,” *Materials Transactions*, vol. 45, pp. 1077–1082, 2004.

[45] H. Y. Kim, T. Sasaki, K. Okutsu, J. I. Kim, T. Inamura, H. Hosoda, and S. Miyazaki, “Texture and shape memory behavior of Ti–22Nb–6Ta alloy,” *Acta Materialia*, vol. 54, no. 2, pp. 423–433, Jan. 2006.

[46] S. Gao and S. Yi, “Experimental study on the anisotropic behavior of textured NiTi pseudoelastic shape memory alloys,” *Materials Science and Engineering: A*, vol. 362, pp. 107–111, Dec. 2003.

[47] L. Zhao, P. F. Willemse, J. H. Mulder, J. Beyer, and W. Wei, “Texture development and transformation strain of a cold-rolled Ti50-Ni45-Cu5 alloy,” *Scripta Materialia*, vol. 39, no. 9, pp. 1317–1323, Oct. 1998.

[48] T. Inamura, Y. Fukui, H. Hosoda, K. Wakashima, and S. Miyazaki, “Relationship between texture and macroscopic transformation strain in severely cold-rolled Ti-Nb-Al superelastic alloy,” *Materials transactions - JIM*, vol. 45, no. 4, pp. 1083-1089.

[49] J. H. Mulder, P. E. Thoma, and J. Beyer, “Anisotropy of the shape memory effect in tension of cold-rolled 50.8 Ti 49.2 Ni (at.%) sheet,” *Z Metallkd*, vol. 84, no. 7, pp. 501-508, 1993.

[50] S. H. Chang and S. K. Wu, “Textures in cold-rolled and annealed Ti50Ni50 shape memory alloy,” *Scripta Materialia*, vol. 50, no. 7, pp. 937–941, Apr. 2004.

[51] P. Šittner and V. Novák, “Anisotropy of martensitic transformations in modeling of shape memory alloy polycrystals,” *International Journal of Plasticity*, vol. 16, no. 10–11, pp. 1243–1268, 2000.

[52] S. C. Mao, J. F. Luo, Z. Zhang, M. H. Wu, Y. Liu, and X. D. Han, “EBSD studies of the stress-induced B2-B19’ martensitic transformation in NiTi tubes under uniaxial tension and compression,” *Acta Materialia*, vol. 58, no. 9, pp. 3357–3366, May 2010.

[53] P. Thamburaja and L. Anand, “Polycrystalline shape-memory materials: effect of crystallographic texture,” *Journal of the Mechanics and Physics of Solids*, vol. 49, no. 4, pp. 709–737, Apr. 2001.

[54] S. W. Robertson, V. Imbeni, H. R. Wenk, and R. O. Ritchie, “Crystallographic texture for tube and plate of the superelastic/shape-memory alloy Nitinol used for endovascular stents,” *Journal of Biomedical Materials Research Part A*, vol. 72A, no. 2, pp. 190–199, 2005.

Chapter 2

Experimental Setup

This chapter describes the determination of transition temperatures in the SMA Nickel-Titanium by differential scanning calorimetry (DSC), the introduction of digital image correlation (DIC) and infrared thermography in the study of phase transformation, and the preparation of test specimens. Technical tips including sensitive calibration of 3D-DIC, proper setup procedure for optical equipment, and sample preparation with speckle patterning are explained in detail. Finally, an overview of the experimental setup is described.

2.1 Differential Scanning Calorimetry

Measuring critical transformation temperatures is an important step in the characterization of SMAs. The material exhibits hysteretic response in stress-free exothermic and endothermic process with several critical transformation temperatures including the austenite start temperature (A_s) and the austenite finish temperature (A_f) during heating, and the martensite start temperature (M_s) and the martensite finish temperature (M_f) during cooling. In the experiments presented here, the austenite finish temperature (A_f) was below room temperature, thus ensuring the specimen was austenite at room temperature and exhibited superelasticity. Differential scanning calorimetry (DSC) is an effective method for obtaining the transformation

temperatures and the latent heats required for transformation. A model TA-Q200 calorimeter was used to obtain the austenite start and finish temperatures, A_s and A_f. Tests using approximately 15 to 35mg of NiTi in one pan and an empty sample pan were both placed into the DSC to scan the heat flow of the specimen pan compared to the empty pan under a constant temperature rate. An intermediate temperature rate of 10°C/min was selected because higher rates can have thermal lag but small rates can show indistinct enthalphy peaks [1]. Consistent results were obtained with the exception of indistinct enthalphy peaks observed at a very low temperature range, around -70°C to -80°C, due to limitations with the DSC. This technical limitation of the DSC resulted in inaccurate martensite start (M_s) and finish (M_f) temperatures. Thus, for an accurate reading of these temperatures, the same DSC procedure was followed by TA Instruments and the result is shown in figure 2-1.

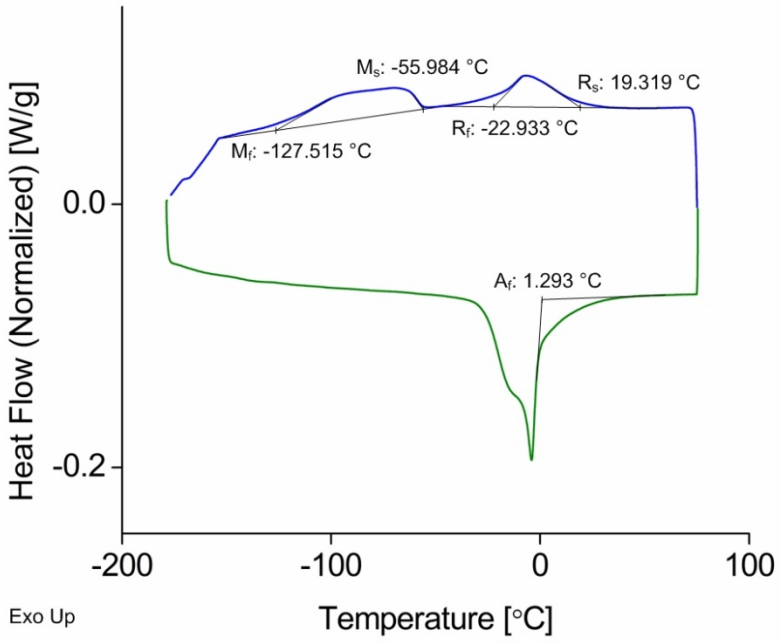

Figure 2-1 The critical transition temperatures by differential scanning calorimetry (DSC).

2.2 Digital Image Correlation

Digital image correlation (DIC) is an in-situ, non-contact optical method used to measure the full-field displacements on the surface of a specimen by tracking a non-uniform, random, isotropic, high contrast pattern on the sample surface. Because the DIC technique is robust, scalable, and accurate, it has emerged as a leading technique for quantifying heterogeneous strain fields on the surface of solid structures. One can choose between two-dimensional DIC, which uses one camera and maps deformations of flat materials deformed in-plane, and three-dimensional DIC which uses two cameras and can map out of plane displacements. For a detailed description of the fundamental concepts, computational algorithms, technical skills and useful applications of DIC, please refer to references [2-5]. In these experiments, commercial software (Vic-Snap from Correlated Solutions) was used to synchronize the two charge-coupled devices (CCDs) and take images, and commercial DIC software (Vic-3D from Correlated Solutions) was used to analyze the deformed images. Note that other software can be used in place of Vic-Snap for image capture, but the image format should be uncompressed, such as bitmap or tiff.

3D-DIC is an ideal method for measuring full-field, quantitative maps of surface strains incurred by stress-induced martensite phase transformation because of the large difference in local strains between the B2 cubic austenite phase and the monoclinic martensite phase. Two five-megapixel gray scale CCD (model Point Grey GRAS-50S5C) cameras were used to capture images of the specimens during testing. The setup of the CCDs with respect to the specimen and a pre-test calibration are important in order to obtain high quality results in a 3D-DIC analysis. Several factors affect the quality of the specimen images and the resulting strain analysis,

including the stereo angle between the two CCDs, specimen illumination, CCD depth-of-field (DOF), and CCD field-of-view (FOV). These factors should be carefully considered during test setup. The experimental setup procedure used here is described below, where general photography techniques were used.

1. Two CCD cameras were positioned on an optical table in front of an Instron (model 5585) load frame. The optical table prevents vibration that would cause rigid body motion in the images and increase correlation errors. Thus, using the optical table is recommended in the DIC experiments rather than placing the cameras directly on a floor-mounted tripod.
2. The position of the CCDs was determined by the CCD field-of-view (FOV) and lens choice. The CCD field of view was chosen in accordance with general DIC rules wherein it is recommended that each speckle should occupy nominally 3 x 3 image pixels and a subset should contain at least 3 x 3 speckles [2]. The maximum displacement of the specimen during testing should be considered while setting the field of view. During testing, the bottom grip of the load frame was fixed and the upper grip moved vertically upward; thus, the bottom of the specimen was aligned at the bottom of the image and the top of the image had nominally 5mm of empty space to capture the whole specimen at the maximum elongation. Additionally, since grip slippage can be an issue for small or thin specimens and can be detected by the sequence of images, it is helpful to set the FOV to contain both the top and bottom grips, if the resolution of the FOV is sufficient. Lenses and the distance between the cameras and the specimen were chosen after choosing both the resolution and the FOV. The stereo angle between two cameras, which affects the result of the calibration between the two cameras, was set to approximately 30°.

3. Obtaining a clear focus is the next step to obtain high quality images for 3D-DIC, and this is closely related to a depth-of-field (DOF), aperture, exposure time, and illumination. Because the procedures for obtaining a clear focus follow standard photography techniques, the specifics are not discussed here. However, the basic procedure is to fully open the aperture for centering the DOF, to find a clear focus, and to close back down the aperture before enlarging to the test DOF. The DOF increases as the aperture closes. However, an overly closed aperture (in these tests, nominally below f/8) produces blurred images and poor correlations. Image blurriness can be exacerbated by small CCD pixel size, particularly when the Airy disc (caused by light diffraction through the aperture) is larger than a pixel. Closing the aperture also requires a larger amount of light, but high intensity light can increase the specimen temperature and cause changes in mechanical behavior. This is particularly true in the case of NiTi, where increased temperatures can cause changes in factors such as the critical stress for phase transformation and the amount of recoverable strain. In addition, the exposure time changes the required amount of light. Since the fastest globally applied strain rate in our experiments was 10^{-2} s^{-1}, a shorter exposure time was needed to avoid image blur and thus more light was required. The lighting source should be carefully chosen considering the specimen temperature and required illumination under the fixed aperture and exposure time. In these experiments, two fluorescent light diffuser boxes wrapped with translucent plastic were placed behind the cameras to produce a diffuse and flat light, and flexible fiber optic lights with adjustable light intensity were positioned above the CCDs with their light positioned directly onto to the specimen. Care should be taken so that the cameras are not disturbed and all equipment around the cameras should be controlled. Cables should be securely

tied down. If the cameras are bumped or otherwise moved, they need to be reset following the procedure outlined above and considering all conditions including the FOV, the DOF, illumination, aperture, the exposure time and the focus.

4. A calibration procedure is necessary to precisely obtain the relative orientation of two cameras prior to testing and post-test image correlation. Generally, the calibration procedure is performed by taking images of a known calibration grid (located in the position of the test specimen) in different positions and orientations. The calibration grid size should be carefully selected and it is recommended that all dots in the grid are visible in the FOV. However, using too small of a grid may lead to a failed calibration. The calibration grid and adequate size of the grid are shown in figure 2-2. At least four calibration images are required, but a greater number will reduce measurement uncertainty and better quantify the effect of lens distortions. More details regarding the calibration procedure are explained in commercial testing guides [6]. In these experiments, the specimen was removed from the grips and the calibration grid (model P/N AIG 045466 or P/N AIG 052985, designed to be backlit by cold light illumination) was attached to the top grip. A white flat sheet was placed behind the grid and the fiber optic light was used to make an even backlight for the calibration grid. Nominally 35 - 40 different pairs of calibration images were taken with six degrees of freedom using a three axis gimble, two micrometer stages and movement of the top grip. Since the calibration result is sensitive to certain conditions, including the stereo angle between the cameras, the degree of even backlight, and the tilting angle of the calibration grid, obtaining a good calibration result can be labor-intensive. However, the calibration of the cameras is a critically important step in obtaining accurate strain fields, and it is strongly

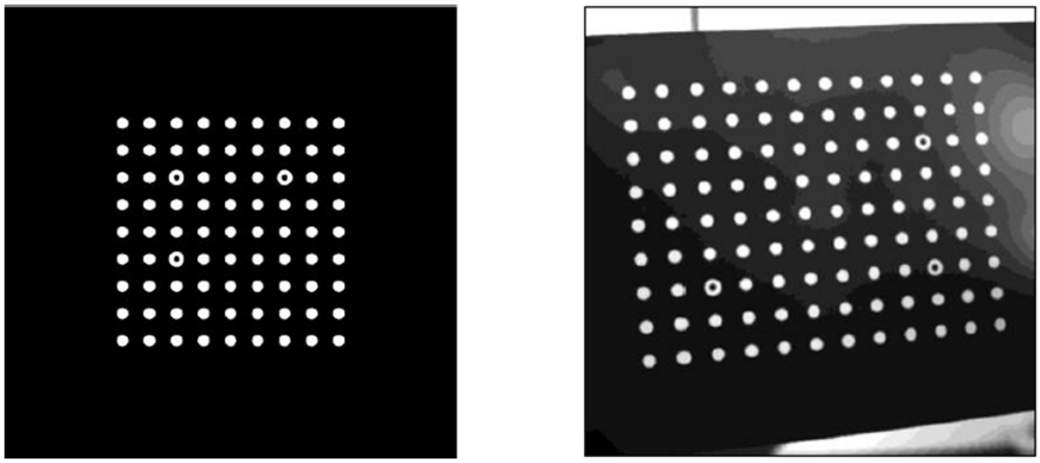

(a) (b)

Figure 2-2 (a) Vic-3D Calibration Grid, (b) correct selection of the calibration grid in the field-of-view [6].

recommended to spend significant effort in obtaining a high quality calibration. If at this point the CCDs are moved or bumped, even slightly, the whole calibration procedure needs to be re-performed prior to testing.

5. Performing a trial test with the specimen is strongly recommended before the start of testing. The trial test includes checking parameters of the DIC setup like exposure time, frame rate, and the amount of light, and also includes checking factors that impact image quality, such as the FOV, image focus, and DIC tracking pattern speckle size and distribution. Analyzing a select number of trial images of a rigid body test or a static test can provide the quality of images and the amount of error. Since a significant source of error can be due to poor calibration of the cameras, the calibration procedure should be performed again until the error value becomes satisfactorily low.

2. 3 Infrared Imaging

Nitinol is inherently sensitive to temperature. The stress-induced phase transformation between austenite and martensite is a first order transformation that releases (absorbs) latent heat upon loading (unloading). It is well known that the accumulation of this latent heat can significantly impact the mechanical properties of Nitinol. In order to quantify the accumulated latent heat in the specimen during stress-induced phase transformation, infrared imaging was utilized. An emissivity of 0.91 as calibrated by a K-type thermocouple was recorded. An infrared camera (model Inframetrics ThemaCam SC 1000) was placed between the two CCDs used for DIC, and a bottle containing ice water was placed behind the specimen in the FOV of the infrared image to increase contrast. While the IR camera was positioned, special care was necessary not to disturb the calibrated DIC setup and for the IR camera not to touch any CCDs because of the tendency of the IR camera to vibrate during testing. It was difficult to measure high-resolution images from the CCDs and IR camera simultaneously because the position of the IR camera with the best FOV would interfere with the position of the CCDs that results in the best FOV. The decision was made to place the CCDs in the optimal position, and then place the IR camera in the best possible position that remained open.

2.4 Specimen Preparation

A flat polycrystalline sheet of Nitinol with an alloy composition of 55 wt% nickel and 45 wt% titanium was obtained from Nitinol Devices and Components (NDC), Johnson and Johnson. The material was cold-rolled by the supplier into a continuous flat strip nominally 63.5 x 3048 mm long and 254 μm thick. The transition temperature (A_f = 1.293 °C) was determined as shown

in section 2.1 and the specimen exhibited superelasticity at room temperature. Dog-bone shaped tensile specimens were fabricated using electric discharge machining (EDM) at three different directions to the rolling direction of the flat sheet: 0º (RD), 45º, and 90º (TD). Specimen dimensions followed ASTM standard E8 with a thickness of 0.254 mm, width of 3.125 mm and gage length of 12.5 mm as shown in figure 2-3. Optical microscopy was conducted on an Olympus SC30 stereo-microscope with an MPlanFL N 20x lens in order to examine the surface of the as-received textured samples as shown in figure 2-4.

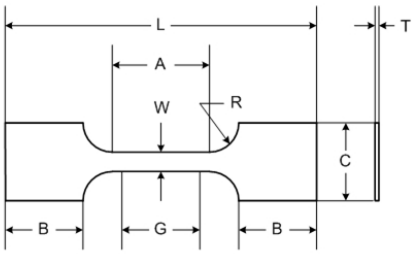

Dimension	mm
G — Gage length	12.5 ± 0.025
W — Width	3.125 ± 0.0625
T — Thickness	0.254
R — Radius of fillet	5
L — Over-all length	50
A — Length of reduced section	15
B — Length of grip section	12.5
C — Width of grip section	12.5

Figure 2-4 Specimen geometry followed ASTM standard E8

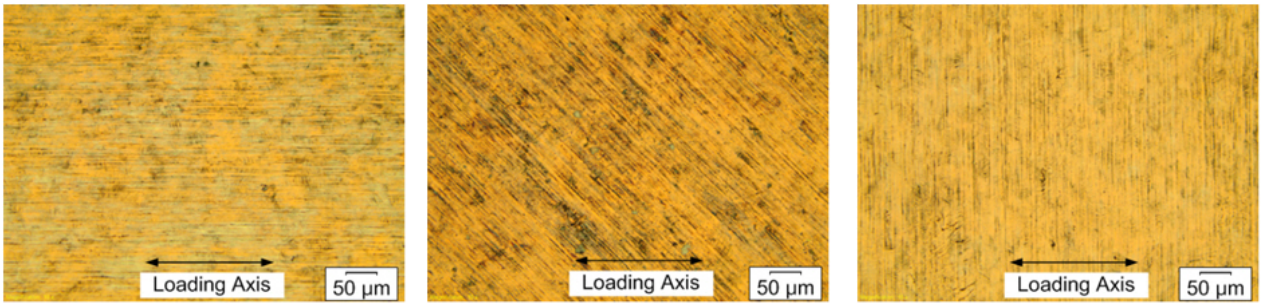

(a) (b) (c)

Figure 2-3 Optical micrographs of the textured surfaces at (a) RD, (b) 45°, and (c) TD to the rolling direction of the as-received sheet.

The specimen was speckled with white and black paints using a spray airbrush (model Iwata Custom Micron B) in order to satisfy the patterning condition for DIC, which is randomly oriented, uniformly dispersed, and high contrast. First, the specimen was painted with a background coat of Golden Airbrush Titanium White (model #8380). A thin, uniform white background is recommended for high contrast, but it is recommended to spray as thin a uniform background as possible in order to avoid cracking in the background coat during cyclic loading. The white-coated specimen was then painted with Golden Airbrush Carbon Black (model #8040) to produce a DIC pattern on the surface of the specimen. Useful tips for producing a quality airbrushed DIC pattern are as follows:

1. The spray airbrush was held approximately 50 – 100 mm away from the specimen and the paint flow was held continuous during a scan across the specimen without stopping in order to make uniformly dispersed pattern.
2. It was found that the smallest speckle size was produced by pulling the airbrush needle back as little as possible to allow paint to flow at a smaller rate for a longer period of time.
3. The air pressure setting affects the speckle size and the rate and continuity of paint flow. High air pressure is recommended for the smallest speckle size and uniformly dispersed pattern.
4. The recommended size of speckles for DIC is approximately 3 x 3 camera pixels as discussed in section 2.2 and Sutton et al. [2]. However, controlling the size of speckles is difficult. Thus, producing speckles with sizes ‘in the ballpark’ and then setting the FOV of the DIC cameras to follow the 3 x 3 rules is recommended.

After completing specimen preparation and CCD setup, the quality of image should be confirmed by analyzing trial experiments, including static and rigid body tests. One method to measure pattern quality is grey scale intensity histograms, where a good pattern should be nominally Gaussian in nature. An example of a patterned specimen, a histogram of grey scale intensity in the gage section, and a Gaussian fit are shown in figure 2-5. The spatial resolution in this case was 9 μm/pixel.

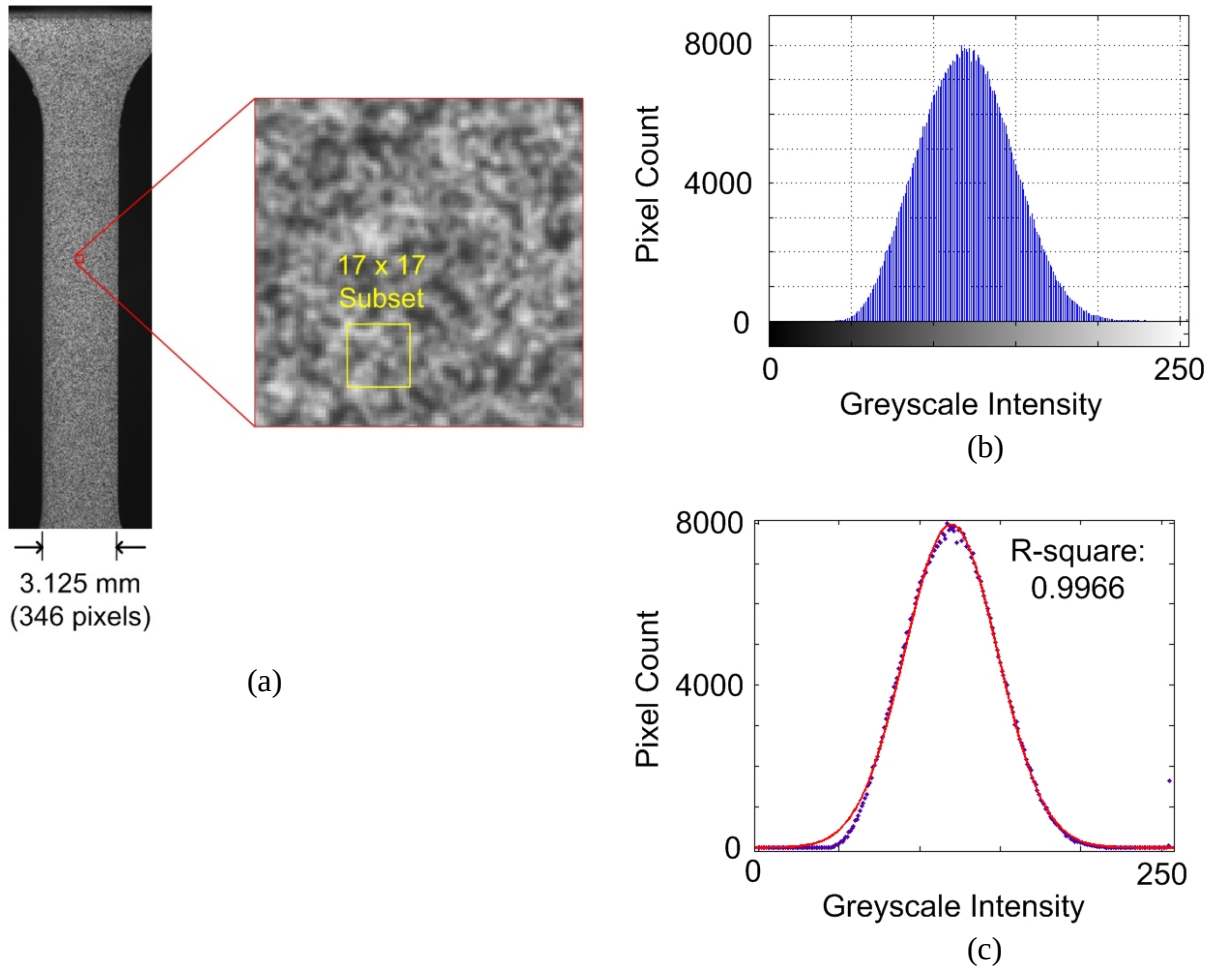

Figure 2-5 (a) Dog-bone shaped Nitinol thin sheet specimen and speckle pattern, (b) a histogram of grayscale intensity, and (c) a curve fitting of the grayscale with Gaussian distribution.

2.5 Overview of Experimental Setup

The experimental setup is discussed below. Note that the setup as described in this section is general and equivalent setups were used in the tests on thin sheet Nitinol specimens described in chapters 3-5.

A LabVIEW data acquisition (DAQ) system was used to collect all data, including elapsed time, load, grip displacement, CCD image capture time, and IR image capture time. Because it is important to synchronize all data from various equipment at one time domain, trigger signals from CCDs and IR camera were also recorded in the LabVIEW data acquisition system. A schematic of all equipment and connection between them is shown in figure 2-6 and the actual experimental setup is shown in figure 2-7. A 200.17-kN Instron (model Instron 5585) uniaxial load frame with mechanical wedge grips (model 2736-004, 100kN capacity) was used to perform displacement-controlled cycling tests up to $N = 50$. Tests were performed under a ramp profile at three globally prescribed (based on the total free length between the grips) strain rates ($\dot{\varepsilon}_g = 10^{-4}$,10^{-3}, and 10^{-2} s^{-1}) for each of the RD, 45º, and TD textures. Because these tests were performed under displacement control (hard cycling), the specimen did undergo a small amount of compression at the end of each cycle as residual strain accumulated. The 1st, 2nd, 5th, 10th, 25th, and 50th cycles were simultaneously recorded by the two CCDs and the IR camera to measure the full-field maps of local strains and temperature. The LabVIEW data acquisition system was used to collect the load (measured by a 453.6 kg load cell), grip displacement and time data for cycles $N = 1, 2, 5, 10, 25$, and 50. The CCDs (model Point Grey GRAS-50S5C) each had a 2048 x 2448 pixel field of view and pixel size (on the sensor) of 3.45μm. Camera positioning resulted in a stereo angle between the cameras of approximately 32° and a spatial

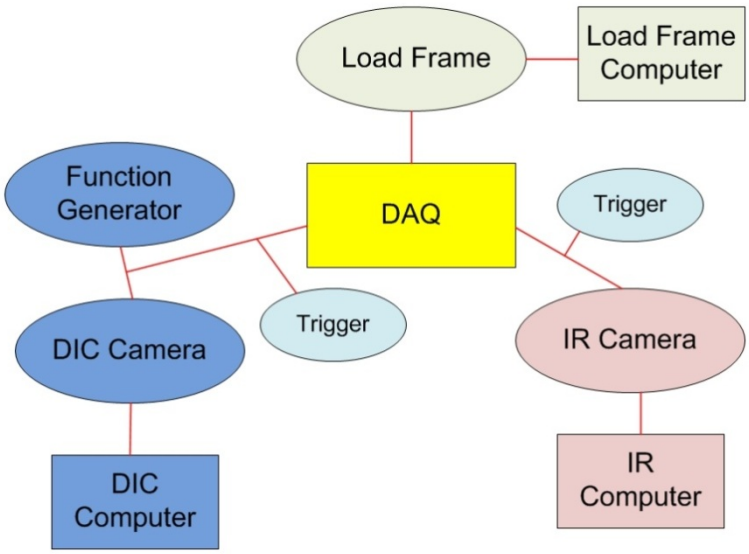

Figure 2-6 Schematic of equipment and connections.

resolution of 9 μm/pixel. The CCDs capture approximately 300 images per cycle and were operated by a function generator with adequate set of frequency depends on the strain rates. Note that approximately 110 images per cycle were captured on the fast strain rate, $\dot{\varepsilon}_g = 10^{-2}\ s^{-1}$, because of the limit of transferring frame rate on Vic-Snap software. The range of exposure time was 23.2 – 50 ms and the aperture size (f-stop) was f/8. The full-field strain maps were generated using commercial DIC software [2, 4, 5] with a subset size of 17 and a step size of 1 using the default cross correlation function in the software. For strain calculations, a Gaussian filter with a size of 15 was used. In these experiments, the Biot strain was calculated in order to have work conjugate measure. Biot strain is defined by $E^B = U - I$, where U is the right stretch tensor from the polar decomposition of the deformation gradient $F = R \cdot U$, with rigid rotation R and identity tensor I. The infrared camera (model Inframetrics ThermaCam SC 1000) was placed between the CCDs to obtain full-field temperature maps, which were generated with commercial Dynamite IR software (Themoteknix Systems Ltd.). In chapter 5, additional testing was conducted at a

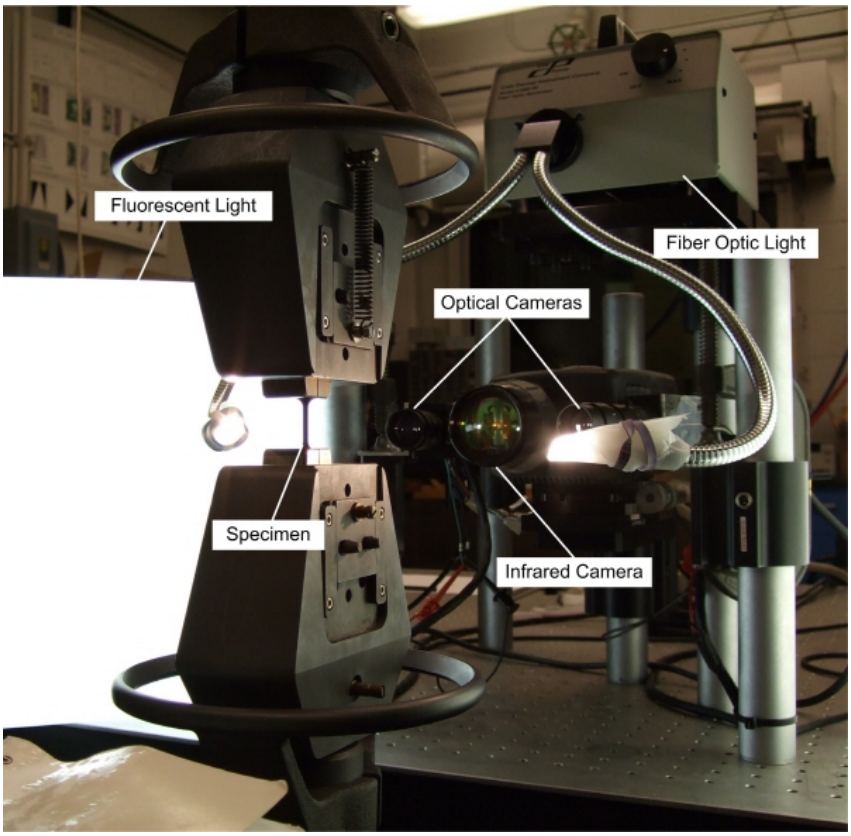

Figure 2-7 Experimental setup. The infrared camera is placed between two optical CCDs. The fiber optic light and the fluorescent light diffuser boxes provide uniform and diffuse light that enables a fast CCD frame rate and minimal blurring.

strain rate of $\dot{\varepsilon}_g = 10^{-2}\ s^{-1}$ using a hold time of 1800 seconds between each cycle. For these "with-hold" tests, which were conducted on specimens with all three crystallographic textures described above, used an equivalent experimental setup excepting the use of a different uniaxial load frame (MTS model 359) and IR camera (FLIR model SC5000).

The static and rigid body motion tests were performed to measure a static and translation error in 3D-DIC measurements after completing setup. The translation error in DIC

measurements fell within the error in the load frame applied translation (< 0.02 mm) for a range of 0 – 2 mm, and static error was approximately 0.025% as shown in figure 2-8.

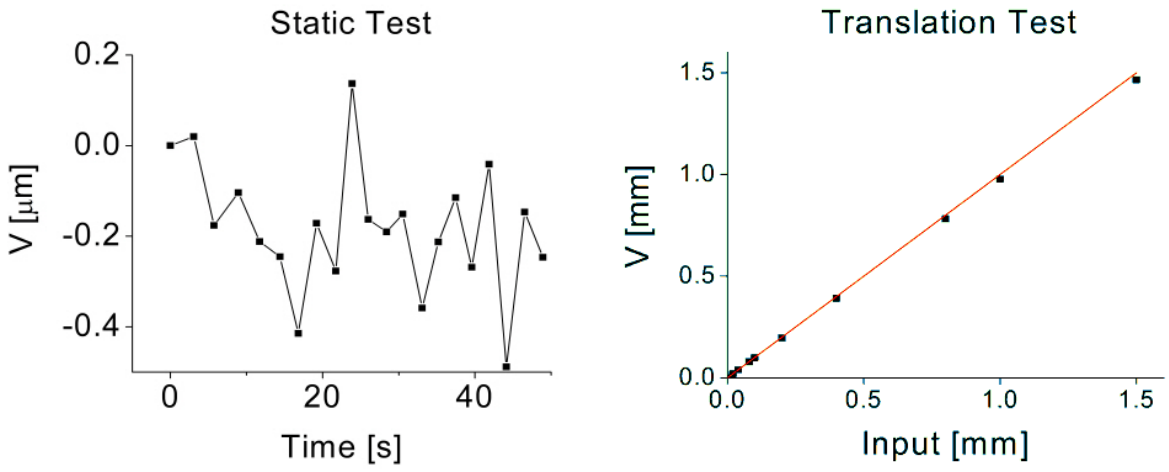

(a) (b)

Figure 2-8 (a) Static and (b) rigid body motion tests in order to measure a static and translation error in 3D-DIC measurements, respectively. V is the displacement of the y-axis.

References

[1] J. A. Shaw, C. B. Churchill, and M. A. Iadicola, “Tips and tricks for characterizing shape memory alloy wire: part 1 – differential scanning calorimetry and basic phenomena,” Experimental Techniques, vol. 32, no. 5, pp. 55–62, 2008.

[2] M. A. Sutton, J.-J. Orteu, and H. Schreier, Image Correlation for Shape, Motion and Deformation Measurements: Basic Concepts,Theory and Applications. Springer, 2009.

[3] S. H. Daly, “Digital Image Correlation in Experimental Mechanics for Aerospace Materials and Structures,” in Encyclopedia of Aerospace Engineering, John Wiley & Sons, Ltd, 2010.

[4] M. A. Sutton, J. H. Yan, V. Tiwari, H. W. Schreier, and J. J. Orteu, “The effect of out-of-plane motion on 2D and 3D digital image correlation measurements,” Optics and Lasers in Engineering, vol. 46, no. 10, pp. 746–757, Oct. 2008.

[5] M. A. Sutton, J. D. Helm, and M. L. Boone, “Experimental study of crack growth in thin sheet 2024-T3 aluminum under tension-torsion loading,” International Journal of Fracture, vol. 109, no. 3, pp. 285–301, 2001.

[6] Vic-3D 2010 Testing Guide, www.correlatedsolutions.com

Chapter 3

Martensite Strain Similarity in Nickel-Titanium Under Mechanical Cycling

This chapter describes an experimental study of stress-induced martensitic phase transformation in the SMA nickel-titanium. The rich local thermo-mechanical interactions that underlie transformation are examined using three-dimensional Digital Image Correlation (strain fields) and infrared imaging (thermal fields). We quantify the complex local interactions between released/absorbed latent heat and the extent of transformation, and explore the characteristics of the phase fronts and the evolution of martensitic volume fraction. We also quantify a strong strain similarity in the martensite that forms in the wake of the phase transformation front and persists from cycle to cycle. The accommodated strain in the martensite will remain nearly constant during loading as the existing phase front propagates. There also exists a remarkable amount of strain similarity in the martensite that persists from cycle to cycle, indicating that the local elastic stress fields in the martensite are driven by a dislocation structure and martensitic nuclei that largely stabilize during the first loading cycle.

3.1. Characteristics of Phase Fronts

The macroscopic stress-strain curve for the first cycle of an as-received specimen under a displacement-controlled strain rate of $\dot{\varepsilon}_g = 10^{-4}\ s^{-1}$, along with corresponding strain and thermal images at select points, is shown in figure 3-1. In this chapter, full-field maps of surface strain and temperature are shown on the length of a reduced section (15 mm) that is centered on and slightly larger than the gage section (12.5 mm). For reference, specimen geometry is shown in figure 2-3. Mapping across the length of reduced section shows, in addition to the response in the gage section, the completion of transformation near fillet regions that is reflected in the macroscopic response. The length of reduced section was mapped in order to have a larger visible strain region and track the completion of transformation. Each data point on the stress-strain curve in figure 3-1 represents an average of approximately 600,000 points on the full-field Lagrangian strain map across the gage section of the specimen at a point in time (ε_{YY}^{AVG}), plotted against the global engineering stress applied to the specimen as measured by the load cell at the same moment in time. Images of the specimen were taken after each displacement increment, and the strains in the gage section along the axis of applied load (ε_{yy}) were computed by digital image correlation. DIC images were triggered and captured directly into LabVIEW with the corresponding load data.

The specimen is macroscopically austenitic at the beginning of the test, behaving in a linear elastic manner with an approximate modulus of 62.3 GPa. The behavior begins to deviate from linearity at $\varepsilon_{YY}^{AVG} \approx 0.007$ for cycle 1. As loading continues, the macroscopic transformation from austenite to stress-induced martensite begins and the curve levels out into a

stress plateau. During this transition regime, a localized band of high strain indicating martensitic transformation forms at the top of the specimen and propagates through the gage section. The nucleation and propagation of the martensitic band can be seen in figure 3-1. The band gradually propagates through the entire gage length of the test sample, and the stress begins to increase around a macroscopic strain of $\varepsilon_{YY}^{AVG} \approx 0.063$. Following this, the behavior once again becomes linear with a modulus of approximately 20.5 GPa as the martensite is loaded. This value agrees with prior experimental and numerical investigations into the elastic modulus of stress-induced martensite, which found a range of 14-36 GPa depending on a variety of factors including applied strain rate and temperature [1-4]. The unloading follows a similar pattern, with an almost linear unloading with a modulus of nominally 35.8 GPa, followed by a departure from linearity at a strain of nominally $\varepsilon_{YY}^{AVG} \approx 0.062$. The stress plateau on unloading is indicative of the reverse transformation from martensite back to austenite, and the localized band accompanying this transformation can be seen through DIC and IR imaging in figure 3-1.

The experimental data in figure 3-1 shows the local self-heating that occurs with the nucleation of the martensitic band, and the relatively quick diffusion of this heat as the band propagates. The initial band nucleation causes a local heat rise of approximately 1.6°C compared with the average temperature in the specimen. Similarly, the final coalescence of the phase front upon unloading causes an approximate 1°C drop in temperature compared with the average temperature in the specimen. In figure 3-2, the local self-heating is examined by considering the simultaneous strain and thermal data down the centerline of the sample. Because there is inherent error in temporally matching the DIC data with the IR data, two IR profiles are shown that are both within this error range. In figure 3-2a, the strain and thermal data down the centerline of the

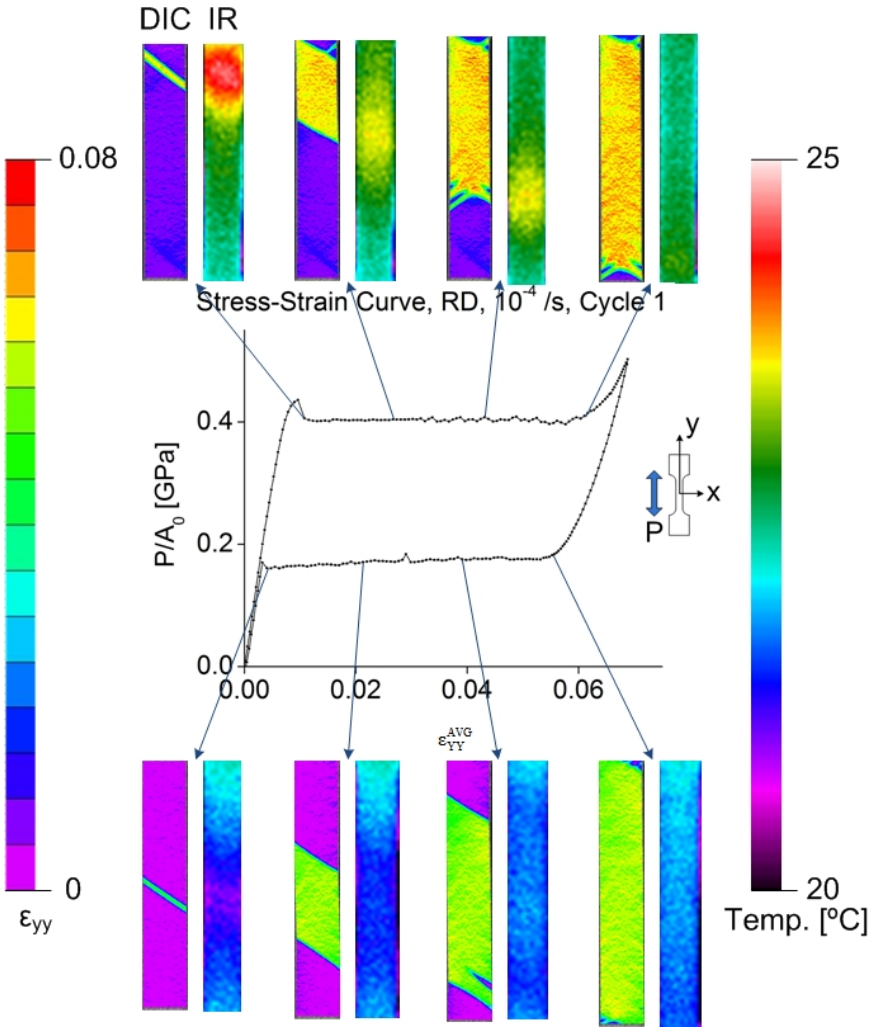

Figure 3-1 Stress-strain curve in the gage section of an as-received nickel-titanium specimen loaded at $\dot{\varepsilon}_g = 10^{-4}\ s^{-1}$ under displacement control in a ramp profile. The applied stress is obtained from the load cell and the strain along the axis of the specimen, ε_{YY}^{AVG}, is obtained by averaging approximately 600,000 strain values in each DIC image.

sample are shown just prior to the formation of a localized martensitic band. There is a small amount of local heating on the side of the specimen where the front will form, but overall the heat is fairly uniform. In figure 3-2b, the load on the specimen has increased, and the martensitic front has nucleated and propagated through approximately a third of the gage section. In figure

3-2c, the load on the specimen has further increased and the martensitic phase front has propagated through approximately two-thirds of the gage section. In figure 3-2d, the specimen has just become fully martensite. In these measurements, one can see that the local temperature maximum slightly leads the martensitic phase front, whose position is clearly visible through the DIC measurements. The pixel resolution of the strain measurements is approximately 9 μm, and each pixel contains hundreds of grains. The IR camera has a sensitivity of <0.07°C and an accuracy of 1.2°C. Note that the accuracy of the IR camera, 1.2 °C, refers to the difference in the recorded IR temperature as compared with the calibration thermo-couple, whereas the camera sensitivity (0.07 °C) refers to the resolution in the temperature field as measured by the IR camera. IR images were generated using the Dynamite IR program and analyzed with Matlab.

In figure 3-2e, the temperature at a fixed point in the center of the gage section of the specimen is monitored as the stress-induced martensitic phase front passes through that location. The discretization of the IR measurements in figure 3-2e is 0.3°C, due to interpolation in the dynamite IR program and the value of 60°C set for the temperature span range of the camera. After the phase front has passed through the center point, the temperature at this point slowly decreases as shown in figure 3-2e. The plateaus in the decreasing temperature may be due to the presence of a small martensitic off-shoot branch from the primary phase front, which gradually coalesces; this branch can be seen in the DIC images in figure 3-2e.

Let us take a closer look at the propagation of the stress-induced martensitic phase front in the as-received specimen. As shown in figure 3-3, there exist small branches that nucleate off of the larger martensitic band as the phase front propagates. The nucleation/coalescence of each branch corresponds directly to a small drop/rise in the macroscopic stress-strain curve. For

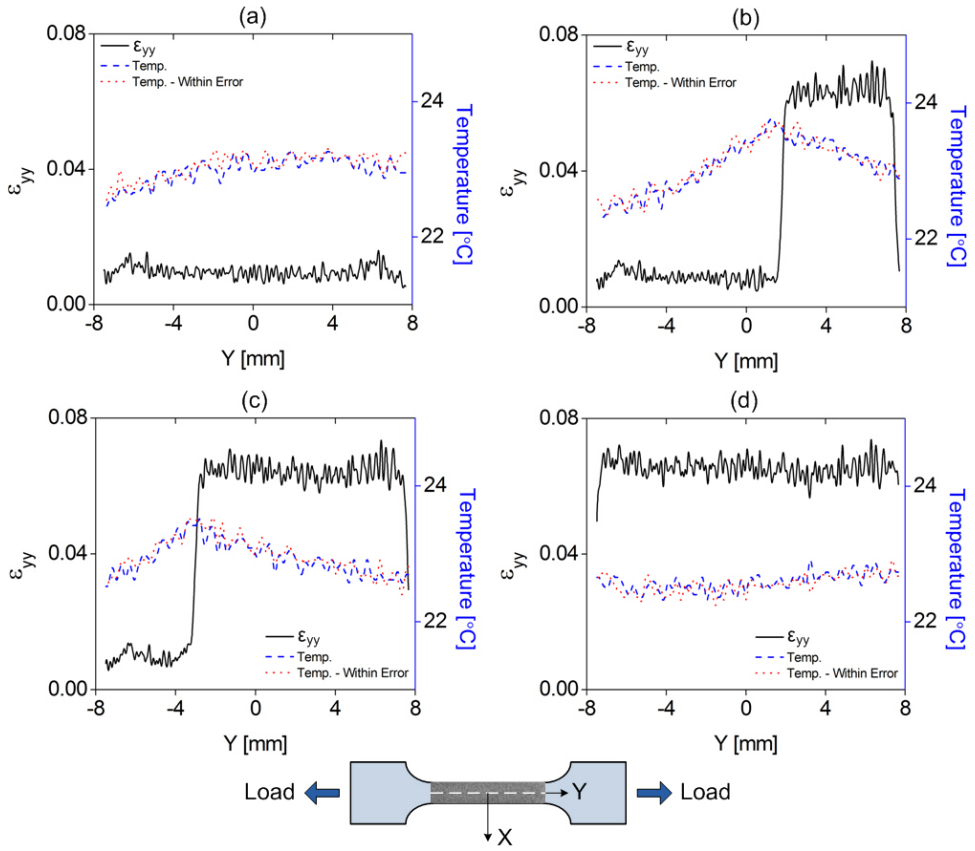

(e)

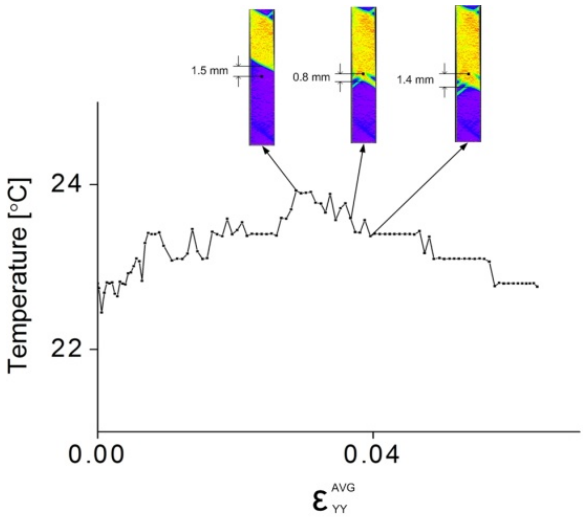

Figure 3-2 (a-d) show the nucleation and propagation of a stress-induced martensitic phase in the gage section of the sample, and corresponding IR data. Data in (a)-(d) is plotted on a line down the center of the specimen. (e) shows thermal data at a fixed point in the center of the specimen as the stress-induced martensitic phase front passes through that location. The lengths (in mm) that are indicated in the middle region of figure 3-2(e) are the distances from the fixed point to the phase interface. Both data sets are from the experimental test described in figure 3-1.

example, point 1 in figure 3-3 corresponds to the nucleation of the primary martensitic band; this drop in stress at nucleation has been widely observed. The primary martensitic band propagates as a single front until point 2, where a small branch occurs on the top right of the front. At point 3 in figure 3-3, the phase front begins to branch out and continues to branch out throughout the remainder of the macroscopic martensitic transformation; this is evident as 'bumpiness' in the macroscopic stress plateau. Branches nucleate at points 3-17 in figure 3-3, and each small branch from the primary transformation front has a corresponding stress drop in the macroscopic stress-strain curve. Similarly, upon unloading, rises in stress correspond to a coalescence of two smaller branches (as shown in figure 3-3, images 20 to 21). It is evident that the single large martensitic phase front propagates through the gage section by the formation of small branches off of the primary martensitic phase front, and that the nucleation and coalescence of these small branches directly affect the macroscopic stress-strain behavior.

The velocity of the phase transformation during loading is shown in figure 3-4a. Because the transformation front branches while it is propagating, it is not appropriate in this case to track the velocity perpendicular to the angled front, because there is no clearly delineated line that remains stable throughout the entire transformation. Instead, the velocity is calculated by tracking the position of the phase front on a line down the center of the gage section of the sample, as shown in the schematic in figure 3-4a. Thus, the peaks in the velocity data correspond to the nucleation of small branches off of the primary phase front. The front initially propagates as a single line angled approximately 53 degrees to the longitudinal axis of the sample. Small branches then nucleate off of the primary front, changing the phase front from an angled straight line into an inverted "v" shape, as shown in the DIC-calculated images of full-field strain in figure 3-4a. When a small branch nucleates off the primary front, it can shift the symmetry of

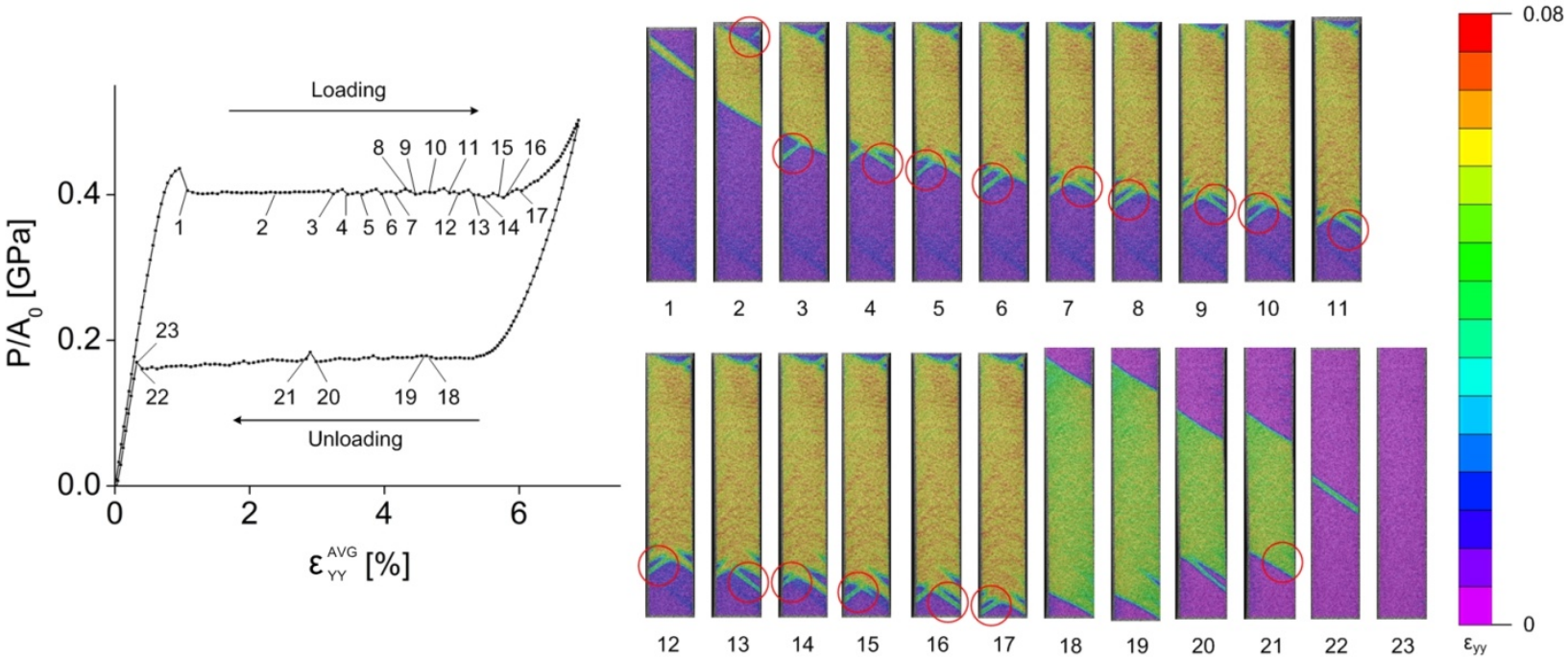

Figure 3-3 Detailed images of stress-induced martensitic transformation during the uniaxial tension test described in figures 3-1 and 3-2. Small branches of martensite appear off of the primary phase front; the nucleation/coalescence of these branches correlates directly with a small rise/drop in the stress. The nucleation of many of these branches in the second half of the plateau cause the latter half of the stress plateau to appear bumpy.

this inverted "v," leading to an apparent jump in velocity. In order to make this clear, two images of the phase front used to calculate the velocity are shown for various points in the graph. In figure 3-4b, the velocity of the phase front upon unloading is shown. Again, due to the appearance of small martensitic branches off of the primary phase front, the velocity is calculated by tracking the position of the phase front on a line down the center of the gage section of the sample, as shown in the schematic in figure 3-4b.

However, from a strain of nominally $\varepsilon_{YY}^{AVG} = 0.005 - 0.035$ upon loading and unloading, the band propagates as a single phase front with no branching. In figure 3-4c, this characteristic is exploited to calculate the velocity perpendicular to the angled phase front in the strain range where it is clearly delineated (no branching). Figure 3-4c shows the sum of the velocities of both sides of the martensitic phase front upon loading and unloading in the strain range where there exists a single, clearly delineated phase front. Although the top and the bottom of a single phase front can propagate at substantially different velocities (for example, note in the DIC images of full-field strain in figure 3-1 that upon loading, the top phase front stays relatively still, while it is only the bottom phase front that propagates), the *sum* of the two perpendicular velocities upon loading and unloading appears to stay nominally equal, which in this test is at a value of $V \approx 0.04$ mm/s. There are some preliminary indications that the sum of velocities of the phase front faces during loading may tend to be slightly faster than the sum of velocities during unloading; however, a detailed examination of the relationship of phase front velocities, as they depend on texture, strain rate, temperature, and other variables, necessitates an in-depth study and is left to future work.

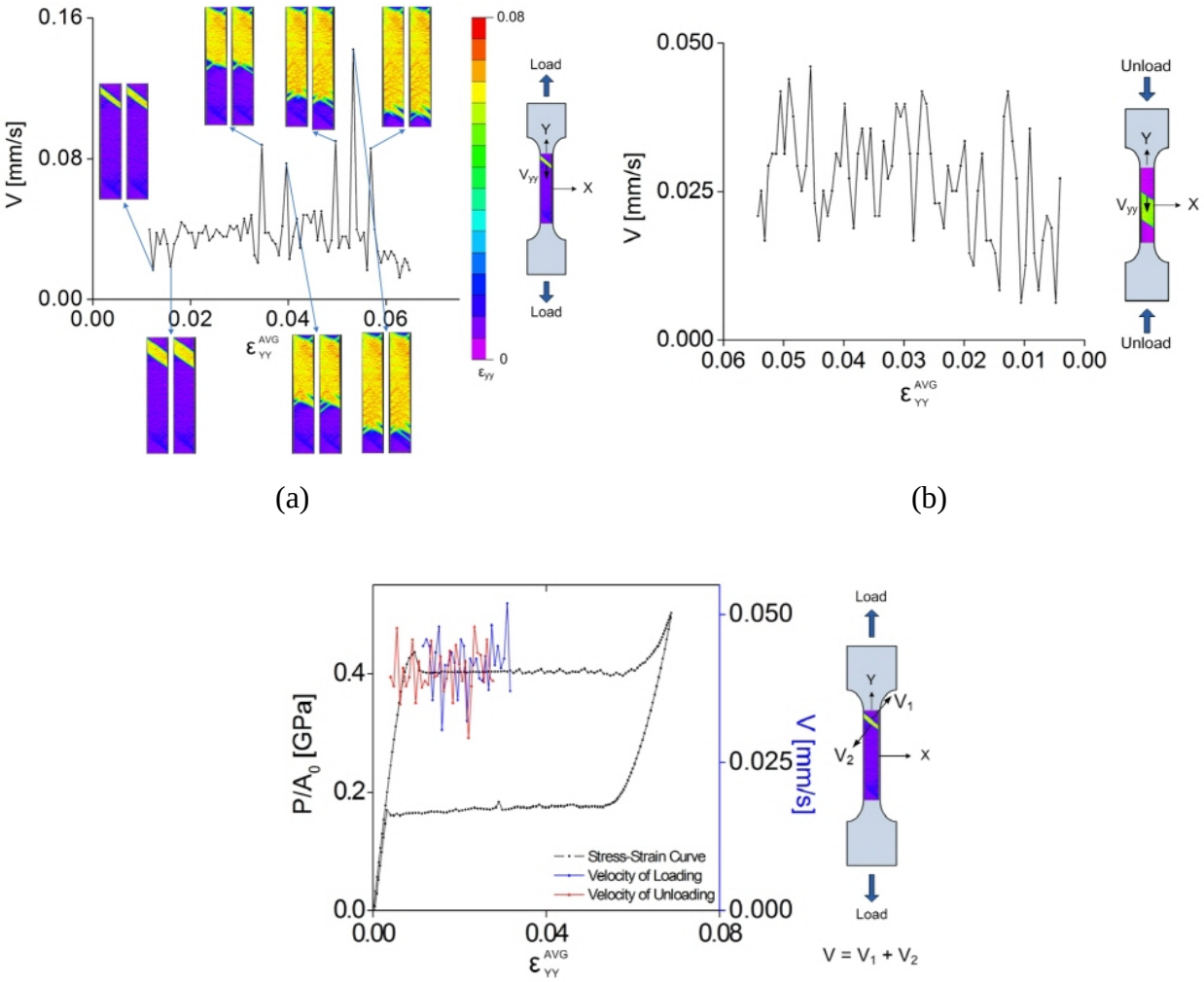

Figure 3-4 (a) The velocity of the phase transformation during loading in the uniaxial tension test described in figure 3-1. The velocity is calculated by tracking the position of the phase front on a line down the center of the gage section of the sample as shown in the schematic. (b) The velocity of the phase transformation during unloading in the uniaxial tension test described in figure 3-1. The velocity is calculated by tracking the position of the phase front on a line down the center of the gage section of the sample, as shown in the schematic. (c) The sum of the velocities of both sides of the martensitic front upon loading and unloading in the strain range where there exists a single, clearly delineated phase front (no branching). Although the top and the bottom of the phase front can propagate at different speeds, the sum of the two perpendicular velocities is nominally equal, here at a value of $V \approx 0.04\ mm/s$.

3.2. Strain Similarity

In the macroscopic stress-strain curves shown in figure 3-5a, the transformation stress decreases with pseudoelastic cycling, in agreement with results from prior work. This effect is generally attributed to local elastic stress fields developed during cycling that are attributed to changes in dislocation structure and/or the retention of martensitic nuclei [5-8]. It is generally known that stress-inducing martensite under mechanical cycling results in a decrease in the forward transformation stress with cycle number, while the reverse transformation stress decreases relatively at slow rate. The macroscopic cycling curve produced through spatially averaging DIC images clearly shows this tendency, as well as the characteristic decrease in hysteresis with an increase in cycle number. We observe that the total amount of residual plastic deformation increases, and the rate of accumulation of residual plastic deformation decreases, as cycling increases. These trends in the accumulation of residual plastic deformation are known phenomena that are attributed to the increase in dislocation hardening, and thus the critical stress required for slip, with the increase in cycle number (for example, see [9] and the discussion contained therein).

Figure 3-5b shows the full-field strains in the specimen at the mid-point of transformation for cycles 1, 2, 5, 10, 25 and 50, and figure 3-5c shows the corresponding IR-obtained thermal fields. There is sometimes a tendency of the martensitic band to “flip,” i.e. to nucleate and propagate from the opposite side of the specimen in a subsequent cycle. This occurs more frequently in the earlier cycles. However, even when the martensitic band has flipped to the other side of the specimen, as is the case from cycle 1 to cycle 2, and from cycle 5 to cycle 10 in figure 3-5b, note that the martensitic phase front maintains a similar profile.

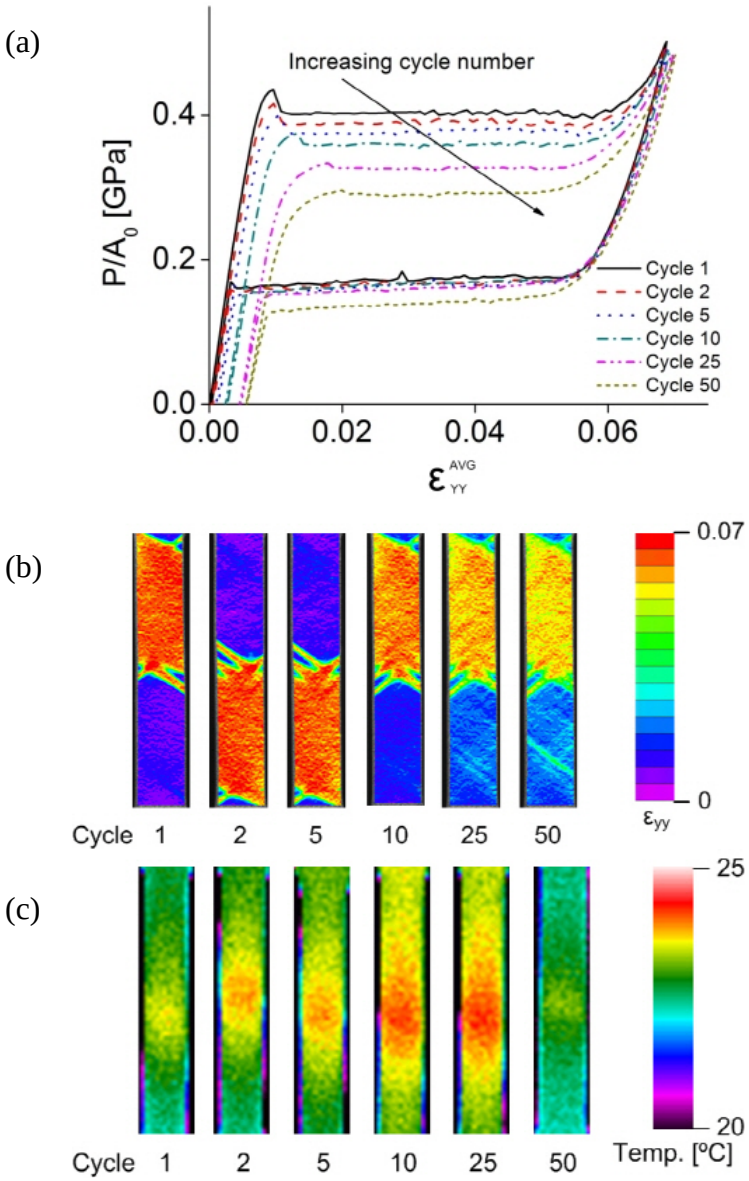

Figure 3-5 (a) Stress-strain curves in the gage section of an as-received nickel-titanium specimen loaded at $\dot{\varepsilon}_g = 10^{-4}$ s^{-1} under displacement control in a ramp profile, taken at cycles 1, 2, 5, 10, 25, and 50. The applied stress is obtained from the load cell and the strain along the axis of the specimen, ε_{YY}^{AVG}, is obtained by averaging approximately 600,000 values (330 x 1830 pixels) of ε_{yy} in each DIC image. (b) Full-field strains (ε_{yy}) in the specimen at the mid-point of transformation for cycles 1, 2, 5, 10, 25, and 50. (c) IR-obtained thermal fields corresponding to the full-field strains shown in (b)

As the cycle number increases, the martensitic phase transformation becomes increasingly homogeneous. The number of nucleation sites increases and the delineation of the phase front degrades. However, the degree of positional similarity for the bands is very strong; bands tend to nucleate in the same locations, and propagate in the same manner, from cycle to cycle. In order to investigate this tendency for strain similarity, let us examine two situations. In the first case (figure 3-6), the strain on a line down the center of the sample is captured during stress-induced martensitic phase transformation in an as-received specimen. Initially (figure 3-6-i) there is no macroscopic phase front, although the specimen is at a high, relatively uniform strain of 0.0095. The specimen is further loaded and the phase front nucleates and propagates (figure 3-6-ii to figure 3-6-iii), and eventually the stress-induced martensitic band has completely propagated through the gage section of the specimen (figure 3-6-iv). What is interesting to note here is that the accommodated strain in the martensite remains the same, even as loading is increased. For example, the martensite strain profile in figure 3-6-ii closely matches that in figure 3-6-iii, although the loading has increased and the martensitic band has propagated. Even with the increased amount of load and the propagation of the martensitic front, the accommodated strain in the martensite remains constant once it has formed.

In the second case, let us examine the axial strain on a line down the center of the sample at the mid-point of martensitic phase transformation, during cycle 1 and cycle 50 (figure 3-7). Figure 3-7a shows the macroscopic stress-strain curves for cycle 1 and 50, and the four points at which the centerline strain profiles are compared (labeled i-iv). These four points correspond to immediately after the large localized band appears (point (i)), during the martensitic band propagation (points (ii) and (iii)), and after the band has finished propagating throughout the gage section (point (iv)). The points between cycle 1 and 50 are chosen when the martensitic

band is at the same position in the gage section, determined through the full-field quantitative strain field maps. However, it is interesting to note that this exact choice of points on the macroscopic curve is not necessary in order to see the strain similarity effect. The strain similarity in the martensite phase is so strong and consistent throughout the loading that it is easily possible to see the strain similarity effect using the axial strain profile on quite different points during phase transformation.

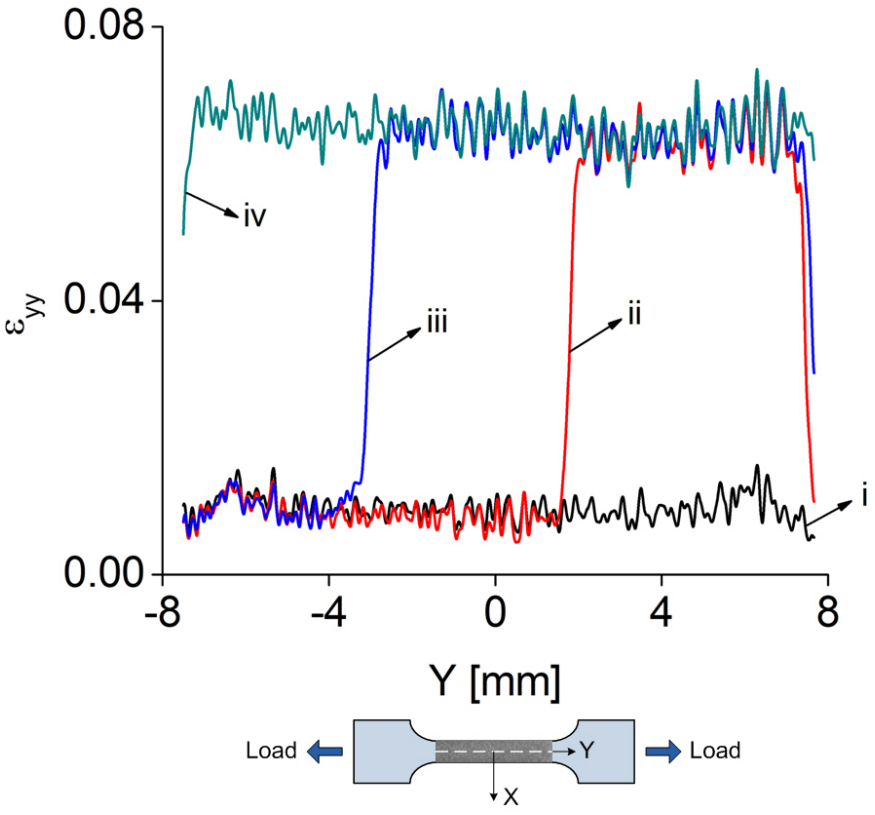

Figure 3-6 The strain (ε_{yy}) on a line down the center of the gage section during stress-induced martensitic phase transformation in an as-received specimen loaded at $\dot{\varepsilon}_g = 10^{-4}\ s^{-1}$ under displacement control in a ramp profile. The accommodation strain in the martensite remains the same, even as loading is increased and the phase front propagates.

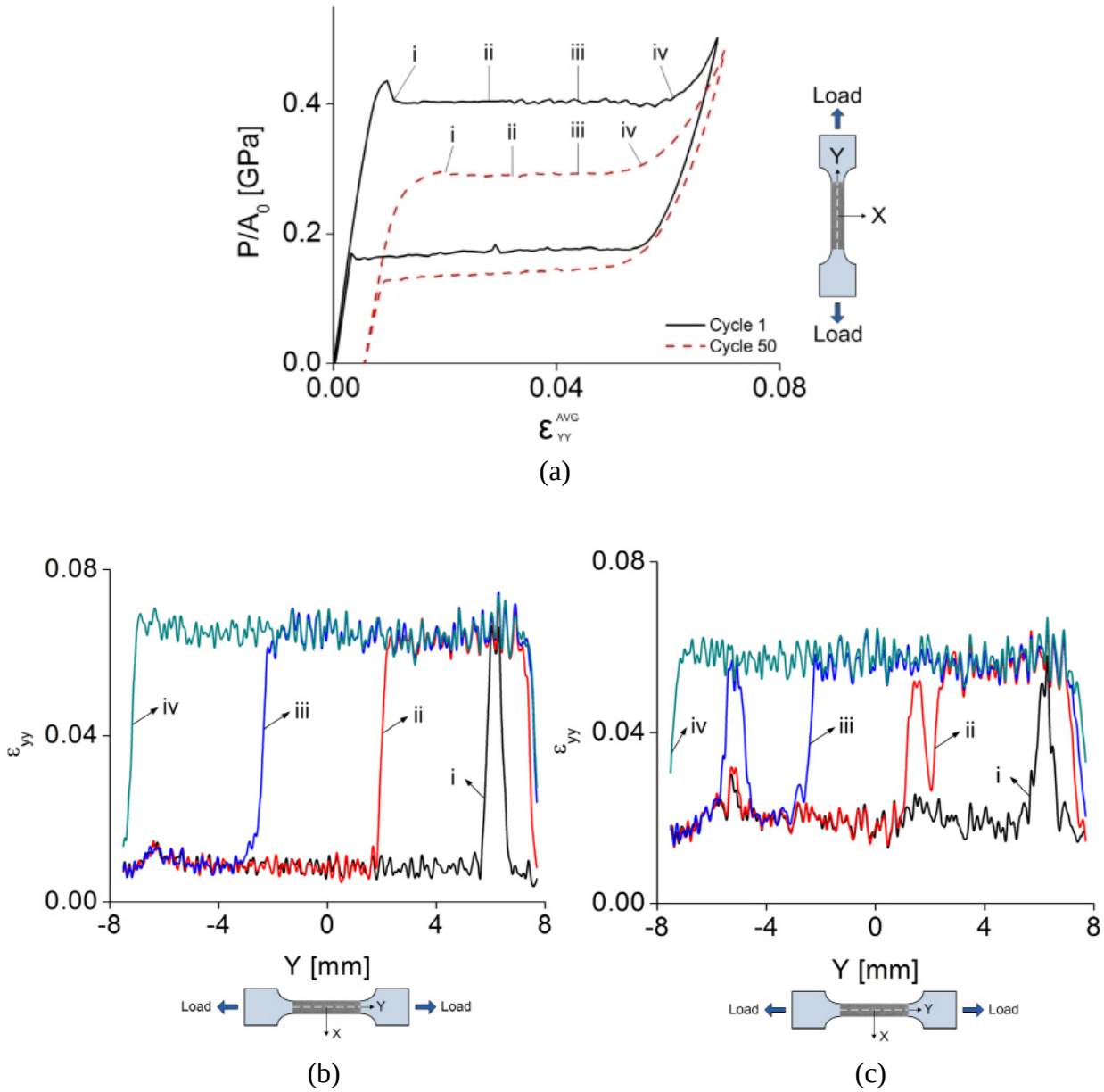

Figure 3-7 The axial strain on a line down the center of the sample at the mid-point of martensitic phase transformation, during cycle 1 and cycle 50. (a) shows the macroscopic stress-strain curves for cycle 1 and 50, and the points at which the centerline strain profiles are compared (labeled i-iv). (b) shows the strain profile at points i-iv in cycle 1, and (c) shows the strain profile at points i-iv in cycle 50. Note the homogenization of the phase transformation as the cycle number is increased.

Figure 3-7b shows the strain profile at points i-iv in cycle 1, and figure 3-7c shows the strain profile at points i-iv in cycle 50. Note the homogenization of the phase transformation as the cycle number is increased. In cycle 1 (figure 3-7b), the strain outside the martensitic band stays constant at nominally 0.008 and the strain inside the martensitic band is nominally 0.063. However, by cycle 50, the strain in the specimen is nominally 0.019 outside the martensitic band, and the strain inside the martensitic band is nominally 0.057. As the number of nucleation sites increases and the phase transformation becomes more homogeneous, the difference in the strain between the inside and outside of the band decreases by 30%, from ~0.055 (cycle 1) to ~0.038 (cycle 50). The increasing homogeneity with cycle number can be largely attributed to the advantageous formation of dislocation structures and the existence of residual pockets of martensite [5, 10-12].

The tendency of the strain in the martensite to stabilize within a loading cycle is again evident in figures 3-7b and 3-7c. If the strain profiles from cycle 1 and from cycle 50 are now overlaid with each other, there is also clear evidence of strain similarity in the martensite from *cycle to cycle* (figure 3-8). To display this cycle-to-cycle martensite strain pattern similarity, the strain profiles for cycles 1 and 50 are vertically shifted and compared at various points during the phase transformation (figure 3-7, points i-iv) in figure 3-8. At point i, which immediately follows nucleation, most of the specimen is austenite and there is little strain similarity in the strain field. In figure 3-8d, the band has completely propagated through the gage section and the specimen can be considered as fully martensite. (Note that although we classify outside the band as macroscopic ‘austenite’ and inside the band as macroscopic ‘martensite,’ this is a bit of a misnomer. As is discussed by Brinson et al. [13], martensitic transformation in fact occurs throughout the material at all strain levels, and it is not correct to consider the areas outside the

large localized bands as martensite-free, nor the areas inside the large localized bands as completely martensite.) In figure 3-8d (fully macroscopically martensite), the strain similarity between cycle 1 and cycle 50 is quite strong; the strain profiles overlay faithfully with each other. In figures 3-8b and 3-8c, mid-way through phase transformation, the strain similarity in the martensite is also quite faithful, while again there is significantly less strain similarity in the austenite. In order to quantitatively examine cycle-to-cycle strain similarity, correlation coefficients of the centerline strains between cycle 1 and 50 were calculated for two cases: (case 1) where the specimen was fully (macroscopically) austenite immediately prior to nucleation of localized band and (case 2) when the bands had finished propagating through the specimen and it was fully (macroscopically) martensite. The correlation coefficient indicates the amount of periodic similarity between the strains of two cycles regardless of differences in the strain magnitude, and is defined as the following. Here, an r value approaching 1 indicates a greater degree of similarity, A_{mn} and B_{mn} are the data sets for cycles 1 and 50 respectively, and $\overline{A}$ and $\overline{B}$ are the means of the respective data sets:

$$r = \frac{\sum_m \sum_n (A_{mn} - \overline{A})(B_{mn} - \overline{B})}{\sqrt{\left(\sum_m \sum_n (A_{mn} - \overline{A})^2\right)\left(\sum_m \sum_n (B_{mn} - \overline{B})^2\right)}}$$

The correlation coefficient of the centerline strains for the macroscopic austenite (case 1) between cycle 1 and 50 was 0.59 and that of the centerline strains for the macroscopic martensite (case 2) was 0.82. The strain accommodated by the stress-induced martensite exhibited significantly greater cycle-to-cycle similarity than the strain accommodated by austenite. This finding indicates that the initial manner in which the martensite accommodates strain in the first cycle strongly dictates how the martensite will accommodate strain in future cycles. Thus, one

can argue that the local elastic stress fields in the martensite are driven by a dislocation structure and martensitic nuclei that largely stabilize during the first loading cycle [5].

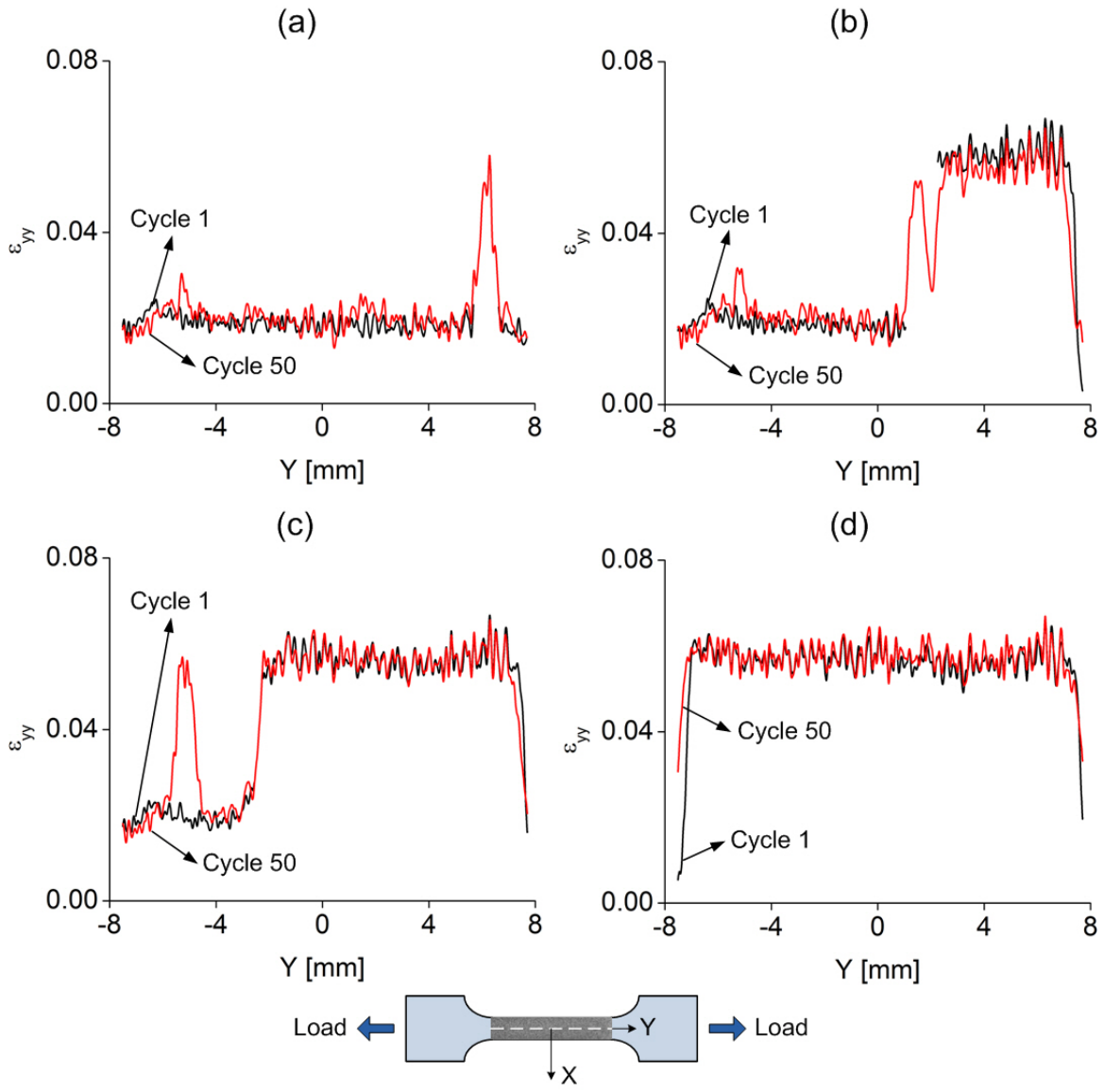

Figure 3-8 Overlay of strain profiles from cycle 1 and from 50, where strain profiles are taken on a line down the center of the gage section and the strain of cycle 50 is shifted vertically upward. There is clear evidence of strain pattern memory in the martensite phase from cycle to cycle. Figure (a) overlays the strain profiles for cycle 1 and 50 at point i, which is immediately following nucleation. Most of the specimen is macroscopically austenite at this point, and there is little similarity in the centerline strains. In figure 3-8d, the band has completely propagated through the gage section and the specimen can be considered as fully martensite. Here, the similarity in the centerline strains between cycle 1 and cycle 50 is quite strong.

3.3. Evolution of Martensitic Volume Fraction

The evolution of martensitic volume fraction across the gage section can be roughly estimated from the full-field strain data obtained by DIC. Figure 3-9a shows the macroscopic stress-strain curve for the first loading cycle on the specimen, as first described in figure 3-1. Lines of slope E_A (austenite Young's modulus) and E_M (martensite Young's modulus) are offset from the onset and saturation of transformation, respectively, by 0.1% in order to quantify the strains at which macroscopic phase transformation begins and saturates. A 0.1% offset of linearity method is used to determine consistent values for the start and completion of transformation, as the elastic modulus of austenite gradually decreases prior to nucleation of localized band and a similar nonlinearity is evident in the martensite modulus. This effect is due to the heterogeneous behavior of transforming grains at the microscale, which is reflected in the macroscopic stress-strain curve. Phase transformation preferentially begins at small sub-grain and grain-level pockets of austenite prior to appearing as large localized bands of transformed martensite as the applied loading is increased [13, 14]. Following this method, four relevant strains for the stress-strain curve are determined at each cycle: the 0.1% offset values for the (1) start of martensitic transformation on loading (ε_{AL}), (2) finish of transformation on loading (ε_{ML}), (3) start of transformation on unloading (ε_{MU}), and (4) finish of transformation on unloading (ε_{AU}). Note that these four representative values need to be determined following any change in loading or sample parameters, such as cycle number, initial crystallographic texture, or applied strain rate, as the macroscopic stress-strain curve will change. After obtaining these values for a specific experimental condition, each individual DIC image in the test is then evaluated in order to determine the extent of martensitic transformation in that image. To evaluate the martensitic volume fraction in a single DIC image, approximately 600,000 points in that image are

individually binned using a rule-of-mixtures approach. The overall martensitic volume fraction for the image is taken as:

$$\delta_M = \frac{N_M}{N_{Total}} \qquad \text{(Eqn. 1)}$$

where N_M is the amount of martensite in all of the pixels, and N_{Total} is the total number of pixels in the image. We consider the number of martensitic pixels as,

$$N_M = M_P + M_T \qquad \text{(Eqn. 2)}$$

where M_P is the number of pure martensite pixels and M_T is the summed martensitic fraction of the pixels that can be considered as partially martensite. During loading, M_P is defined as the sum of all pixels that have a strain $\varepsilon \geq \varepsilon_{ML}$, and M_T is defined as the sum of the martensitic fraction of pixels that have a strain $\varepsilon_{AL} < \varepsilon < \varepsilon_{ML}$, where

$$M_T = \frac{\varepsilon - \varepsilon_{AL}}{\varepsilon_{ML} - \varepsilon_{AL}} \qquad \text{(Eqn. 3)}$$

Similarly, during unloading, M_P is defined as the sum of all pixels that have a strain $\varepsilon \geq \varepsilon_{MU}$, and M_T is defined as the sum of the martensitic fraction of pixels that have a strain $\varepsilon_{AU} < \varepsilon < \varepsilon_{MU}$, where

$$M_T = \frac{\varepsilon - \varepsilon_{AU}}{\varepsilon_{MU} - \varepsilon_{AU}} \qquad \text{(Eqn. 4)}$$

Binning is performed for all the pixels in the image. For a simple example, consider the case where the offset values are ε_{AL}= 0.01 and ε_{ML}=0.06, and the strain value of one pixel in a

DIC image is 0.03. This single pixel would then, by the rule of mixtures, be binned as 40% austenite and 60% martensite. This procedure is repeated for the nominally 600,000 pixels in each image, and all of the values in each bin are summed in order to determine the final value for martensitic volume fraction (δ_M) for that image, taken at a specific point in the loading cycle. This entire procedure is then repeated for each image in the test in order to build up the evolution of δ_M as a function of applied stress (P/A_0). This approach results in the quantitative measures of the evolution of martensitic volume fraction shown in figure 3-9b (loading) and 3-9c (unloading). This method captures the salient features of the evolution of martensitic volume fraction, but there are sources of error that need to be discussed. Firstly, there is possible error in computing the four critical values (ε_{AL}, ε_{ML}, ε_{MU}, ε_{AU}) through the 0.1% offset of linearity method; to create the linear lines in loading and unloading, the linear curve fitting was used with a norm of residuals of 2.43 MPa. An important error to note comes from the assumption that a pixel is 100% martensite after it contains a strain greater than ε_{ML}. As shown by previous research and discussed in this paper (for example, see [13, 14] and the references contained therein), it is extremely likely that the pixel still contains a significant amount of residual austenite at strains greater than ε_{ML}. Because each analyzed pixel contains a large number of grains, the amount of residual austenite will be relatively consistent from pixel to pixel with respect to the strain within that pixel. However, it will not be negligible; therefore, what is referred to as 100% martensite or 100% austenite in the evolution of volume fraction should be considered as 100% martensite/austenite as defined by the macroscopic strain, rather than on the microstructural level.

The cycle number has a clear effect on the evolution of δ_M on loading, and substantially less effect on the evolution of δ_M upon unloading. This observation agrees with prior macroscopic observations that the reverse transformation stress decreases substantially with cycling upon loading, but stays nearly constant upon unloading. Similar to the macroscopic stress-strain curves, the nucleation or coalescence of bands has a direct impact on the evolution of δ_M, appearing as small but noticeable bumps in figures 3-9b and 3-9c.

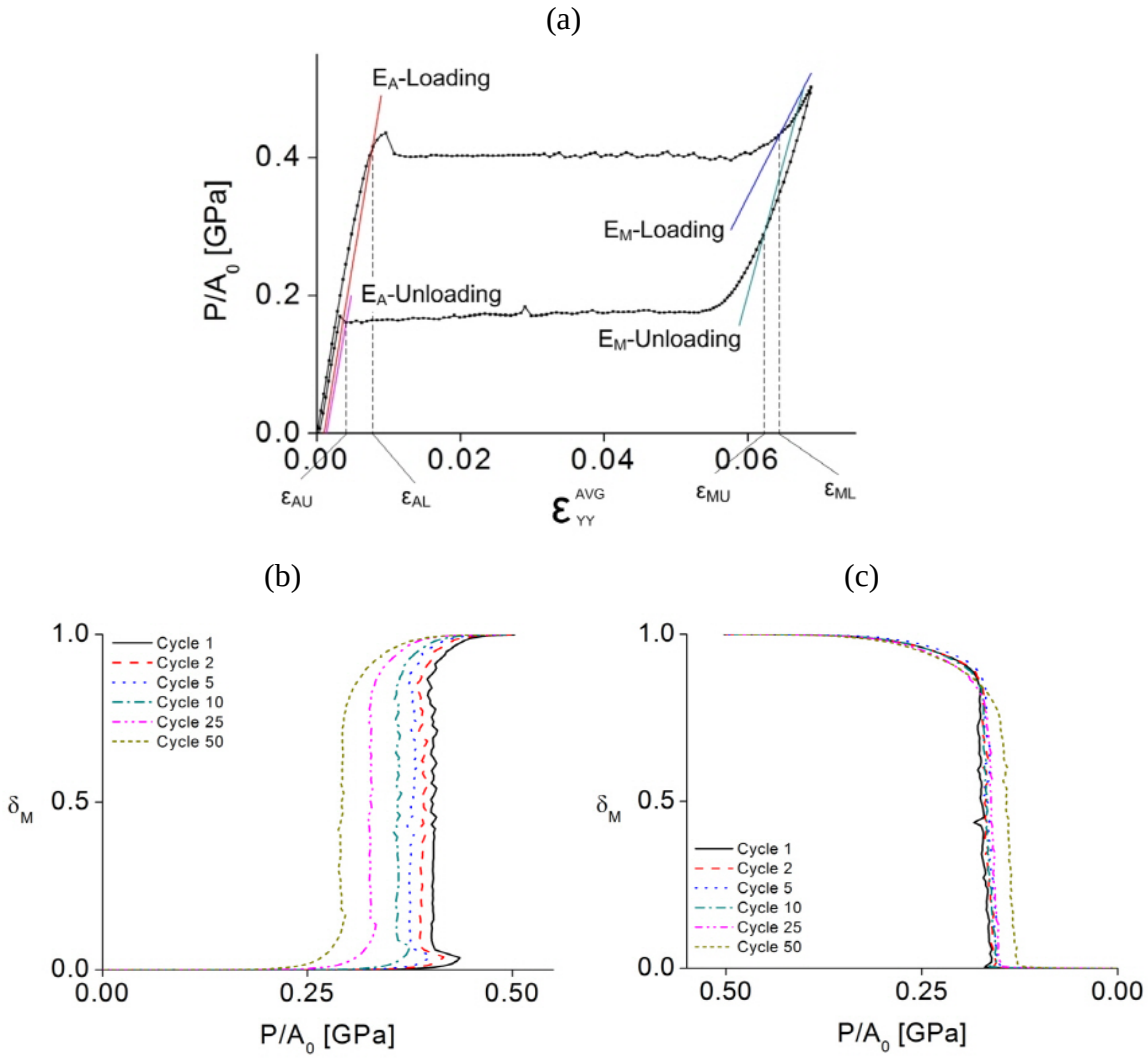

Figure 3-9 The evolution of martensitic volume fraction in the gage section during loading and unloading in a sample that is tested in uniaxial tension at $\dot{\varepsilon}_g = 10^{-4}$ s^{-1} under displacement control in a ramp profile.

3.4. Conclusions on Strain Similarity

Simultaneous three-dimensional digital image correlation and infrared imaging were used to examine stress-induced martensitic transformation in nickel-titanium during uniaxial, zero-to-tension loading at an applied strain rate of $\dot{\varepsilon}_g = 10^{-4}\ s^{-1}$. The effect of hard cyclic loading was examined, particularly the appearance of a strain pattern similarity in the macroscopically martensite region both within a cycle and from cycle to cycle. The following was determined:

- Stress-induced martensitic phase transformation can propagate either by a single, clearly delineated front, or alternatively by the offshoot of small branches from the primary phase front. A single martensitic front can change to a branched front in the middle of phase transformation, as shown in figure 3-1. The nucleation/coalescence of these small branches directly corresponds to a load drop/rise in the macroscopic stress-strain curve.
- Although the top and the bottom of a single phase front can propagate at substantially different velocities (for example, note in figure 3-1 that upon loading, the top phase front stays relatively still, while it is only the bottom phase front that propagates), the *sum* of the two velocities taken perpendicular to the phase front was found to be nominally equal upon loading and unloading in these tests.
- The accommodated strain in the microstructure of martensite that has already been formed will remain constant, even as loading is increased and the martensitic phase front propagates through the gage region (figure 3-6).
- The number of nucleation sites increases and the delineation of the stress-induced martensitic phase fronts decreases as cycle number is increased. However, although the transformation becomes more homogeneous during cycling, there is a remarkable amount of strain similarity

in the martensite from cycle to cycle. This can be seen in an overlay of the strain values down the centerline of the gage section from the 1st cycle on an as-received specimen and from the 50th cycle on the same specimen, as shown in figure 3-8. Note that the tendency to have strain similarity is much stronger in the stress-induced martensite (inside the localized band) than in the austenite (outside the localized band). This tendency is quantitatively shown by a higher correlation coefficient of the centerline strains for the martensite between cycles 1 and 50 than that for the austenite. This indicates that the initial manner in which the martensite accommodates strain in the first cycle strongly dictates how the martensite will accommodate strain in future cycles. Thus, one can argue that the local elastic stress fields in the martensite are driven by a dislocation structure and martensitic nuclei that largely stabilize during the first loading cycle.

- By using a rule-of-mixtures approach on the DIC-obtained full-field strains, the evolution of martensitic volume fraction across the gage section of the specimen as a function of the applied load can be roughly quantified and examined. The cycle number has a clear effect on the spatial evolution of δ_M on loading, and substantially less effect on the spatial evolution of δ_M upon unloading.

References

[1] M. A. Iadicola and J. A. Shaw, “The effect of uniaxial cyclic deformation on the evolution of phase transformation fronts in pseudoelastic NiTi wire,” *Journal of Intelligent Material Systems and Structures*, vol. 13, no. 2–3, pp. 143 –155, Feb. 2002.

[2] Y. Matsuzaki, H. Naito, T. Ikeda, and K. Funami, “Thermo-mechanical behavior associated with pseudoelastic transformation of shape memory alloys,” *Smart Mater. Struct.*, vol. 10, no. 5, p. 884, Oct. 2001.

[3] P. B. Entchev, and D. C. Lagoudas, “Modeling of transformation-induced plasticity in SMAs,” *In Shape memory alloys, Springer US*, pp. 233-277, 2008.

[4] S. Daly, G. Ravichandran, and K. Bhattacharya, “Stress-induced martensitic phase transformation in thin sheets of Nitinol,” *Acta Materialia*, vol. 55, no. 10, pp. 3593–3600, Jun. 2007.

[5] P. G. McCormick and Y. Liu, “Thermodynamic analysis of the martensitic transformation in NiTi-II. Effect of transformation cycling,” *Acta Metallurgica et Materialia*, vol. 42, no. 7, pp. 2407–2413, Jul. 1994.

[6] S. Miyazaki, T. Imai, Y. Igo, and K. Otsuka, “Effect of cyclic deformation on the pseudoelasticity characteristics of Ti-Ni alloys,” *MTA*, vol. 17, no. 1, pp. 115–120, Jan. 1986.

[7] E. Patoor, P. Barbe, A. Eberhardt, and M. Berveiller, “Internal stress effect in the shape memory behaviour,” *J. Phys. IV France*, vol. 01, no. C4, pp. 95–100, Nov. 1991.

[8] H. Sehitoglu, R. Anderson, I. Karaman, K. Gall, and Y. Chumlyakov, “Cyclic deformation behavior of single crystal NiTi,” *Materials Science and Engineering A*, vol. 314, no. 1–2, pp. 67–74, Sep. 2001.

[9] S. Miyazaki and K. Otsuka, “Development of shape memory alloys,” *ISIJ International*, vol. 29, no. 5, pp. 353–377, 1989.

[10] B. Strnadel, S. Ohashi, H. Ohtsuka, T. Ishihara, and S. Miyazaki, “Cyclic stress-strain characteristics of Ti-Ni and Ti-Ni-Cu shape memory alloys,” *Materials Science and Engineering A*, vol. 202, no. 1–2, pp. 148–156, Nov. 1995.

[11] B. Strnadel, S. Ohashi, H. Ohtsuka, S. Miyazaki, and T. Ishihara, “Effect of mechanical cycling on the pseudoelasticity characteristics of Ti-Ni and Ti-Ni-Cu alloys,” *Materials Science and Engineering A*, vol. 203, no. 1–2, pp. 187–196, Nov. 1995.

[12] R. DesRoches, J. McCormick, and M. Delemont, “Cyclic properties of superelastic shape memory alloy wires and bars,” *Journal of Structural Engineering*, vol. 130, no. 1, pp. 38–46, 2004.

[13] L. C. Brinson, I. Schmidt, and R. Lammering, “Stress-induced transformation behavior of a polycrystalline NiTi shape memory alloy: micro and macromechanical investigations via in situ optical microscopy,” *Journal of the Mechanics and Physics of Solids*, vol. 52, no. 7, pp. 1549–1571, Jul. 2004.

[14] M. Kimiecik, J. W. Jones, and S. Daly, “Quantitative studies of microstructural phase transformation in Nickel–Titanium,” *Materials Letters*, vol. 95, pp. 25–29, Mar. 2013.

Chapter 4

The Effect of Texture on Stress-Induced Martensitic Transformation in Nickel-Titanium

In this chapter, an experimental study was performed to investigate the effect of crystallographic texture on stress-induced martensitic phase transformation in the shape memory alloy nickel-titanium (Nitinol). Thin sheet specimens of Nitinol were examined under uniaxial tensile loading using three-dimensional digital image correlation in order to spatially and temporally track strain localization indicative of martensitic transformation. Tensile specimens were fabricated along directions oriented 0° (RD), 45°, and 90° (TD) to the rolling direction of the sheet and subjected to 50 cycles at prescribed strain rates of $\dot{\varepsilon}_g = 10^{-4}, 10^{-3}$, and $10^{-2} s^{-1}$. It was found that upon loading, specimens with crystallographic textures that were unfavorably oriented for transformation (TD specimens) nucleated a greater number of deformation bands due to a smaller difference between nucleation and propagation stresses, and also accommodated less axial strain inside the band and more axial strain outside of the band. The unfavorable (TD) specimens also exhibited a stronger cycle-to-cycle similarity in the strain accommodated inside the band. Finally, the (primarily martensite) region of the deformation band(s) consistently showed significantly stronger cycle-to-cycle similarity than the (primarily austenite) region outside of the band(s), regardless of specimen texture.

4.1 Characterization of Specimen Crystallographic Texture

Optical micrographs of three specimens cut parallel (RD), 45°, and perpendicular (TD) to the rolling direction of the sheet are shown in figure 4-1. It was determined by X-ray diffraction (XRD) that the RD specimens had a {110} texture, which is a favorable orientation for large recoverable transformation strains [1, 2]. These specimens also showed the largest recoverable strain under the uniaxial loading imposed in these tests. The 45° specimen had a texture that was favorably oriented for large recoverable transformation strains as well, though with a slightly smaller intensity than the RD. The TD specimens had a significantly less favorable texture for transformation strain (and correspondingly exhibited the shortest transformation plateau in the macroscopic stress-strain curves shown in figure 4-5).

X-ray diffraction of the as-received material revealed the presence of the two dominant peaks shown in figure 4-2; a major peak intensity at $2\theta=42.36°$ and a second peak intensity at $2\theta=77.48°$, which correspond to the (110) and (211) planes in the parent austenite phase, respectively. Strong texture in the (110) plane in cold-rolled NiTi has also been observed in

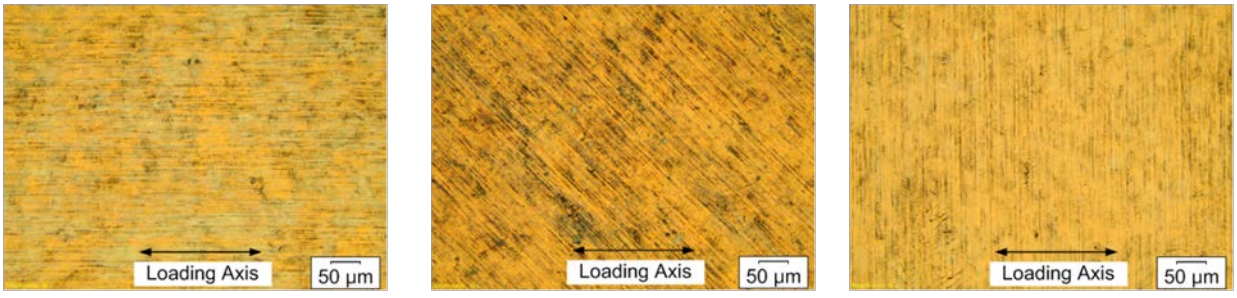

(a) (b) (c)

Figure 4-1 Optical micrographs of the textured surfaces at specimens cut at (a) RD, (b) 45°, and (c) TD to the rolling direction of the as-received sheet.

previous research on NiTi plates [2-4]. Note that the minor third peak intensity at 2θ=43.36° was determined to be (200) of a TiO surface oxide. The {111}, {100}, and {110} pole figures of the test material were obtained by orientation density functions calculated by MTEX and are shown in figure 4-3a through 4-3c respectively. The test specimens possessed a small average grain size on the order of tens to hundreds of nanometers (nominally 40nm as measured with the Scherrer equation). Note that there was some overlap between differently oriented grains in the pole figures because of the large diffraction spot size to grain size ratio. The pole figures and inverse pole figures indicate that the orientations of most grains were $\{111\}[\bar{1}10]$ and $\{110\}[\bar{1}10]$, with the {h k l} plane parallel to the sample surface and the [u v w] direction parallel to RD.

The orientation of the crystallite axis in the specimen is known to significantly affect transformation strain in thin rolled plates and sheets [1, 2]. Miyazaki et al. theoretically

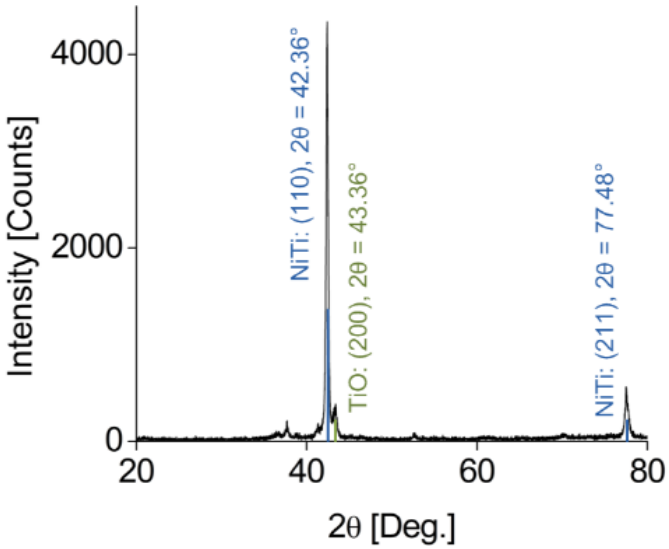

Figure 4-2 X-ray diffraction analysis of the as-received NiTi sample**.** There is a major peak intensity at 2θ=42.36° and a second peak intensity at 2θ=77.48°, which correspond to the (110) and (211) planes in the parent austenite phase, respectively.

calculated this dependence of transformation strain during martensitic transformation, projected on a $[001]-[011]-[\bar{1}11]$ standard stereographic triangle. The recoverable strain was found to depend on whether the crystallite axes were preferentially located around the $[011]-[\bar{1}11]$ line of this orientation dependent transformation strain map [1]. Similarly, the transformation strain became small if the crystallite axes were preferentially located around the $[001]$ direction. This map [1] was calculated by using the lattice parameters of the austenite and martensite phases to compute lattice distortion due to martensitic transformation, where it was assumed that the most favorable martensite variant grows to induce the maximum transformation strain in each grain. A similar map was constructed in [2], where higher transformation strains were again calculated along the $[011]-[111]$ line and inhibited transformation strain calculated along the $[001]$ direction. Larger recoverable strains observed in some of the calculated versus experimentally measured results in [2] were attributed to the introduction of permanent strain via slip; also, differences in the recoverable strain versus orientation curves were attributed to constraints becoming more pronounced as the quantity of grain boundaries increased near TD. Note that this orientation

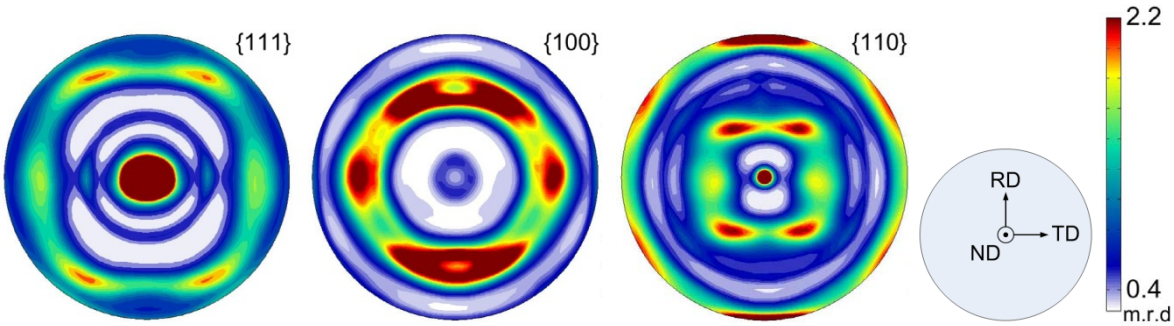

Figure 4-3 The pole figures obtained by orientation density functions of (a) $\{111\}$, (b) $\{100\}$, and (c) $\{110\}$ are shown with a legend of intensity, multiple of a random distribution (m.r.d). Specimen coordinates of the pole figures are shown at right. Strong intensities appear at RD and 45° in the $\{110\}$ pole figure.

dependence of the transformation strain was only found for thin rolled plates and sheets; in sputter-deposited thin films, transformation strain was found to be nearly independent of in-plane direction.

Following these calculations, diffraction studies of the RD and 45° test specimens indicated that they had crystallographic textures favorably oriented for large transformation strains, and that the TD specimen had a crystallographic texture that was relatively unfavorably oriented for transformation. Inverse pole figures of the test specimens were experimentally

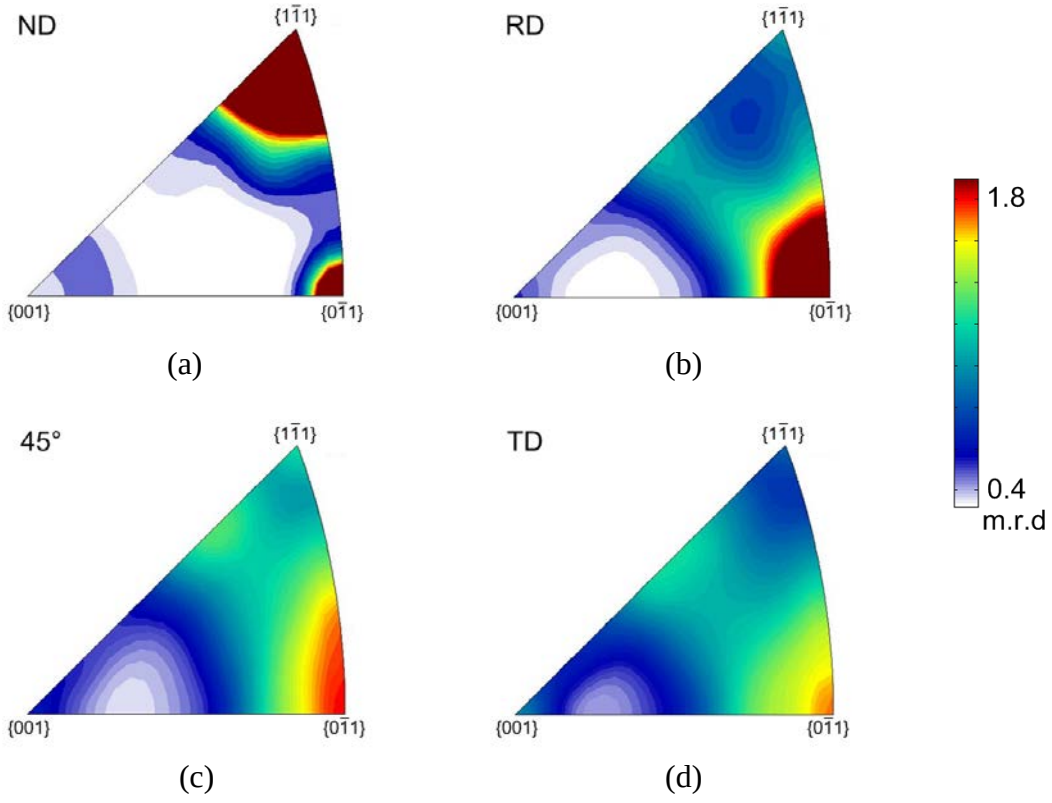

Figure 4-4 The inverse pole figures of the (a) normal direction to the surface (ND); (b) rolling direction (RD); (c) 45° direction; and (d) transverse direction (TD). In plane, the density of $\{0\bar{1}1\}$ is the highest at RD and decreases as the angle approaches TD; the density of $\{001\}$ is the lowest at RD and increases as the angle approaches TD.

obtained to examine the crystallite axis density distributions along specific directions, and are shown in figure 4-4. The RD inverse pole figure in figure 4-4b showed a high density around $\{0\bar{1}1\}$ and $\{1\bar{1}1\}$. The highest density of $\{0\bar{1}1\}$ was observed for RD and decreased as the in-plane angle approached 90° (TD). Conversely, the intensity of $\{001\}$ was lowest at RD and increased as the in-plane angle approached 90° (TD). This finding is in agreement with the macroscopic stress-strain responses shown in figure 4-5, where the TD orientation shows a markedly lower transformation strain.

4.2 Effect of Crystallographic Texture and Applied Strain Rate on Stress-Strain Response and Localization

The macroscopic stress-strain response of a TD specimen was markedly different from the RD and 45° responses at all strain rates studied here, requiring a higher load to nucleate and propagate martensite, and exhibiting a transformation plateau with a shorter length and a smaller strain at completion. Details of strain rate effects are well explained in Shaw and Kyriakides [5]. Macroscopic stress-strain responses are shown in figure 4-5 for globally applied strain rates of $\dot{\varepsilon}_g = 10^{-4}, 10^{-3}$, and $10^{-2} s^{-1}$. Each strain value on the x-axis (ε_{YY}^{AVG}) is an average of the DIC-measured full-field strains (ε_{yy}) in the gage section at a given global stress (y-axis), where P is the applied load measured by the load cell and A_0 is the reference cross-sectional area of the specimen. At a set strain rate, the macroscopic stress-strain curves of the RD and 45° specimens were nominally similar. These characteristics are consistent with the crystallographic textures of the RD and 45° specimens, which were found to be favorably oriented for large transformation strains (long transformation plateaus), and with the assertion that crystallographic texture is an

important factor in determining the propensity of a SMA to transform [6]. It was determined through IR measurements that crystallographic texture did not significantly affect the amount of released/absorbed latent heat during phase transformation.

As seen in table 4-1, the macroscopic (averaged) strain at the start of phase transformation in the TD specimen was higher than in the RD and 45° specimens at all strain rates. Because it was not possible to assess the exact strain at which the first band nucleated due to the discrete nature of the imaging, and it is likely that the amount of microscale martensite that accumulated prior to band nucleation depended on crystallographic texture, the initiation strain of the A → M transformation was obtained using a 0.1% offset from linearity of the elastically loaded austenite. A schematic of this method is shown in figure 4-6. The larger macroscopic strain at the start of transformation in TD specimens is reasonable given its unfavorable crystallographic texture. The globally applied stress at the start of transformation (σ_{MS}), and its dependence on cycling, is shown in figure 4-7.

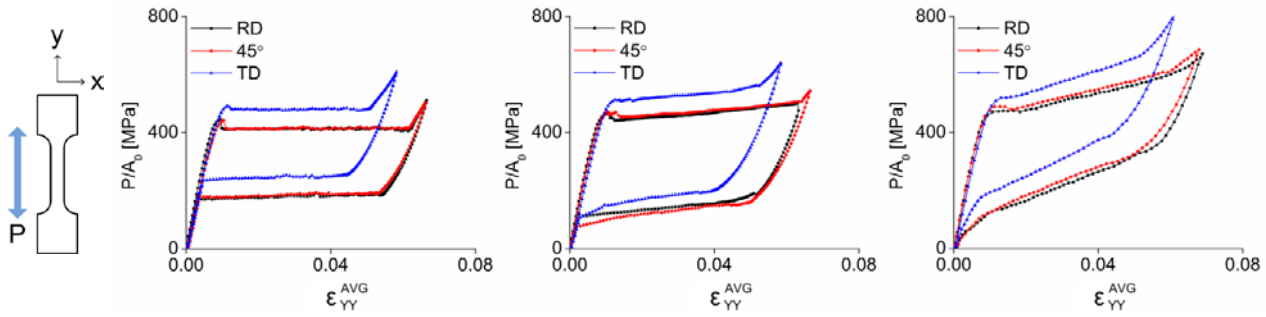

Figure 4-5 Macroscopic stress vs. DIC-averaged strain curves of textured specimens (cycle1) at the applied strain rate of (a) $\dot{\varepsilon}_g=10^{-4}$ s^{-1}, (b) $\dot{\varepsilon}_g=10^{-3}$ s^{-1}, and (c) $\dot{\varepsilon}_g=10^{-2}$ s^{-1}. The TD specimen requires higher stress to nucleate and propagate martensitic bands. Martensite band nucleation and propagation in the TD specimen starts at a higher averaged strain value and completes at a lower averaged strain value than in the RD and 45° specimens.

Table 4-1 Averaged strain values at the start of phase transformation, calculated by 0.1% offset from the linear austenite region in the stress-strain curve at cycle 1. Phase transformation in the TD (unfavorable) specimen begins at higher (averaged) strain values than in the RD and 45° specimens, for all applied strain rates.

Strain Rate	Texture	ε_{YY}^{AVG} at beginning of phase transformation [%]
$\dot{\varepsilon}_g = 10^{-4}\ s^{-1}$	RD	0.76
	45°	0.84
	TD	0.94
$\dot{\varepsilon}_g = 10^{-3}\ s^{-1}$	RD	0.81
	45°	0.86
	TD	0.97
$\dot{\varepsilon}_g = 10^{-2}\ s^{-1}$	RD	0.81
	45°	0.82
	TD	0.95

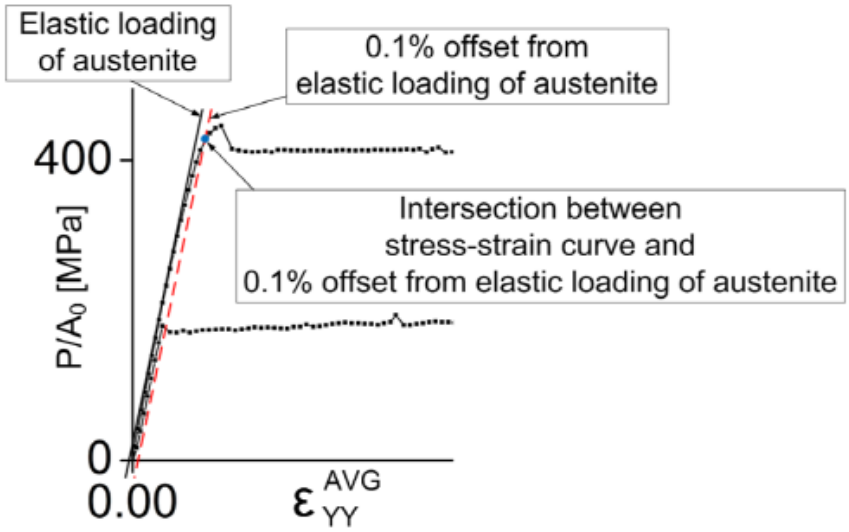

Figure 4-6 Schematic of the 0.1% offset from linearity used to calculate the average strain values (ε_{YY}^{AVG}) at the start of martensitic transformation, tabulated in table 4-1.

In addition to these characteristics, the accumulated residual strain was smallest for the TD specimen. The effect of cycling on the accumulation of residual strain (ε^P) is shown in figure 4-8. Note that a small amount of bending was apparent in the unloaded specimen due to accumulated plasticity, which created a slight nonlinearity in the stress-strain curve at the tail end of unloading; thus, residual strain was calculated using the intersection between the linearly extended stress-strain line and the x-axis. Even though transformation is inhibited for the TD specimen, there is a small residual strain accumulation likely due to low Schmid factors for slip. For a similar cold-rolled nickel-titanium TD sheet specimen, Mulder et al. found that the possible slip Schmid factors were close to zero [7]. Similarly, Chang and Wu [3] also measured a low accumulation of residual strain in unfavorably textured specimens.

The unfavorably oriented (TD) specimens also tended to nucleate a greater number of deformation bands than the RD and 45° specimens at a given strain rate, and this behavior became more pronounced at faster strain rates. This is evident in the full-field strain maps of the

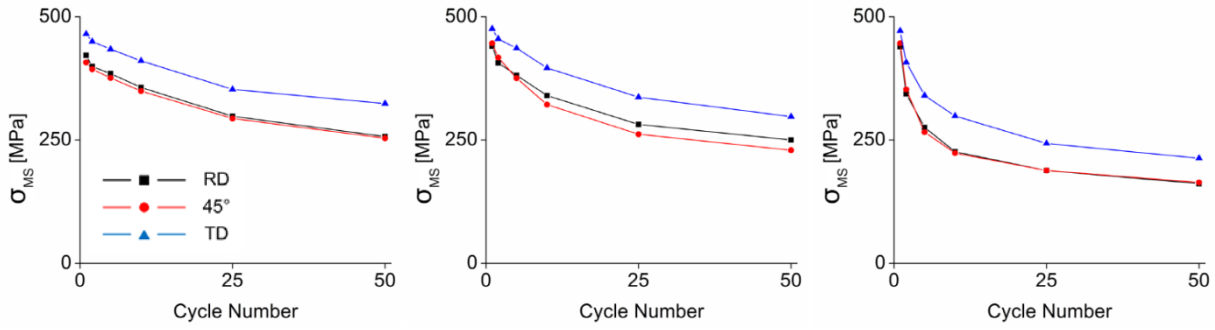

Figure 4-7 Stress required for the onset of stress-induced martensitic phase transformation at globally applied strain rates of (a) $\dot{\varepsilon}_g=10^{-4}$ s^{-1}, (b) $\dot{\varepsilon}_g=10^{-3}$ s^{-1}, and (c) $\dot{\varepsilon}_g=10^{-2}$ s^{-1}. The transformation stress is calculated by a 0.1% offset from linearity.

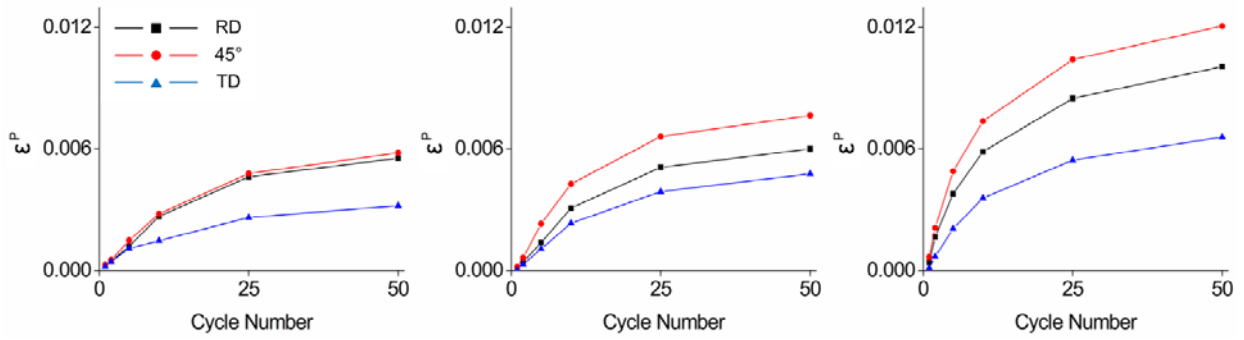

(a) (b) (c)

Figure 4-8 Residual strain at the applied strain rate of (a) $\dot{\varepsilon}_g = 10^{-4}\ s^{-1}$, (b) $\dot{\varepsilon}_g = 10^{-3}\ s^{-1}$, and (c) $\dot{\varepsilon}_g = 10^{-2}\ s^{-1}$.

sample gage section shown in figure 4-9. The strain fields were obtained when the specimen was in the middle of the phase transformation plateau during loading on the first cycle. High strain regions indicate primarily stress-induced martensite, and low strain regions indicate regions of primarily austenite. Note that each pixel contains hundreds of grains (the pixel resolution was 9 μm), and individual grains can and usually do contain both austenite and martensite [8, 9]. Thus, each point value in these strain fields represents an averaged contribution from both the austenite and martensite phases. As the applied stress level initially increased from zero, small sub-grain and grain-level pockets of austenite began to transform to martensite prior to the nucleation of a large macroscopic band, as first observed by Brinson et al. [8]. When the applied stress reached a critical level, large localized bands of strain nucleated and propagated; these martensitic fronts are clearly visible in figure 4-9.

The propensity of a TD specimen to nucleate more martensitic bands than RD or 45° specimens at a given strain rate arises from a dependence on crystallographic texture of the difference between the nucleation and propagation stresses. For $\dot{\varepsilon}_g = 10^{-4} s^{-1}$ and $10^{-3} s^{-1}$, the

nucleation stress (σ_N) was defined as the maximum stress prior to the onset of the first deformation bands (note all bands nucleated near the fillets but in the gage section), and the propagation stress (σ_P) was defined as the reduced value observed after nucleation of the first band. However, at $\dot{\varepsilon}_g = 10^{-2} s^{-1}$ it became difficult to define the nucleation and propagation stresses because of the nearly simultaneous nucleation of multiple fronts. Thus, the nucleation stress for $\dot{\varepsilon}_g = 10^{-2} s^{-1}$ is defined as the stress where the multiple fronts (near simultaneously) nucleated, and the propagation stress is defined as the stress where the multiple fronts (near simultaneously) began to propagate. Note that at the applied strain rate of $\dot{\varepsilon}_g = 10^{-2} s^{-1}$, five and four fronts nucleate simultaneously in the RD and the 45° specimens respectively – thus, in this case, a larger stress drop is observed in the 45° specimen than in the RD specimen. Finally, note that (σ_N - σ_P) for the TD specimen at $\dot{\varepsilon}_g = 10^{-2} s^{-1}$ was unable to be determined due to the continuous nucleation of

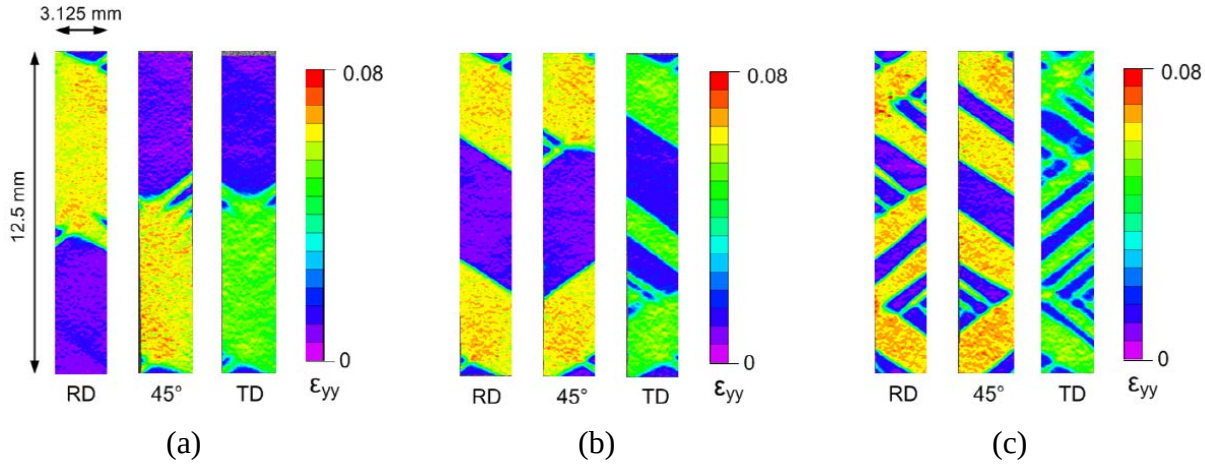

Figure 4-9 Full-field local strain maps of the gage section at cycle 1 at the middle of the phase transformation plateau at the applied strain rate of (a) $\dot{\varepsilon}_g = 10^{-4} s^{-1}$, (b) $\dot{\varepsilon}_g = 10^{-3} s^{-1}$, and (c) $\dot{\varepsilon}_g = 10^{-2} s^{-1}$. Though the number of deformation bands increases with faster strain rates, the TD specimen shows greater number of deformation bands at a given strain rate.

numerous new fronts that resulted in no clear delineation between the two values. The stresses required for nucleation (σ_N) and propagation (σ_P) of the martensite are calculated in table 4-2. At a set strain rate, the TD specimen exhibited both higher nucleation (σ_N) and propagation (σ_P) stresses than the RD and 45° specimens. However, the difference between these stresses (σ_N - σ_P) was substantially smaller, as shown in table 4-2. The smaller (σ_N - σ_P) difference resulted in the TD specimen being more inclined to nucleate a new deformation band in a cooler location, rather than propagate an existing deformation band in a location that had accumulated latent heat. Although accumulated latent heat will trigger the nucleation of multiple bands as the strain rate increases regardless of texture [5] (for example, see figure 4-9), the number of deformation bands is greatest in the TD specimen.

Table 4-2 The stress required to nucleate (σ_N) and propagate (σ_P) deformation bands of primarily martensite during loading at cycle 1. At a given strain rate, the TD specimen requires higher stresses for band nucleation and propagation than the RD and 45° specimens, but exhibits a smaller difference between stresses (σ_N - σ_P). This smaller (σ_N - σ_P) leads to a greater number of deformation bands, as the TD specimen is more willing to nucleate a new front in a cooler location rather than try to propagate an existing front in a location that has accumulated latent heat.

Strain Rate	Texture	σ_N [MPa]	σ_P [MPa]	σ_N - σ_P [MPa]
$\dot{\varepsilon}_g = 10^{-4}\ s^{-1}$	RD	445	411	34
	45°	443	412	31
	TD	492	480	12
$\dot{\varepsilon}_g = 10^{-3}\ s^{-1}$	RD	467	450	17
	45°	473	460	13
	TD	513	511	2
$\dot{\varepsilon}_g = 10^{-2}\ s^{-1}$	RD	475	472	3
	45°	490	479	11
	TD	520	N/A	N/A

During stress-induced martensitic transformation, the TD specimen exhibited more axial (ε_{yy}) strain outside the localized (primarily martensite) deformation band, and less axial strain inside the band, compared to the more favorably orientated RD and 45° specimens. Otherwise stated, in the TD specimen, a 'less strained' band propagated through a 'more strained' matrix during loading. This was true at all three globally applied strain rates. One possible cause for this is the low Schmid factors for both slip and transformation in the TD specimen. An increased number of non-transforming grains and grain clusters in the TD specimen would result in a more constrained transformation landscape, where individual pockets of martensite could still nucleate in the austenite region, but saturation of martensitic transformation in the deformation band would occur at lower strains. Additionally, the low Schmid factors for both transformation and slip may limit any synergistic interactions between the two mechanisms. However, these are hypotheses that need to be explored with studies on the length scale of the microstructure, currently under investigation. The range of all pixel strain values taken inside and outside of the deformation band(s), where each pixel encompassed hundreds of grains, are shown in table 4-3 at globally applied strain rates of $\dot{\varepsilon}_g = 10^{-4}s^{-1}$, $10^{-3}s^{-1}$, and $10^{-2}s^{-1}$. Pixel strain ranges were determined when the specimen was in the middle of the phase transformation plateau during the first loading cycle, where the averaged ε_{YY}^{AVG} = 3.77%, 3.67%, and 3.25% for RD, 45° and TD specimens, respectively. The macroscopically austenite region in the TD specimen accommodated an average strain of 1.1%, versus an average strain of 0.9% in the RD and 45° specimens. Conversely, the macroscopically martensite region in the TD specimen accommodated an average strain of 5.1%, versus an average of 6.2% in the RD and 45° specimens. In all cases, the strains were spatially heterogeneous, with the minimum and maximum pixel strain values varying by as much as a factor of 18.

Table 4-3 The range of strain values observed in individual pixels (each pixel encompassing hundreds of grains), as well as averaged across the region, outside and inside of the localized deformation band during loading at cycle 1. Strains are spatially heterogeneous, exhibiting a large range of pixel strain values. When the specimen had an unfavorable crystallographic texture for martensitic transformation (TD), smaller average strains were observed inside the (primarily martensitic) deformation band and larger average strains were observed outside the deformation band.

Strain Rate	Texture	Axial Strain Outside Deformation Band (Macroscopically Austenite) Min. – Max. (Avg.) [%]	Axial Strain Inside Deformation Band (Macroscopically Martensite) Min. – Max. (Avg.) [%]
$\dot{\varepsilon}_g = 10^{-4}\ s^{-1}$	RD	0.4 – 1.5 (0.9)	4.9 – 7.3 (6.2)
	45°	-0.3 – 2.1 (0.9)	4.7 – 7.6 (6.2)
	TD	0.4 – 1.8 (1.1)	3.5 – 6.2 (5.1)
$\dot{\varepsilon}_g = 10^{-3}\ s^{-1}$	RD	0.3 – 1.5 (0.9)	5.5 – 7.2 (6.3)
	45°	0.2 – 1.5 (0.9)	5.4 – 7.3 (6.3)
	TD	0.6 – 1.9 (1.3)	3.7 – 6.3 (5.1)
$\dot{\varepsilon}_g = 10^{-2}\ s^{-1}$	RD	0.1 – 1.7 (1.0)	4.3 – 10.1 (6.4)
	45°	0.1 – 1.8 (1.0)	5.3 – 7.4 (6.3)
	TD	0.7 – 2.5 (1.4)	3.3 – 6.8 (5.0)

4.3 Effect of Crystallographic Texture and Applied Strain Rate on Cyclic Strain Similarity

A strong similarity in the strains incurred by stress-induced (primarily martensite) regions of localized deformation was observed from cycle to cycle in chapter 3 [10], indicating that the manner in which the localized martensitic deformation accommodates strain in the first loading cycle strongly dictates how it will accommodate strain in future cycles. In this chapter, the dependence of this cyclic strain memory on crystallographic texture and strain rate is examined in both the (primarily martensite) region inside the deformation band and the (primarily austenite) region outside of the band. Recall that although the stress-induced deformation band(s)

are largely martensite, they do contain a significant amount of untransformed austenite. Similarly, although the regions outside of the deformation band are largely austenite, they contain a significant amount of transformed martensite [8, 9]. Thus, we will refer to the regions as "(primarily) martensite" and "(primarily) austenite" in the analysis below and we urge the reader to remember that we are referring to regions that are mixed in their composition. It was found that the strain accommodated by the (primarily) martensite region exhibited a greater cycle-to-cycle similarity in the unfavorably oriented (TD) specimen than in the RD and 45° specimens. Additionally, the (primarily) martensite region consistently showed much stronger cycle-to-cycle similarity than the (primarily) austenite region, regardless of specimen crystallographic texture. Finally, the strain similarity in the (primarily) martensite region evolved with cycling for all specimens and strain rates. For example, the similarity between cycles 25 and 50 was larger than the similarity between cycles 1 and 50, indicating that dislocation networks and the retention of martensitic nuclei continued to evolve, although at a reduced rate, as cycling progressed.

DIC-calculated strains on a vertical line down the center of the specimen at the 1^{st} and 50^{th} cycles were examined when: the specimen was fully (primarily) austenite before band nucleation; during stress-induced deformation band propagation; and after the specimen was fully (primarily) martensite. The phases are denoted here as (primarily) austenite and (primarily) martensite as a reminder that there exist microscopic pockets of martensite in the macroscopically austenite region prior to band nucleation, and there also exist microscopic pockets of austenite in the transformed deformation band, as observed in [8, 9]. Strains down the centerline of the specimen at cycle 1 and 50, after the deformation band(s) had fully propagated through the specimen, are shown in figure 4-10 for the three crystallographic textures. The

strains are taken down the dotted line shown in the sample schematic to the bottom right of figure 4-10. The cycles are shifted and overlaid for clear comparison of their strain profiles, since only the trend/similarity of the accommodated strain, and not the magnitude, is under

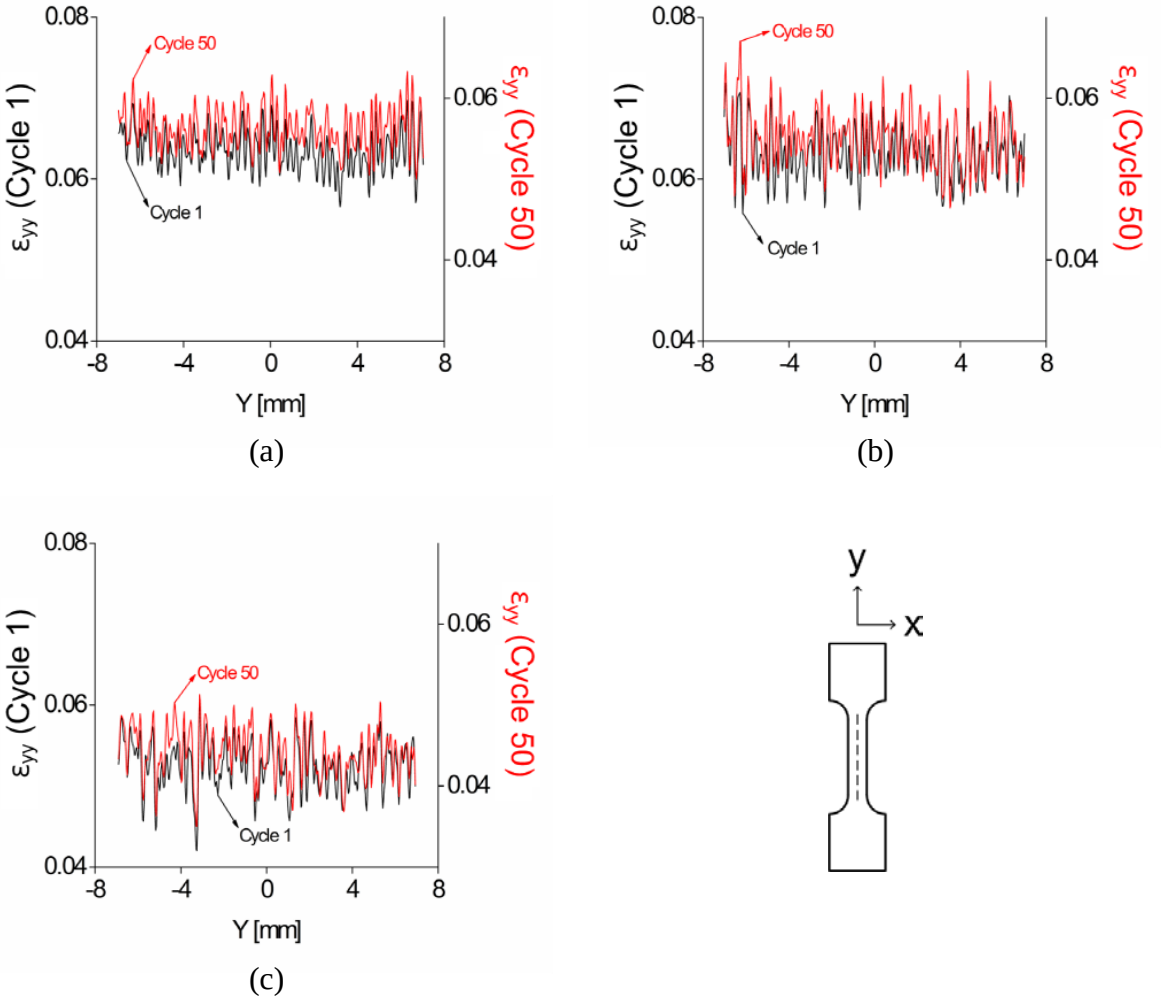

Figure 4-10 Axial strains for cycle 1 and 50 of (a) RD, (b) 45°, and (c) TD specimens at a globally applied strain rate of $\dot{\varepsilon}_g = 10^{-4}\ s^{-1}$, taken when the specimen is fully (macroscopically) martensite. The strain is taken on a vertical line down the center of the sample as shown by the dotted line in the sample schematic. The strain profiles for cycle 1 and 50 are shifted and overlaid, since only the profile and not magnitude is under consideration. The strain accommodated by the (macroscopically) martensite phase shows significant similarity from cycle to cycle for all textures, and particularly for the TD specimen. Correlation coefficients between the cycle 1 and 50 profiles are calculated in table 4-4.

consideration here. The left vertical axis shows the axial strain values for the first cycle and the right vertical axis shows the axial strain values for the 50th cycle. Note that each point on these profiles represents the averaged strain of hundreds of grains, and thus contains an averaged contribution from both martensite and austenite phases.

In order to compare the effect of texture on the amount of strain similarity between cycle 1 and 50, correlation coefficients of the centerline strain profiles from cycle 1 and 50 were calculated and are shown in table 4-4. The correlation coefficient is described in chapter 3.2; as a brief reminder, the correlation coefficient captures the amount of periodic similarity between the strains of two cycles, and is defined as the following, where a r value approaching 1 indicates a greater degree of similarity, A_{mn} and B_{mn} are the data sets of cycle 1 and 50 respectively, and $\overline{A}$ and $\overline{B}$ are the means of their respective data sets:

$$r = \frac{\sum_m \sum_n (A_{mn} - \overline{A})(B_{mn} - \overline{B})}{\sqrt{\left(\sum_m \sum_n (A_{mn} - \overline{A})^2\right)\left(\sum_m \sum_n (B_{mn} - \overline{B})^2\right)}}$$

As evidenced by the calculated correlation coefficients, the strain accommodated by the stress-induced (primarily) martensite exhibited significantly greater cycle-to-cycle similarity in the unfavorably oriented (TD) specimen than in the RD and 45° specimens. Additionally, the (primarily) martensite consistently showed a significantly stronger cycle-to-cycle similarity than the (primarily) austenite, regardless of specimen texture. Recall that the local strain values (encompassing numerous grains) inside the martensite band of the TD specimen were found to be significantly less than in the RD and 45° specimens. The strong cycle-to-cycle strain similarity and the smaller strains contained within the (primarily) martensite bands of the TD

specimen could be due to preferentially oriented microscale pockets of austenite transforming to martensite prior to band nucleation. These microscale pockets of transformed martensite, in a sea of heavily constrained grains, could then lead to a stronger cycle-to-cycle similarity in the strain accommodated by the martensitic transformation. This hypothesis and its relation to the variation in Schmid factors will be scrutinized in our current efforts to characterize martensitic transformation at the length scale of the microstructure.

Table 4-4 Correlation coefficients of the strain similarity between cycles 1 and 50, at each texture, and globally applied strain rate $\dot{\varepsilon}_g$, indicating greater periodical similarity as it approaches 1. Cycle-to-cycle strain similarity is greater for martensite than austenite at all textures and applied strain rates, and appears to increase with unfavorable texture.

Strain Rate	Texture	Austenite Correlation coefficient	Martensite Correlation coefficient
$\dot{\varepsilon}_g=10^{-4}\ s^{-1}$	RD	0.59	0.82
	45°	0.66	0.79
	TD	0.54	0.91
$\dot{\varepsilon}_g=10^{-3}\ s^{-1}$	RD	0.55	0.83
	45°	0.58	0.83
	TD	0.63	0.85
$\dot{\varepsilon}_g=10^{-2}\ s^{-1}$	RD	0.38	0.80
	45°	0.20	0.86
	TD	0.65	0.95

4.4 Evolution of Strain Similarity

The evolution of cycle-to-cycle similarity was investigated by comparing correlation coefficients between line strains at each set reference cycle and cycle of interest, such as cycle 1-2, 1-5, 1-10, 1-25 and 1-50 (reference cycle is 1), and cycle 2-5, 2-10, 2-25, 2-50 (reference cycle

is 2), etc. The selection of the specific images that are used to extract the line strains significantly affects the result of the cycle-to-cycle similarity due to the amount of plastic deformation at different points after full (macroscopic) martensitic transformation. Therefore, images immediately prior to transformation (specimen is macroscopically austenite) and immediately after transformation (specimen is macroscopically martensite) were consistently selected by applying a 0.1% offset from linearity. It was hypothesized that a greater amount of accumulated plastic deformation following the phase transformation would increase the cycle-to-cycle similarity. Images of increasingly strained specimens post-transformation were selected to examine this hypothesis, including a 0.1% offset, +0.2% offset, and +0.4% offset from martensite linearity. The evolution of the cycle-to-cycle similarity of the TD specimen at an applied strain rate of $\dot{\varepsilon}_g = 10^{-4}\ s^{-1}$ is shown in figure 4-11 for these three points of increasing plasticity.

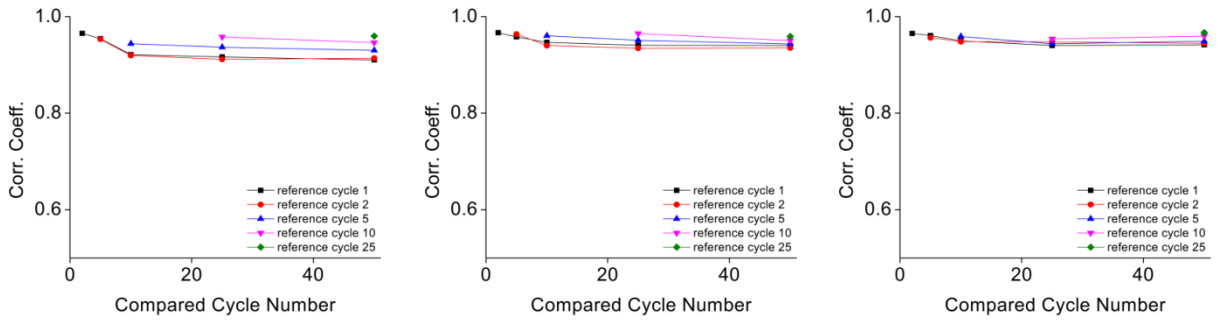

(a) (b) (c)

Figure 4-11 Correlation coefficients between a reference cycle and other compared cycles using, (a) 0.1% offset strain, (b) 0.1% offset strain + 0.2% strain, and (c) 0.1% offset strain + 0.4% strain, of the TD specimen at applied strain rate of $\dot{\varepsilon}_g = 10^{-4}\ s^{-1}$. For example, in each figure, the correlation coefficient between reference cycle 1 and other compared cycles is black line with square (cycle 1-2, 1-5, 1-10, 1-25, and 1-50).

At a set reference cycle, as the compared cycle number increases (for example, cycle 1-2, 1-5, 1-10, 1-25, and 1-50), the correlation coefficient tends to decrease regardless of offset strain. One can see this by following lines (e.g. the black line for reference cycle 1) horizontally across the graph. It is reasonable to expect that the similarity in accommodated axial strain (comparing centerline profiles) would be greater between cycles 1-2 than it would between cycles 1-50. That is, we would expect similarity to the 1st cycle to degrade slightly after 50 cycles; however, it is interesting to note that it does not degrade significantly, and it stabilizes by nominally 25 cycles. Another way to look at this is that at a set compared cycle number, as the reference cycle number increases (for example, cycles 1-25, 2-25, 5-25, and 10-25), the correlation coefficient increases. This is particularly when the offset strain is low (0.1%, Figure 4-11a). One can see this by following points upwards at a set compared cycle number (x-axis value). For example, the strain similarity is greater between cycles 10-25 than between cycles 1-25, indicating that similarity 'mechanisms' (dislocation networks, retention of martensitic nuclei) continue to accumulate with cycling, although at a reduced rate.

In order to examine the effect of the amount of plastic deformation following phase transformation on cycle-to-cycle similarity, correlation coefficients between cycles are calculated for three image sets with an increasing amount of post-transformation plasticity. As shown in the inset of the macroscopic stress-strain curve in figure 4-12(a), images "A", "B", and "C" are taken at increasing levels of post-transformation plasticity. The analysis in figure 4-12 is shown for a TD specimen at an applied strain rate of $\dot{\varepsilon}_g = 10^{-4}$ s^{-1}. As the data is selected from increasingly strained images (A to C), higher correlation coefficients are observed because of the (diminishing) accumulation of plastic deformation after completion of the stress plateau

(macroscopic phase transformation). As the reference cycle number increases (figure 4-12a to 4-12e), the correlation coefficients between image sets at different strains become close and finally, nominally the same (figure 4-12e). These results are consistently observed for specimens of all three crystallographic textures. The RD and 45° specimens show lower correlation coefficient values than the TD specimen, but these correlation coefficients also become nominally the same in the most strained images (C). This indicates that dislocation networks and the amount of plastically deformed martensite saturate with cycling, in this case near cycle 50 (see figure 4-12e) regardless of crystallographic orientation.

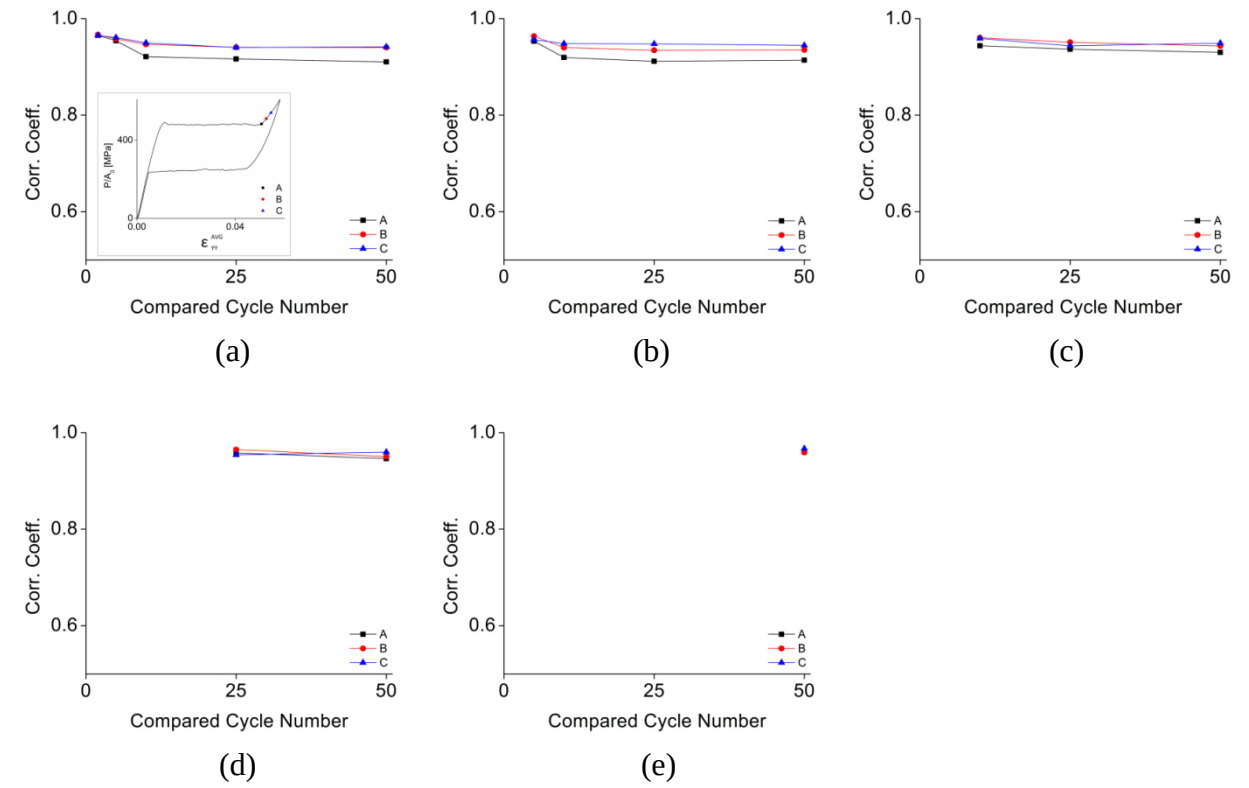

Figure 4-12 Correlation coefficients (a) between a reference cycle 1 and other cycles (cycle 1-2, 1-5, 1-10, 1-25, and 1-50), (b) between a reference cycle 2 and other cycles (cycle 2-5, 2-10, 2-25, and 2-50), (c) between a reference cycle 5 and other cycles (cycle 5-10, 5-25, and 5-50), (d) between a reference cycle 10 and other cycles (cycle 10-25 and 1-50), (e) between a reference cycle 25 and 50 (cycle 25-50) at different sets of images, A, B and C (A: 0.1% offset strain, B: 0.1% offset strain + 0.2% strain, and C: 0.1% offset strain + 0.4% strain), of the TD specimen at applied strain rate of $\dot{\varepsilon}_g = 10^{-4}\ s^{-1}$.

The accumulated latent heat under faster applied strain rates affects the evolution of cycle-to-cycle similarity in the (macroscopically) martensite phase. In order to examine this effect, a highly strained image ("C") was selected with enough cycles to result in a significant accumulation of plastic martensite (reference cycle 5). Correlation coefficients between reference cycle 5 and other compared cycles at the globally applied strain rate of $\dot{\varepsilon}_g = 10^{-4}$, 10^{-3} and 10^{-2} s^{-1} are shown in figure 4-13. All have high correlation coefficient values, (> 0.87) and indicate a strong cycle-to-cycle similarity, but more similarity is observed at $\dot{\varepsilon}_g = 10^{-2}$ s^{-1} regardless of the crystallographic texture of the specimen. It is hypothesized that the large amount of accumulated latent heat (more than 50°C) at a strain rate of $\dot{\varepsilon}_g = 10^{-2}$ s^{-1} increases the relative amount of slip and results in stronger cycle-to-cycle similarity, in a similar manner to higher residual strain accumulation at faster strain rates and higher temperatures.

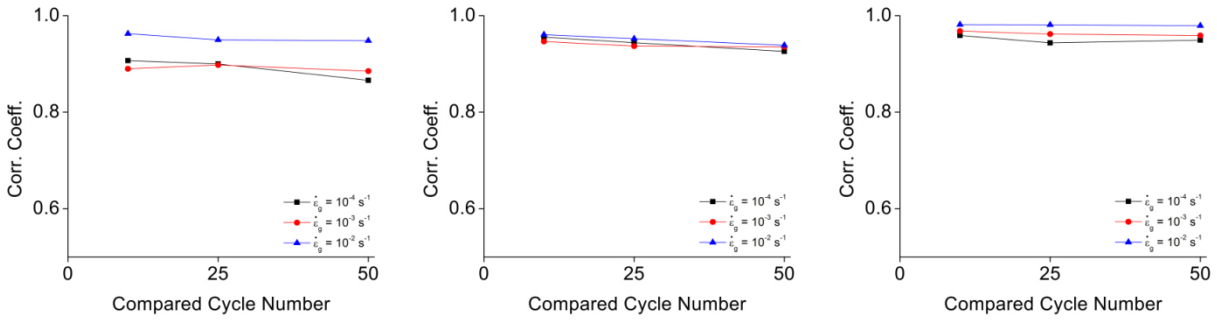

(a) (b) (c)

Figure 4-13 Correlation coefficient between reference cycle 5 and others (e.g. cycle 5-10, 5-25, and 5-50) at applied strain rates of $\dot{\varepsilon}_g = 10^{-4}$, 10^{-3} and 10^{-2} s^{-1} at the crystallographic textured specimen (a) RD, (b) 45°, and (c) TD. The higher applied strain rate shows stronger cycle-to-cycle similarity due to easier dislocation movement at higher temperature.

4.4. CONCLUSIONS

Full-field methods were used to explore the effects of crystallographic texture on the formation of stress-induced martensite during the cyclic loading of Nitinol. Three texture orientations from a cold-rolled 254μm thick sheet (RD, 45°, TD) were examined under displacement-controlled cycling at globally applied strain rates of $\dot{\varepsilon}_g = 10^{-4}, 10^{-3}$, and $10^{-2} s^{-1}$.

- The RD and 45° test specimens were found to have crystallographic textures that were favorably oriented for large transformation strains, and the TD specimen had a crystallographic texture that was relatively unfavorably oriented for transformation.
- The observed propensity of the TD specimen to nucleate more martensitic deformation bands than the RD or 45° specimens arises from the difference between the nucleation and propagation stresses. At a set strain rate, the TD specimen exhibited significantly higher nucleation (σ_N) and propagation (σ_P) stresses than the RD and 45° specimens. However, the difference between these stresses ($\sigma_N - \sigma_P$) was substantially smaller. Thus, the TD specimen was more inclined to nucleate a new deformation band in a cooler location, rather than propagate an existing deformation band in a location that had accumulated latent heat.
- During stress-induced martensitic transformation, the TD specimen accommodated more average axial strain outside the (primarily martensite) deformation band, and less axial strain inside the band, compared to the more favorably orientated RD and 45° specimens. Otherwise stated, in the TD specimen, a ‘less strained’ deformation band propagated through a ‘more strained’ matrix during loading.
- The pixel strain distribution (each pixel encompassing hundreds of grains and containing contributions from both martensite and austenite), once the deformation band had fully

propagated through the specimen, was remarkably similar from cycle to cycle. The (primarily) martensite region consistently showed a stronger cycle-to-cycle strain similarity than the (primarily) austenite region for all three globally applied strain rates and crystallographic textures.

- Additionally, the strain similarity in the (primarily) martensite region evolved with cycling for all specimens and applied strain rates. For example, the similarity between cycles 25 and 50 was larger than the similarity between cycles 1 and 50. This indicates that the dislocation networks and retention of martensitic nuclei continued to evolve, although to a reduced extent, as cycling progressed.
- The cycle-to-cycle strain similarity was stronger in the TD specimen than in the RD and 45° specimens. The strong cycle-to-cycle strain similarity and the relatively smaller strains contained within the (primarily martensite) deformation bands of the TD specimen could be due to preferentially oriented microscale pockets of austenite transforming to martensite prior to band nucleation. These microscale pockets of transformed martensite, in a sea of heavily constrained grains, could then lead to a stronger cycle-to-cycle similarity in the strain accommodated by the martensitic transformation. This hypothesis and its relation to the variation in Schmid factors will be scrutinized in our current efforts to characterize martensitic transformation at the length scale of the microstructure.
- In order to examine the effect of the amount of plastic deformation following phase transformation on cycle-to-cycle similarity, correlation coefficients between cycles were calculated for three image sets with an increasing amount of post-transformation plasticity. As the data was selected from increasingly strained images (A to C), higher correlation coefficients were observed because of the (diminishing) accumulation of plastic deformation

after completion of the stress plateau (macroscopic phase transformation). These results were consistently observed for specimens of all three crystallographic textures.

- The accumulated latent heat under faster applied strain rates affects the evolution of cycle-to-cycle similarity in the (macroscopically) martensite phase. It is hypothesized that the large amount of accumulated latent heat (more than 50°C) at faster strain rates increases the relative amount of slip and results in stronger cycle-to-cycle similarity, in a similar manner to higher residual strain accumulation.

REFERENCES

[1] S. Miyazaki, V. H. No, K. Kitamura, A. Khantachawana, and H. Hosoda, “Texture of Ti–Ni rolled thin plates and sputter-deposited thin films,” *International Journal of Plasticity*, vol. 16, no. 10–11, pp. 1135–1154, 2000.

[2] H. Inoue, N. Miwa, and N. Inakazu, “Texture and shape memory strain in TiNi alloy sheets,” *Acta Materialia*, vol. 44, no. 12, pp. 4825–4834, Dec. 1996.

[3] S. H. Chang and S. K. Wu, “Textures in cold-rolled and annealed Ti50Ni50 shape memory alloy,” *Scripta Materialia*, vol. 50, no. 7, pp. 937–941, Apr. 2004.

[4] S. W. Robertson, V. Imbeni, H. R. Wenk, and R. O. Ritchie, “Crystallographic texture for tube and plate of the superelastic/shape-memory alloy Nitinol used for endovascular stents,” *Journal of Biomedical Materials Research Part A*, vol. 72A, no. 2, pp. 190–199, 2005.

[5] J. A. Shaw and S. Kyriakides, “On the nucleation and propagation of phase transformation fronts in a NiTi alloy,” *Acta Materialia*, vol. 45, no. 2, pp. 683–700, Feb. 1997.

[6] S. Daly, G. Ravichandran, and K. Bhattacharya, “Stress-induced martensitic phase transformation in thin sheets of Nitinol,” *Acta Materialia*, vol. 55, no. 10, pp. 3593–3600, Jun. 2007.

[7] J. H. Mulder, P. E. Thoma, and J. Beyer, “Anisotropy of the shape memory effect in tension of cold-rolled 50.8 Ti 49.2 Ni (at.%) sheet,” *Z Metallkd*, vol. 84, pp. 501-508, 1993.

[8] L. C. Brinson, I. Schmidt, and R. Lammering, “Stress-induced transformation behavior of a polycrystalline NiTi shape memory alloy: micro and macromechanical investigations via in situ optical microscopy,” *Journal of the Mechanics and Physics of Solids*, vol. 52, no. 7, pp. 1549–1571, Jul. 2004.

[9] M. Kimiecik, J. W. Jones, and S. Daly, “Quantitative studies of microstructural phase transformation in Nickel–Titanium,” *Materials Letters*, vol. 95, pp. 25–29, Mar. 2013.

[10] K. Kim and S. Daly, “Martensite strain memory in the shape memory alloy Nickel-Titanium under mechanical cycling,” *Exp Mech*, vol. 51, no. 4, pp. 641–652, Apr. 2011.

Chapter 5

The Effect of Cycling and Strain Rate on the Pseudoelastic Deformation of Nickel-Titanium

In this chapter, the effect of applied strain rate and displacement-controlled cycling are examined through full-field strain and thermal mapping by three-dimensional Digital Image Correlation (3D-DIC) and infrared thermography, respectively. Transformation characteristics including the released (absorbed) latent heat during loading (unloading) and the relationship between transformation stresses and temperature were analyzed at strain rates of $\dot{\varepsilon}_g = 10^{-2}$, 10^{-3} and $10^{-4} s^{-1}$ during displacement-controlled loading to 50 cycles. Additionally, testing with holds between cycles (to remove accumulated absorbed latent heat from the previous cycle) was performed at an applied strain rate of $\dot{\varepsilon}_g = 10^{-2}\ s^{-1}$ and differences between these "with-hold" tests and "without hold" tests are discussed. The evolution of martensitic volume fraction and the velocities of the martensitic bands and small offshoot branches are examined.

5.1. Effect of Applied Strain Rate on Deformation and Thermal Response

The macroscopic stress-strain curve of the as-received Nitinol and corresponding images of the strain and temperature fields in the gage section are shown in figure 5-1 through 5-3 at

applied strain rates of $\dot{\varepsilon}_g = 10^{-4}\ s^{-1}$, $\dot{\varepsilon}_g = 10^{-3}\ s^{-1}$, and $\dot{\varepsilon}_g = 10^{-2}\ s^{-1}$ respectively. Strain values in the macroscopic curve (ε_{YY}^{AVG}) were calculated by averaging approximately 600,000 strain values in the gage section. In figure 5-1 at an applied strain rate of $\dot{\varepsilon}_g = 10^{-4}\ s^{-1}$, the behavior was as follows: at $\varepsilon_{YY}^{AVG} < 0.0076$, the austenite phase was elastically loaded until the stress reached a nucleation stress for A->M phase transformation of σ_{NM} = 445 MPa, at which point a large localized band of martensite nucleated. The stress-induced martensitic band then propagated at a lower stress than the nucleation value (σ_{PM} = 413 MPa). The martensitic band was easily visible through DIC imaging, due to the large difference in the localized strain between the austenite and martensite phases.

Determining the start and finish points of transformation can be difficult, since as discussed earlier in this thesis, there is likely microscopic martensite in a 'fully austenitic' sample and vice versa. In order to consistently determine the start and finish points of the phase transformation while taking microscopic marensite (austenite) accumulation into consideration prior to A->M (M->A) transformation, a 0.1% linear off-set method was adopted to define four points, denoted as the martensite start, martensite finish, austenite start, and austenite finish. These points are shown as points 1, 6, 7, and 12, respectively in figure 5-1(a) and the procedure to determine them is shown in chapter 4, figure 4-6. Six pairs of DIC strain fields and IR thermal fields taken from the transformation plateau are shown and numbered from ① to ⑥ in figure 5-1(b). Similarly, six pairs of images, from ⑦ to ⑫ in figure 5-1(b) show reverse phase transformation. In the microscopic view, we again note that A → M transformation occurs on the

microscopic level prior to the nucleation of large martensitic bands. Thus, we consider the elastic region of the austenite phase as 'macroscopically' austenite and similarly, the elastic region of the martensite phase as 'macroscopically martensite,' as a reminder that it is likely not fully saturated. A study by Brinson et al. [1] found that approximately 30 - 40% of a specimen remained austenite even when the stress-induced martensitic phase transformation was considered macroscopically complete.

Figures 5-2 and 5-3 shown strain and thermal fields, respectively, from tests performed at globally applied strain rates of $\dot{\varepsilon}_g = 10^{-3}$, and 10^{-2} s^{-1}. Note that stress-induced martensitic phase transformation appears incomplete at the end of loading in the first cycle at a strain rate of $\dot{\varepsilon}_g = 10^{-3}$ s^{-1}, as evident in the stress-strain curve in Fig. 5-2 (a). However, the completion of martensitic band propagation was verified by DIC-obtained strain field images. At the relatively slow strain rate of $\dot{\varepsilon}_g = 10^{-4}$ s^{-1} (figure 5-1(a)), only one primary martensitic band nucleated and propagated, and the transformation plateau was nominally flat. As the strain rate increased, more martensitic bands nucleated and the transformation plateau became increasingly inclined, as shown in figures 5-2 and 5-3. At a strain rate of $\dot{\varepsilon}_g = 10^{-3}$ s^{-1}, two martensitic bands nucleated and propagated during phase transformation as shown in figure 5-2(b), and the phase transformation plateau in figure 5-2(a) is inclined with a slope of approximately 1136 MPa. At an applied strain rate of $\dot{\varepsilon}_g = 10^{-2}$ s^{-1}, approximately five martensitic bands nucleate, and the phase transformation plateau is further inclined with the slope of approximately 3204 MPa as seen in figure 5-3. The inclination of the stress plateau during transformation is directly related to the temperature of the specimen. The difference of the maximum and minimum local

temperatures in the specimen during the first cycle is 4.3 °C ($\dot{\varepsilon}_g = 10^{-4}\ s^{-1}$), 19.9 °C ($\dot{\varepsilon}_g = 10^{-3}\ s^{-1}$), and >39.5 °C ($\dot{\varepsilon}_g = 10^{-2}\ s^{-1}$). Note that the maximum local temperature in the first cycle at $\dot{\varepsilon}_g = 10^{-2}\ s^{-1}$ is >50 °C, but the exact value was unable to be measured due to a 50°C maximum resolution limit on the infrared camera. The high temperature gradients at fast strain rates, caused by the accumulation of the latent heat during martensitic phase transformation, results in an increase in the transformation stress and an increase in the stress required for the nucleation of the martensitic band (σ_{NM}). Observation of the full-field strain maps at each globally applied strain rate, from figures 5-1(b), 5-2(b), and 5-3(b), shows increasing homogenization of the strain across the specimen surface. Additionally, the temperature maps show higher local and global temperatures with an increase in applied strain rate. It is known that at faster strain rates, these temperature gradients cause a preference for the nucleation of new martensite bands at a cooler location away from a propagating band that has accumulated latent heat. An increased nucleation of martensitic bands with higher strain rates is expected given the known interaction between latent heat and band nucleation [2].

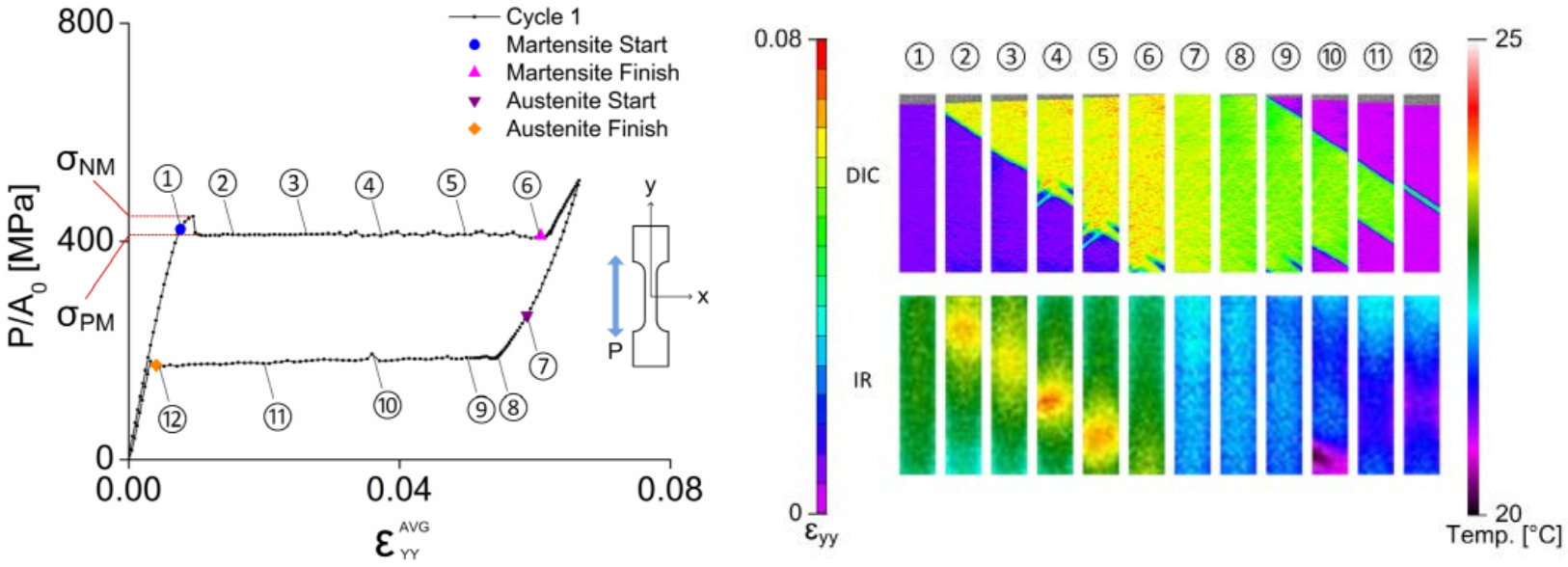

Figure 5-1 (a) Macroscopic stress-strain curve of cycle 1 a globally applied strain rate of $\dot{\varepsilon}_g = 10^{-4}\ s^{-1}$ and crystallographic texture in the rolling direction of the sheet. (b) DIC and IR images show full-field and quantitative maps of the strain and temperature in the gage section of the sample during phase transformation, corresponding with numbers (from ① to ⑫) on the stress-strain curve, in the first cycle. At a slow strain rate, only one large martensitic band nucleates and propagates, with small martensitic branches offshoots that cause small fluctuations in the stress-strain curve.

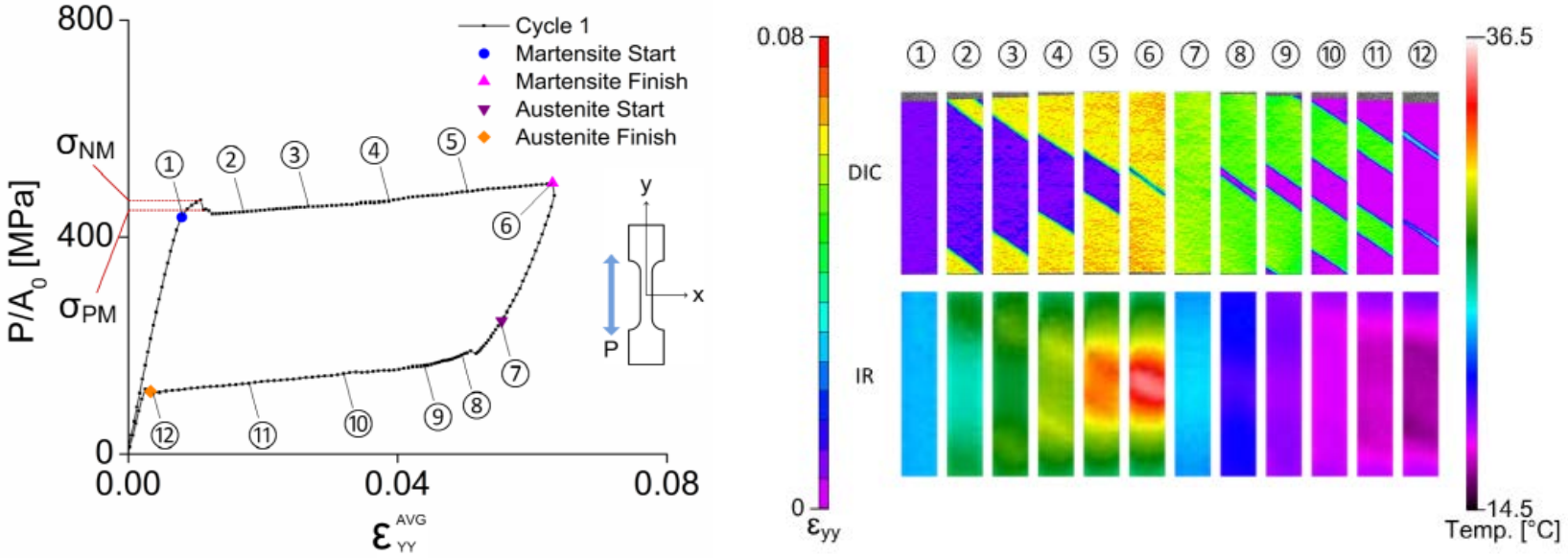

(a) (b)

Figure 5-2 (a) Macroscopic stress-strain curve of cycle 1 at a globally applied strain rate of $\dot{\varepsilon}_g = 10^{-3}\ s^{-1}$ and crystallographic texture in the rolling direction of the sheet. (b) DIC and IR images show full-field and quantitative maps of the strain and temperature in the gage section of the sample during phase transformation, correspond with numbers (from ① to ⑫) on the stress-strain curve. Two martensitic bands nucleate and propagate. The accumulation of latent heat results in an inclined stress plateau in the stress-strain curve.

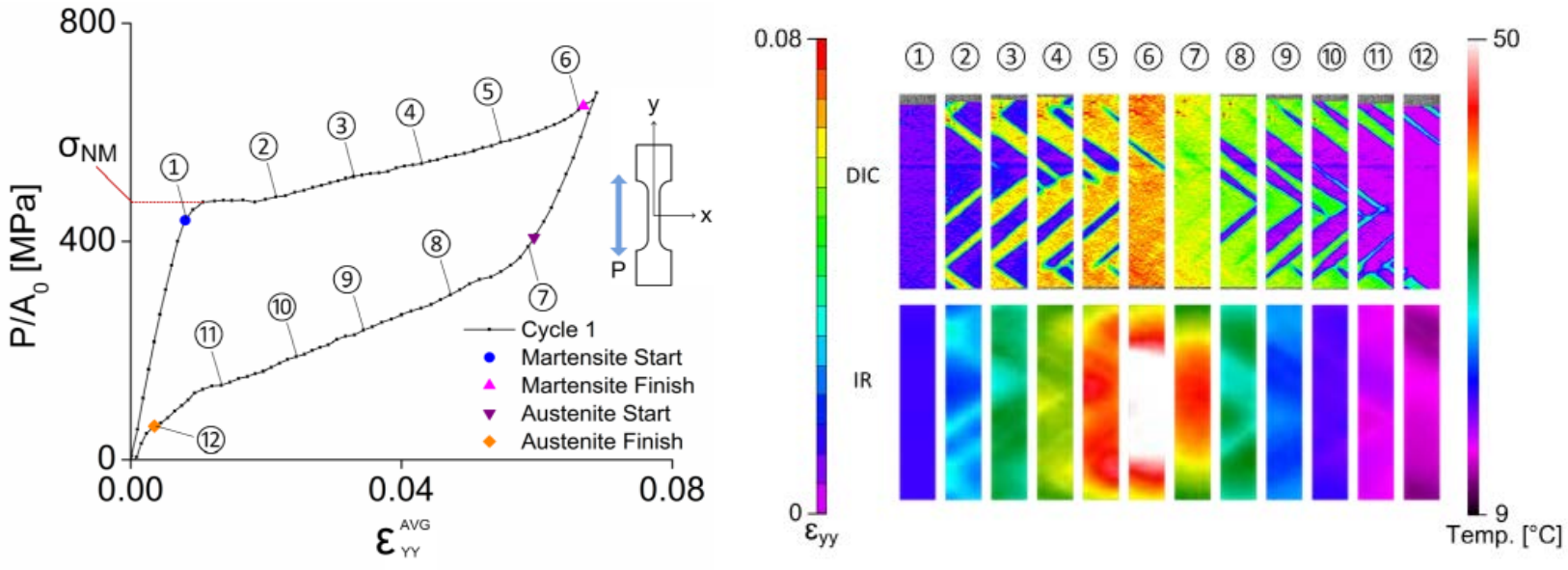

(a) (b)

Figure 5-3 (a) Macroscopic stress-strain curve of cycle 1 at a globally applied strain rate of $\dot{\varepsilon}_g = 10^{-2}\ s^{-1}$ and crystallographic texture in the rolling direction of the sheet. (b) DIC and IR images show full-field quantitative maps of the strain and temperature in the gage section of the sample during phase transformation, corresponding with numbers ① to ⑫ on the stress-strain curve. More than four martensitic bands nucleate and propagate. Higher accumulation of latent heat results in an inclined stress plateau in the stress-strain curve.

5.2. Effect of Cycling and Strain Rate

The combined effects of applied strain rate and cycling are shown for $\dot{\varepsilon}_g = 10^{-4}\ s^{-1}$, $10^{-3}\ s^{-1}$ and $10^{-2}\ s^{-1}$ in figures 5-4 (a) through (c). Comparison between figures 5-4(a) through (c) shows the effect of strain rate, and each plot individually shows the effect of cycling at a set strain rate. At each strain rate, the stress required to nucleate and propagate martensitic bands decreases and the amount of residual strain increases with cycling. However, the rate of decrease in the nucleation/propagation stresses and the rate of increase of residual strain become smaller with cycling. These cycling effects agree with many previous cyclic studies [1, 3-9]. The shape of stress-strain curves becomes smoother with cycling as a result of more spatial homogeneity in phase transformation evident through DIC imaging. These cycling effects are particularly pronounced at an applied strain rate of $\dot{\varepsilon}_g = 10^{-2}\ s^{-1}$, which will be discussed in the chapter.

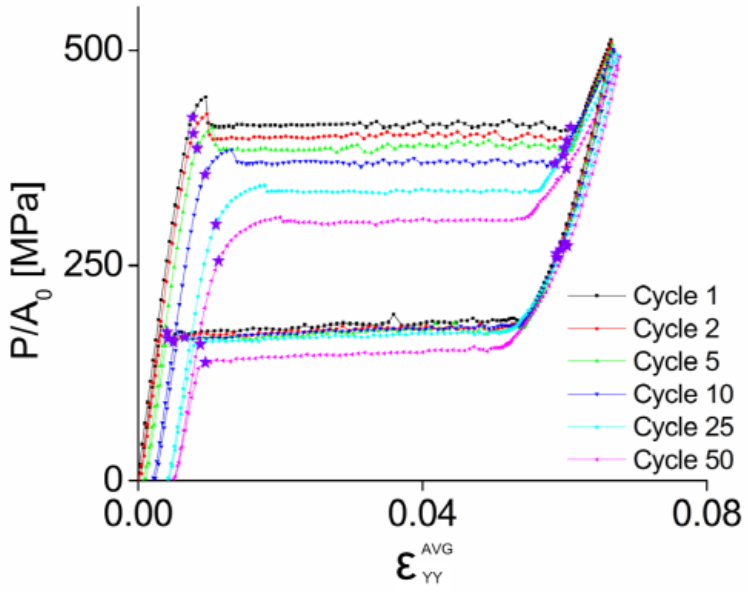

(a)

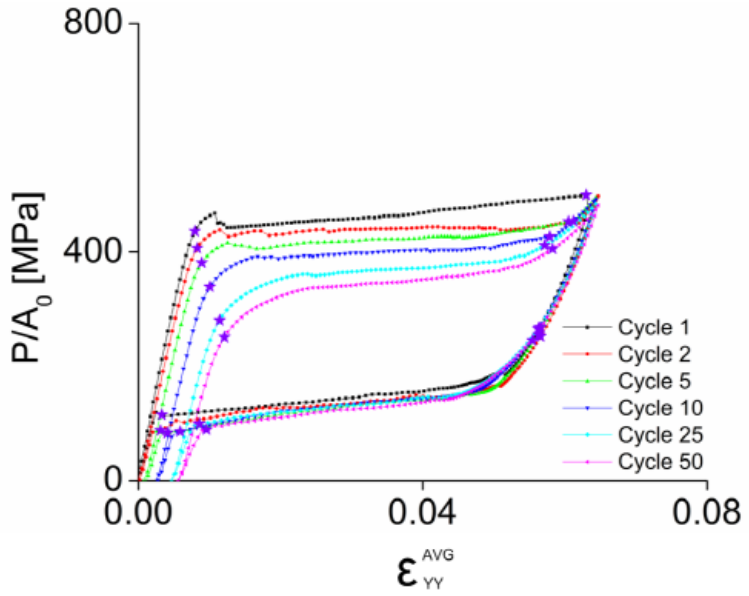

(b)

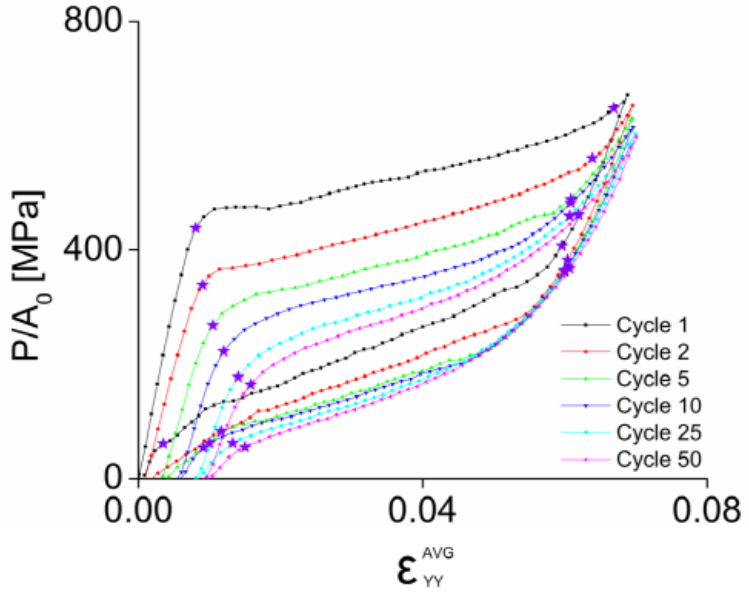

(c)

Figure 5-4 Macroscopic stress-strain curve of cycles 1, 2, 5, 10, 25, and 50 at a globally applied strain rate of (a) $\dot{\varepsilon}_g = 10^{-4}\ s^{-1}$, (b) $\dot{\varepsilon}_g = 10^{-3}\ s^{-1}$ and (c) $\dot{\varepsilon}_g = 10^{-2}\ s^{-1}$. Crystallographic texture is in the rolling direction of the sheet and phase transformation start and finish points, shown as purple stars, are defined through a 0.1% offset from linearity.

The elastic modulus of the austenite and martensite phases at $\dot{\varepsilon}_g = 10^{-4}\ s^{-1}$ and varied cycle number (*N)* are tabulated in Table 1. These are calculated by linear fits to the austenite and martensite loading portions of the macroscopic response. The elastic moduli of both the austenite and martensite phases decrease as cycling increases, both during loading and unloading. Liu [10] observed a similar value of the austenite elastic modulus in the first loading cycle and a similar amount of decrease in the austenite elastic modulus after ten cycles. Mao et al. [11] attributed this softening of austenite elastic modulus to grain reorientation and development of defects/dislocations during mechanical cycling. This decrease in the austenite elastic modulus could also be enhanced by increased pockets of residual martensite that form with cycling. The martensitic elastic modulus also decreases with cycling, also likely due to the development of defects and dislocations. However, note that in the 50^{th} cycle the elastic modulus of the martensite phase increases slightly from cycle 25, by approximately 1 MPa; here, the phase transformation plateau is shortened and more plasticity is accumulated in martensite under the displacement-controlled test.

Table 5-1 The elastic modulus of austenite and marteniste during loading and unloading at a globally applied strain rate of $\dot{\varepsilon}_g = 10^{-4}\ s^{-1}$ and crystallographic texture in the rolling direction of the sheet.

	Austenite Loading [GPa]	Martensite Loading [GPa]	Martensite Unloading [GPa]	Austenite Unloading [GPa]
Cycle 1	60.45	21.56	30.58	57.69
Cycle 2	58.25	21.75	30.70	58.83
Cycle 5	57.94	20.25	30.21	56.35
Cycle 10	55.70	17.53	28.94	54.62
Cycle 25	52.41	16.61	26.94	47.66
Cycle 50	49.83	17.97	27.62	43.23

The stress required to nucleate localized martensitic band(s), the amount of hysteresis, and the accumulation of residual strain were examined in the context of the effect of cycling and strain rate on the macroscopic stress-strain response. As seen in figure 5-4, the residual strain (ε^P) accumulates as cycling progresses. It is hypothesized that dislocation hardening with cycling results in a rise in stress required for slip, while at the same time the stress required for phase transformation decreases with cycling [3, 4]. Thus, the transformation stress becomes increasingly dominant, resulting in the increment of accumulated residual strain decreasing with cycling. Secondly, the amount of residual strain accumulation (ε^P) increases as the applied strain rate increases. The greater global and local temperature increases caused by a faster applied strain rate causes an increase in the stress required for transformation. However, the resolved shear stress for slip decreases as temperature increases due to the thermal activation of dislocation motion. As a result, the difference between stresses required for slip and transformation becomes lower as the strain rate increases [3, 4]. Consequently, cycling or decreasing the strain rate, as seen in figure 5-5, causes a decrease in the amount of residual strain. In figure 5-5, the increment in accumulation of the residual strain at a set strain rate decreases with cycling, and a large amount of residual strain is evident as the strain rate is increased.

One of the advantages of this experimental approach is that the nucleation stress of the first martensitic band can be accurately obtained within ±15 MPa (due to discrete image) through full-field strain mapping. By using this method, the critical stresses and strains (globally averaged across the image) for the nucleation of the first martensitic band are tabulated in Table 5-2 for all applied strain rates and cycles. Note that the nucleation stress could not be determined at select points, due to the inherently fuzzy and criss-cross character of the martensitic bands under certain loading conditions that combine high cycle number and fast strain rates; these are

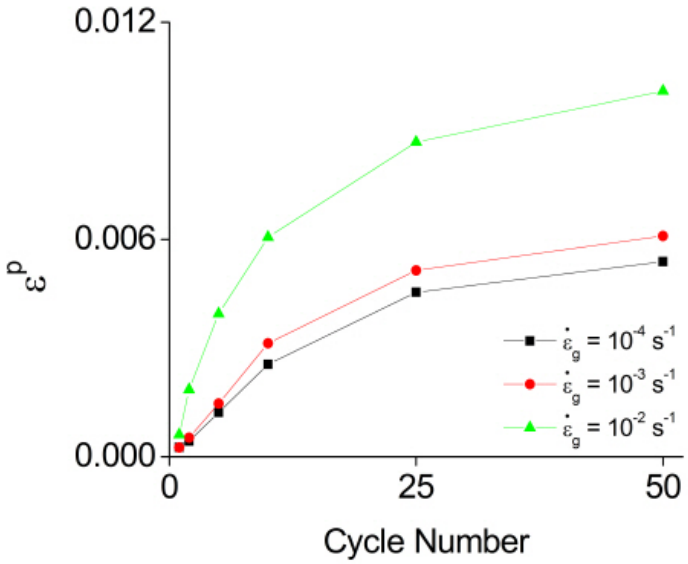

Figure 5-5 Accumulation of a residual strain at $\dot{\varepsilon}_g = 10^{-4}\ s^{-1}$, $10^{-3}\ s^{-1}$ and $10^{-2}\ s^{-1}$ for a specimen with crystallographic texture in the rolling direction of the sheet. At a set applied strain rate, the increment of the residual strain decreases with cycling. Residual strain accumulates more quickly at faster strain rates.

Table 5-2 The strain and stress required for nucleation of the localized martensitic bands during loading at various strain rates and cycling, determined from full-field strain mapping. Note the particularly large drop in nucleation stress at a strain rate of 10^{-2}, due to decreased specimen temperature by absorbed latent heat from cycle 1.

Strain Rate	$10^{-4}\ s^{-1}$		$10^{-3}\ s^{-1}$		$10^{-2}\ s^{-1}$	
Cycle	ε_{YY}^{AVG} [%]	σ_{NM} [MPa]	ε_{YY}^{AVG} [%]	σ_{NM} [MPa]	ε_{YY}^{AVG} [%]	σ_{NM} [MPa]
1	1.07	415	1.17	450	1.19	474
2	1.07	402	1.20	427	1.24	368
5	1.15	390	1.29	412	N/A	N/A
10	1.40	370	1.69	390	N/A	N/A
25	1.86	336	N/A	N/A	N/A	N/A
50	2.06	300	N/A	N/A	N/A	N/A

denoted as N/A. At a set strain rate, the nucleation stress decreases with cycling as observed and explained in the macroscopic stress-strain data. As the strain rate increases, the stress required for nucleation of the martensitic band increases. Though many values cannot be measured at global strain rate of $\dot{\varepsilon}_g = 10^{-2}\ s^{-1}$ due to strain homogenization, the nucleation stress shows a large drop between cycle 1 and 2. It is hypothesized that this large drop is caused by decreased specimen temperature at beginning of cycle 2 due to absorbed latent heat in unloading process of cycle 1. This latent effect from previous cycle is examined in detail in chapter 5.3.

A high damping capacity, characterized by the amount of hysteresis in the macroscopic response, is used in seismic protection and vibration isolation applications of Nitinol [12-15]. In order to examine the damping capacity, the energy is calculated as the area under the stress-strain curve during loading and unloading. Energy is dissipated when the specimen is loaded and absorbed when the specimen is unloaded. The amount of dissipated (loading) and absorbed (unloading) energy is shown in figure 5-6(a) and (b), respectively. The hysteresis is obtained as the difference of the dissipated and absorbed energies, and is shown in figure 6(c). Note that the amount of energy is calculated from the stress-strain curves and is affected by the maximum deformation (strain). Note that due to a limited number of samples and a strong dependence of the length of the stress plateau on applied strain rate and crystallographic texture, it was difficult to know apriori the displacement limit to set in order to obtain optimal transformation, i.e. transformation completion without unwanted plasticity. Although it was confirmed that the martensite band(s) propagated fully through the gage section by the full-field DIC images, please note that the maximum strain at $\dot{\varepsilon}_g = 10^{-3}\ s^{-1}$ was smaller than that at other strain rates by a significant amount (0.55%), thus the amount of both the dissipated and stored energy could be

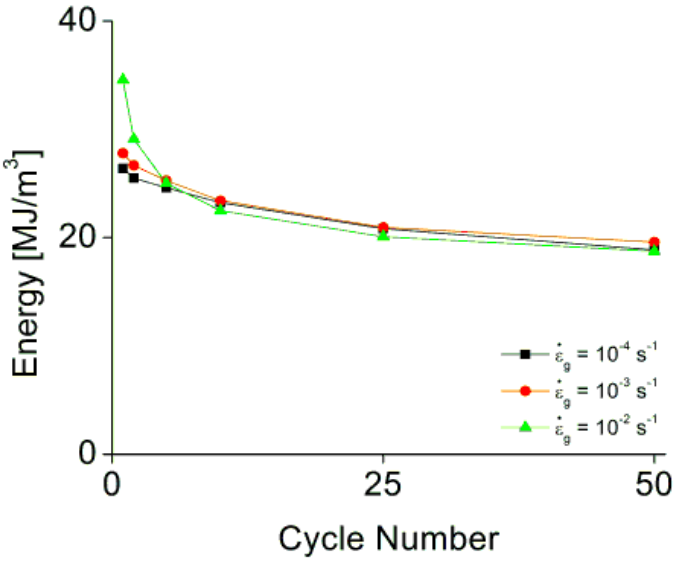
40
20
0
0
25
50
Energy [MJ/m3]
Cycle Number
ε̇g = 10-4 s-1
ε̇g = 10-3 s-1
ε̇g = 10-2 s-1

(a)

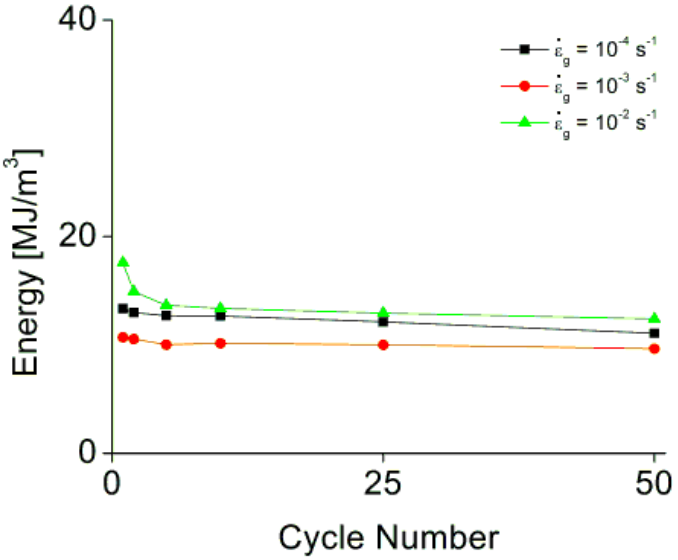
40
20
0
0
25
50
Energy [MJ/m3]
Cycle Number
ε̇g = 10-4 s-1
ε̇g = 10-3 s-1
ε̇g = 10-2 s-1

(b)

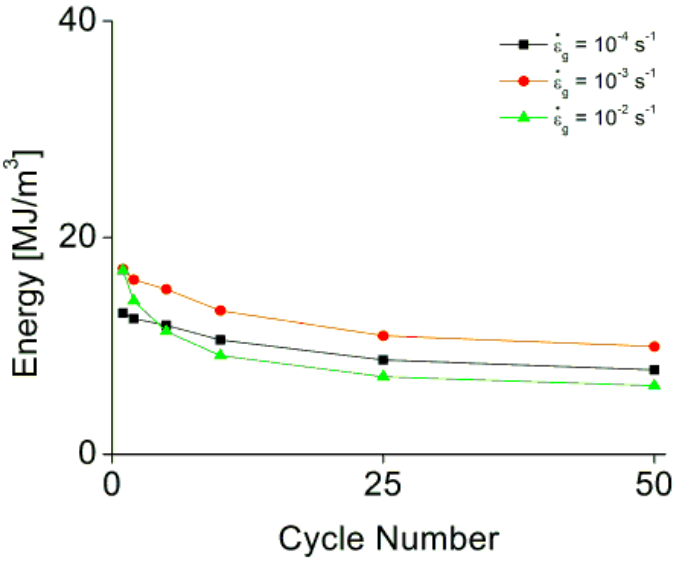

(c)

Figure 5-6 (a) Dissipated energy during loading, (b) absorbed energy during unloading, and (c) stored energy, hysteresis for texture in the rolling direction of the sheet. The energy of (a) and (b) is calculated as the area under the stress-strain curve during loading and unloading, respectively. The hysteresis indicates a damping capacity for use of NiTi in seismic protection and vibration isolation applications.

larger than the amount of energies in figure 5-6 (a) and (b). A significant amount of energy is dissipated at $\dot{\varepsilon}_g = 10^{-2}\ s^{-1}$ in the first cycle, but the amount of dissipated energy at $\dot{\varepsilon}_g = 10^{-2}\ s^{-1}$ drops continuously and crosses below that of $\dot{\varepsilon}_g = 10^{-3}\ s^{-1}$ and $\dot{\varepsilon}_g = 10^{-4}\ s^{-1}$ around the fifth cycle. After the fifth cycle, the amount of dissipated energy at each strain rate is relatively the same, though they all continue to continuously decrease with cycling. The dissipated and absorbed energy at $\dot{\varepsilon}_g = 10^{-2}\ s^{-1}$ substantially drop between cycle 1 and 2.

5.3 Effect of Accumulated Latent Heat between Cycles

Tests were undertaken to examine the effect of a hold time in between cycles on the macroscopic stress-strain behavior. The hold time acted to remove the effect of latent heat accumulation from prior cycles from the observed macroscopic response. A strain rate of $\dot{\varepsilon}_g = 10^{-2}\ s^{-1}$ was chosen for these tests because of the relatively rapid accumulation of latent heat. It was found that the macroscopic stress-strain curves that were obtained from testing without holding in-between cycles generally had a lower stress level than those with holding; if one attributes this difference to temperature alone, and does not consider plasticity, this means that the samples without holding are in fact cooler at the beginning of subsequent cycles (e.g. cycle 2) than those with holding – thus meaning the 'with hold' samples find it easier to dissipate heat instead of absorb heat.

In order to quantify the accumulated absorbed latent heat, the average temperature in the gage section of the specimen was obtained by averaging all temperature values (pixels) of the IR images. Let us first examine the tests with no holding between cycles, as shown in figure 5-7(a) for a relatively fast globally applied strain rate of $\dot{\varepsilon}_g = 10^{-2}\ s^{-1}$, the averaged temperature of the specimen at the start of testing prior to cycle 1 was 18.3 °C. However, the temperature at the end of cycle 1 was 13.0°C, as the applied strain rate was too fast to allow the absorbed latent heat form the M->A transformation to equilibriate with the ambient environment. Because the latent heat cannot equilibriate effectively, the average temperature at the beginning of cycle 2 was then 13.0 °C. This relative decrease in the average specimen temperature at the start of cycle 2 decreases the transformation stress, causing the large drop of stress required for nucleation and the decrease in the amount of dissipated energy observed in figure 5-6(a).

To remove the effect of latent heat on the cycling dependence of the macroscopic stress-strain response, testing at an applied strain rate of $\dot{\varepsilon}_g = 10^{-2}\ s^{-1}$ with a hold time of 1800 seconds between cycles was performed in order to remove the effect of absorbed latent heat from the previous cycle. The averaged temperature of the specimen gage section is plotted with respect to the averaged applied strain in figure 5-7(b). Because the hold time between cycles allowed the latent heat absorbed from the M->A transformation to equilibriate, the start temperature of the specimen gage section was stable at approximately 20.8 °C at the start of every cycle. The corresponding macroscopic stress-strain curve of this 'with-hold' test is shown in figure 5-8. Though a large drop of the transformation stress between cycle 1 and cycle 2 is observed in the macroscopic curves of the without hold test (figure 5-4(c)), there is a relatively small drop of the transformation stress in the with-hold test (figure 5-8). All stress-strain curves (except cycle 1) in the with-hold test show a higher transformation stress than those in the without-hold test.

The dissipated/absorbed energy and hysteresis of the with-hold test as a function of cycling is shown in figure 5-9. The amount of dissipated energy quickly drops until cycle 10, at which point it begins to level out. The amount of dissipated energy at $\dot{\varepsilon}_g = 10^{-2}\ s^{-1}$ stays consistently larger than that at other strain rates ($\dot{\varepsilon}_g = 10^{-3}\ s^{-1}$ and $\dot{\varepsilon}_g = 10^{-4}\ s^{-1}$) regardless of cycle number (recall that this is with-hold; hence the specimen begins at a stable temperature at the start of every cycle, which results in a higher dissipation of energy as it does not have the advantage of starting from a cooler state). Though the amount of stored energy at each strain rate cannot be compared due to different maximum deformation as explained earlier, the tendency of stored energy with cycling is nominally similar regardless of the strain rate. Compared to the without-hold test, the amount of both dissipated and stored energy in with-hold test is larger, thus

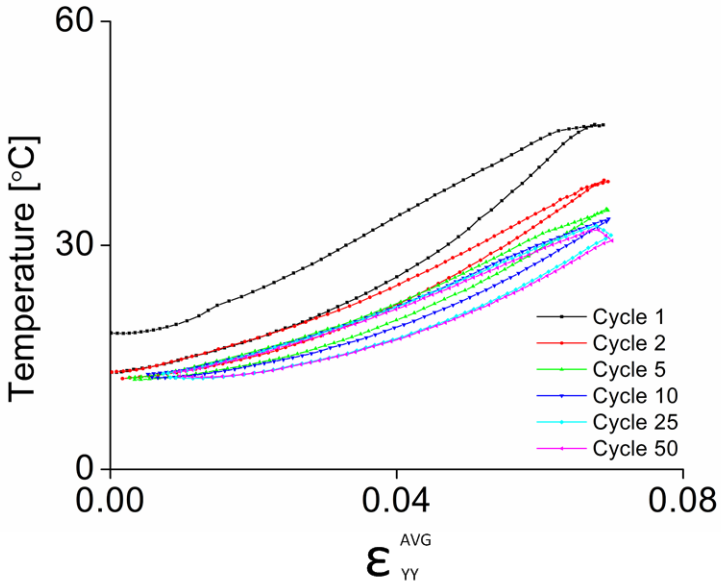

(a)

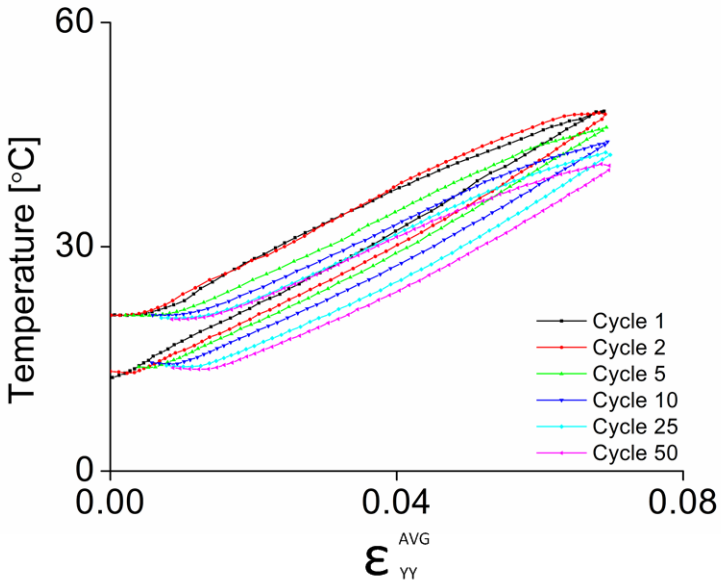

(b)

Figure 5-7 Averaged temperature as a function of averaged axial strain in the gage section of the specimen for all cycles at $\dot{\varepsilon}_g = 10^{-2}$ s^{-1} (a) with no holding between cycles, and (b) with a 1800 second hold time between cycles.

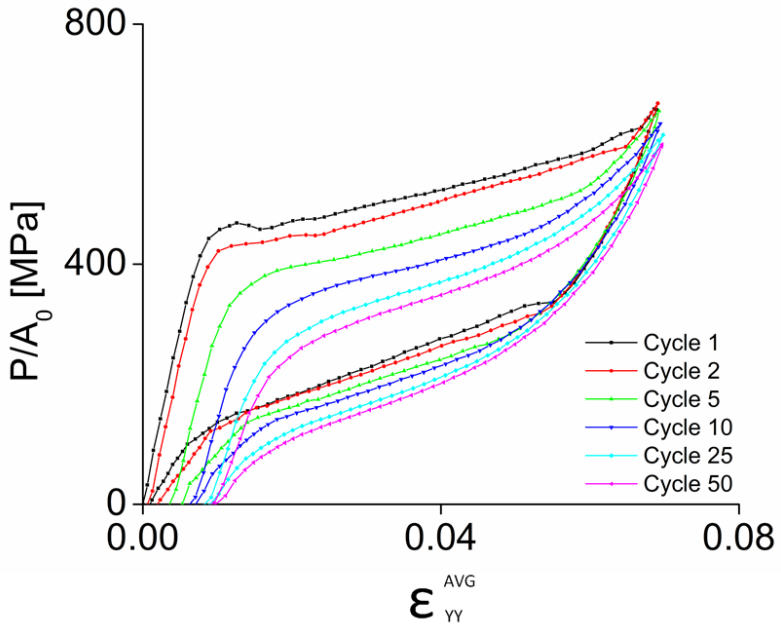

Figure 5-8 Macroscopic stress-strain curves as a function of cycling, at a globally applied strain rate of $\dot{\varepsilon}_g = 10^{-2}\ s^{-1}$. A hold of 1800 seconds is prescribed between each cycle. Specimen crystallographic texture for these tests is in the rolling direction of the sheet.

the amount of hysteresis between the without-hold and with-hold tests is relatively constant. The large drop of the transformation stress and amount of dissipated energy between cycles 1 and 2 in the without-hold test is likely due to the absorbed latent heat from cycle 1, causing a cooler specimen temperature at the start of cycle 2. However, the fast degradation of these factors still exist at applied strain rate of $\dot{\varepsilon}_g = 10^{-2}\ s^{-1}$ due not only to the effect of residual latent heat from previous cycles but also to the pure effect of strain rate without the accumulated latent heat from the previous cycle.

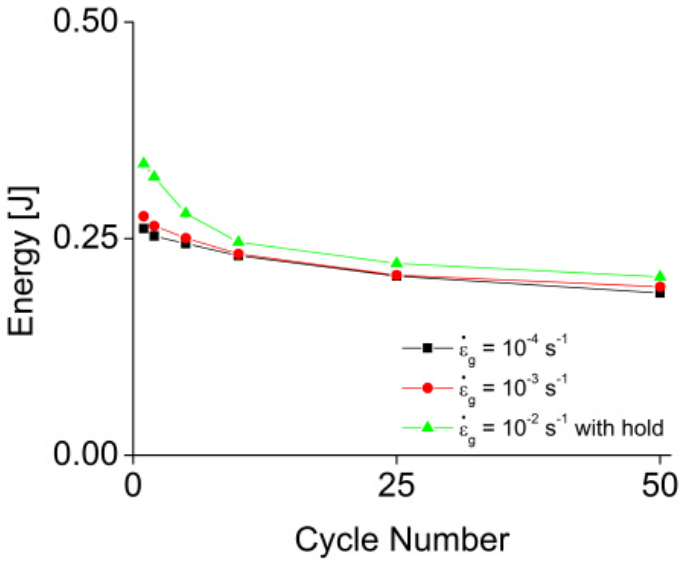
0.50
0.25
0.00
Energy [J]
0
25
50
Cycle Number
$\dot{\varepsilon}_g$ = 10^{-4} s^{-1}
$\dot{\varepsilon}_g$ = 10^{-3} s^{-1}
$\dot{\varepsilon}_g$ = 10^{-2} s^{-1} with hold

(a)

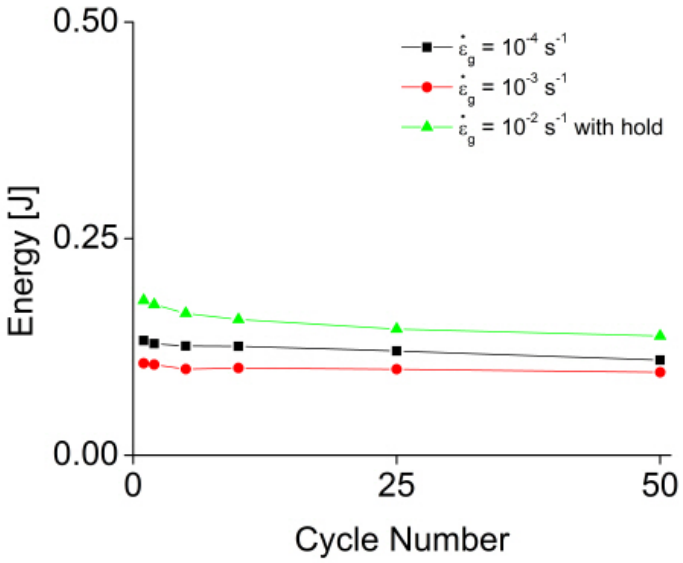
0.50
0.25
0.00
Energy [J]
0
25
50
Cycle Number
$\dot{\varepsilon}_g$ = 10^{-4} s^{-1}
$\dot{\varepsilon}_g$ = 10^{-3} s^{-1}
$\dot{\varepsilon}_g$ = 10^{-2} s^{-1} with hold

(b)

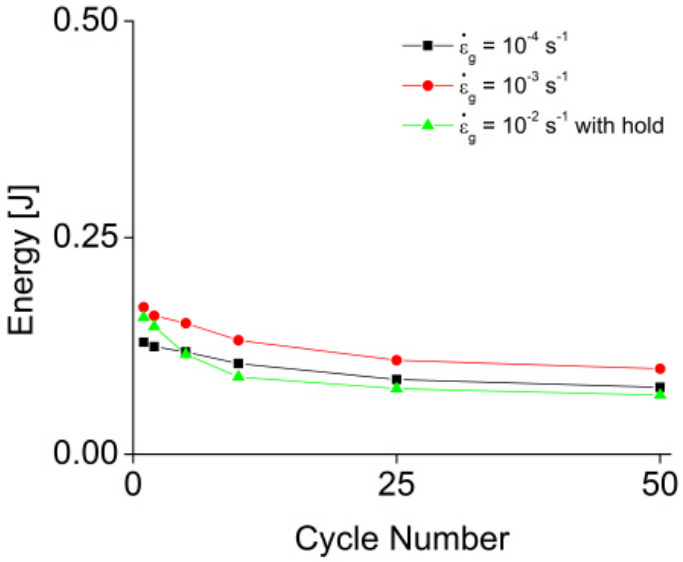

(c)

Figure 5-9 The following values, calculated for a test at $\dot{\varepsilon}_g = 10^{-2}\ s^{-1}$ with a 1800 second hold between each cycle: (a) dissipated energy during loading, (b) absorbed energy during unloading; and (c) hysteresis. The amount of both dissipated and stored energy in with-hold test increases over without-hold test, thus the amount of hysteresis between without-hold and with-hold tests is relatively the same.

In both the with-hold and without-hold tests, an interesting result was observed with regard to the location of the first new martensitic band at cycle 2. Generally, the nucleation of the martensitic phase transformation has been considered as random in the absence of a defined stress concentration. However, in the without-hold tests, it was observed that the location of the first new martensitic band at cycle 2 was consistently close to the location where the reverse phase transformation completed in cycle 1, as shown in figure 5-10(a). The location of the last coalescence of reverse phase transformation is usually near the fillets of the gage section due to stress concentration. Figure 5-10(a) shows the strains calculated down the center line of the at two points in time, the end of reverse phase transformation during cycle 1 (black line), and the

beginning of the martensitic phase transformation during cycle 2 (red line). Though two martensitic bands concurrently nucleate at the beginning of cycle 2, the right side band is near the position of the last reverse transformation. In contrast, in the with-hold test, the location of the first martensitic band at cycle 2 is the middle of the specimen regardless of the location where the reverse phase transformation completed at cycle 1. Without holding, the lower local temperatures from the latent heat of cycle 1 affects the location of the first martensitic band at cycle 2 because the stress required to nucleate the martensitic band decreases with the decrease of temperature. In order to examine this hypothesis, the line temperature down the center line of the specimen was extracted from the IR image of 0.5 second before the first band nucleates. Both the line strain and the line temperature where the first bands nucleate and 0.5 second before, respectively are shown in figure 5-10(b). It is evident that the martensitic transformation starts at a location with a minimum in local temperature, located at the top of the specimen. This observation is consistent across all textures (RD, 45°, TD) at strain rate of $\dot{\varepsilon}_g = 10^{-2}\ s^{-1}$. Consequently, at fast strain rate, it is anticipated where the martensitic phase transformation initiates by the location of the last reverse phase transformation in the previous cycle.

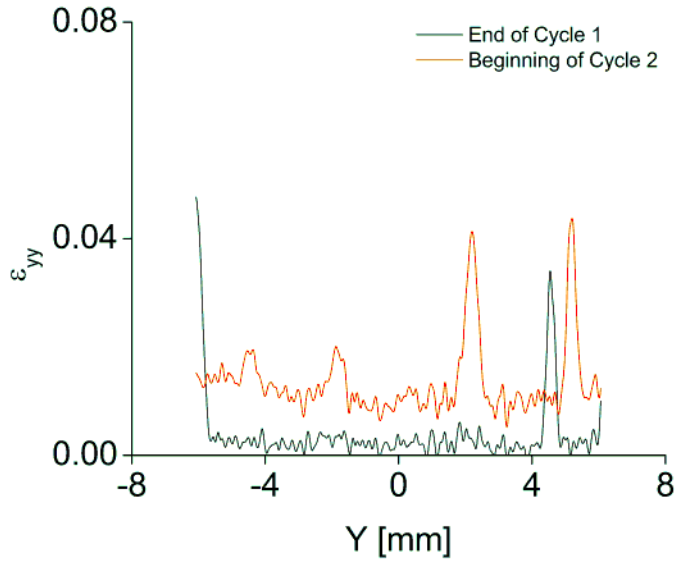

(a)

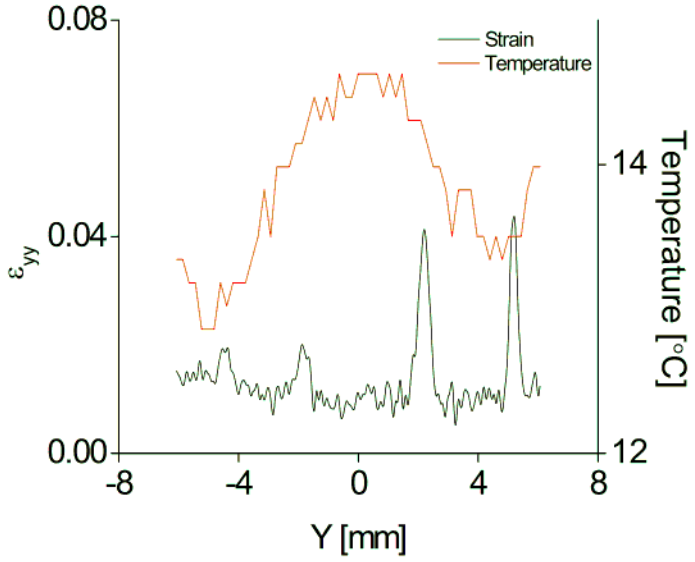

(b)

Figure 5-10 In a without-hold test at an applied strain rate of 10^{-2}: (a) strains down the center line of the specimen at the end of reverse phase transformation in cycle 1 (black) and at the beginning of the martensitic phase transformation in cycle 2 (red) and (b) strain (black) where the first martensitic bands nucleate in cycle 2 and line temperature (red) at 0.5 second before where the first martensitic bands nucleate. The martensitic transformation starts at the lower local temperature.

5.4. The Relationship between Transformation Stress and Temperature

Surface temperature changes have been tracked in past research in order to observe the stress-induced martensitic phase transformation by their released (absorbed) latent heat during forward (reverse) phase transformation [5, 16, 17]. Although the latent heat released (absorbed) is generally assumed to be where the A->M (M->A) phase transformation occurs, the locations of maximum and minimum latent heat was verified in these tests. In these tests, it was found that the latent heat is maximally released (absorbed) at the phase boundary during loading (unloading).

The relationship between transformation stress and local temperature is examined through the full-field, corresponding strain and temperature maps. It is first shown that the local maximum (minimum) temperatures closely follow the phase boundaries during loading (unloading), independent of the applied strain rate and cycling. The maximum (minimum) temperature of the specimen is on the boundary of the martensitic band during loading (unloading) as shown in figure 5-11 for cycles 1 and 50, at all three strain rates. The pixels of the maximum and the minimum temperatures in the IR images are aligned and overlaid on the DIC images (using white and black pixels, respectively), and the maximum (minimum) temperature at every image is close to the boundary of the transformation bands as indicated in the red circles in figure 5-11. At an applied strain rate of $\dot{\varepsilon}_g = 10^{-4}\ s^{-1}$, a small degree of error appears because the temperature difference is only 3.9 °C. However, as the applied strain rate increases and the temperature difference increases (to 19.7 °C and 39.6 °C at strain rates of $\dot{\varepsilon}_g = 10^{-3}\ s^{-1}$ and $\dot{\varepsilon}_g = 10^{-2}\ s^{-1}$ respectively), the peak temperatures and phase boundary match well. Note that in

figure 5-11, there exist possible errors including the difference between DIC and IR images resolution at ±1.14 mm spatial error, specimen alignment error, and IR camera sensitivity.

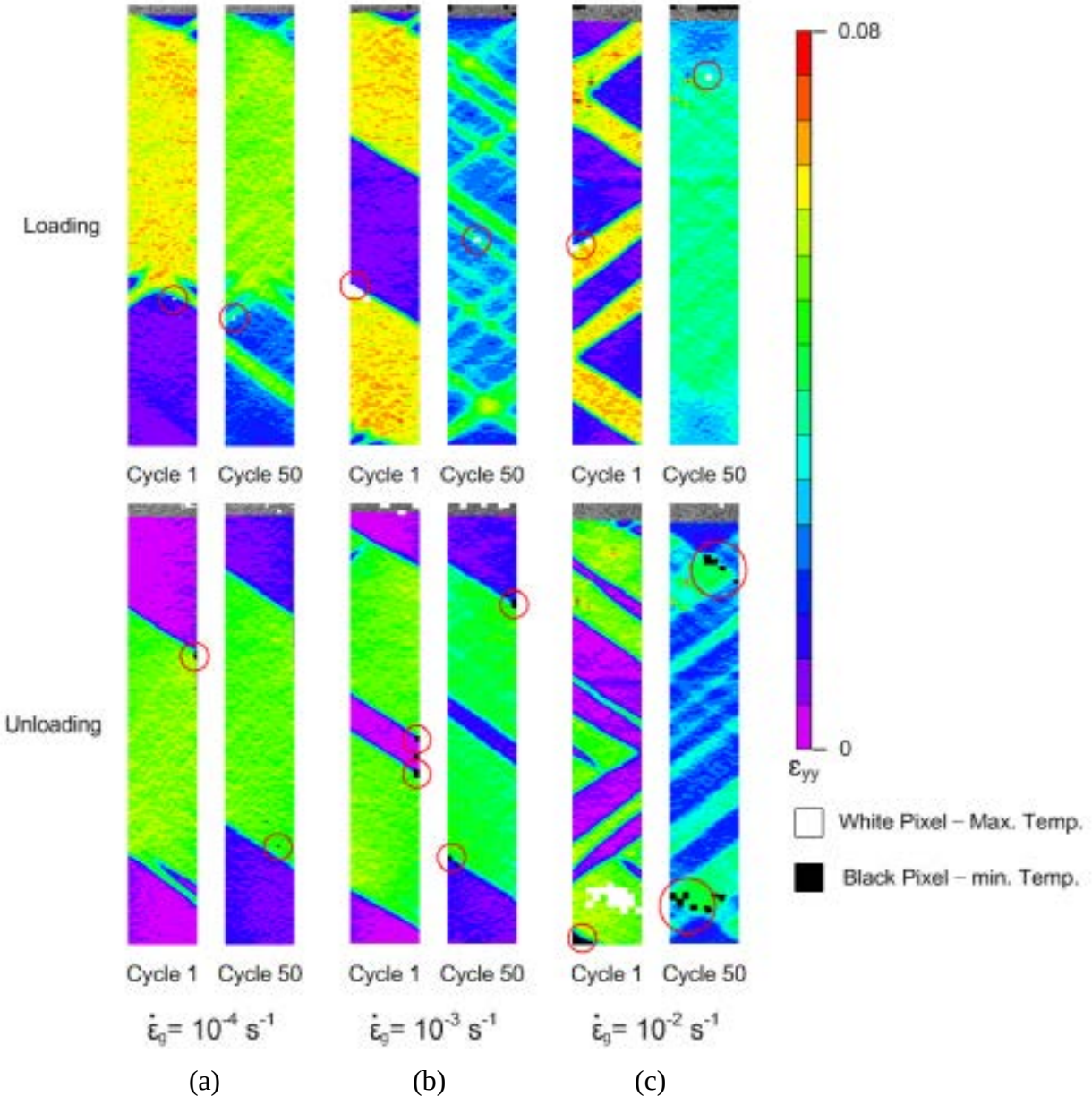

Figure 5-11 Strain field images overlaid with the maximum (minimum) temperatures determined from IR imaging during A->M (M->A) transformation. The locations of maximum and minimum temperature are indicated by white and black pixels, respectively. The globally applied strain rate is (a) $\dot{\varepsilon}_g = 10^{-4}\ s^{-1}$, (b) $\dot{\varepsilon}_g = 10^{-3}\ s^{-1}$ and (c) $\dot{\varepsilon}_g = 10^{-2}\ s^{-1}$. The maximum and minimum temperatures amass at the phase boundary during both loading and unloading.

Macroscopic stress–strain curves (from DIC-averaged data) are overlaid with both the maximum/minimum temperature-strain curves, and shown in figure 5-12 for the three applied strain rates. Note that only the maximum temperature is shown during loading and only the minimum temperature is shown during unloading. Though temperature changes at $\dot{\varepsilon}_g = 10^{-4}\ s^{-1}$ (figure 5-12(a)) are relatively small at ~4 °C, the fluctuation of peak temperature directly corresponds to the stress peaks observed in the macroscopic stress–strain curve. When the localized martensitic band nucleates upon loading, the maximum temperature jumps approximately 0.9°C from the accompanying release of latent heat. When small branches nucleate at the end of the primary boundary of the localized band, stress and maximum temperature fluctuate together during loading, shown at select points by arrows in figure 5-12(a). Similarly, the coalescence of two martensitic bands during unloading causes a substantial stress rise and a corresponding drop in the minimum temperature due to latent heat absorption. There also exists a continuous temperature drop during the A → M transformation at $\dot{\varepsilon}_g = 10^{-4}\ s^{-1}$ from the effective dissipation of released latent heat into the ambient environment (air). A large jump in the maximum temperature is clearly observed at all applied strain rates whenever the localized martensitic band nucleates, as seen in figures 5-12 (a) through (c). Because the maximum temperature at $\dot{\varepsilon}_g = 10^{-2}\ s^{-1}$ increases to > 50 °C, which is above the capacity of the IR camera, the maximum temperature >50°C could not be obtained in the region indicated by the arrow and dotted box ($\varepsilon_{YY}^{AVG} = 6.0\%$ to 6.9%). The accumulated latent heat strongly increases specimen temperature during loading at fast strain rates because there is not enough time to escape released latent heat. This increasing temperature of the specimen in turn increases the stress required for phase transformation, which is evident in the macroscopic stress-strain curve.

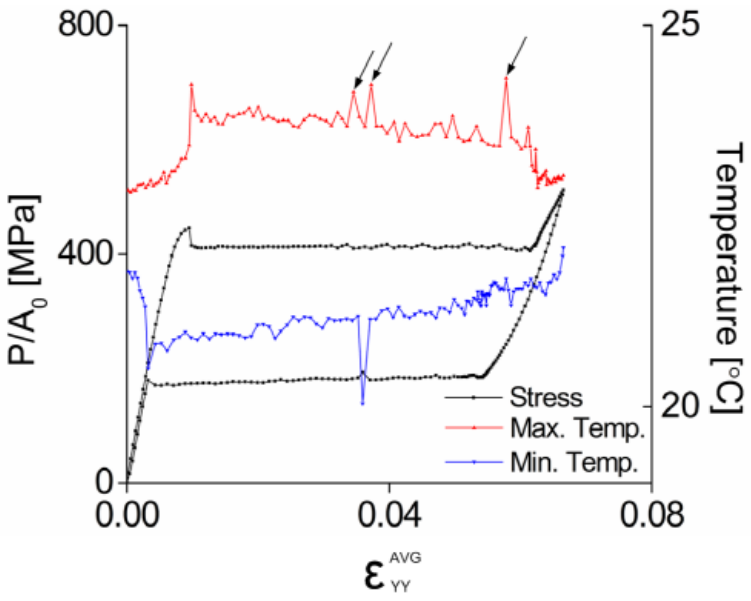
800
400
0
25
20
0.00
0.04
0.08
P/A0 [MPa]
Temperature [°C]
Stress
Max. Temp.
Min. Temp.
ε AVG YY

(a)

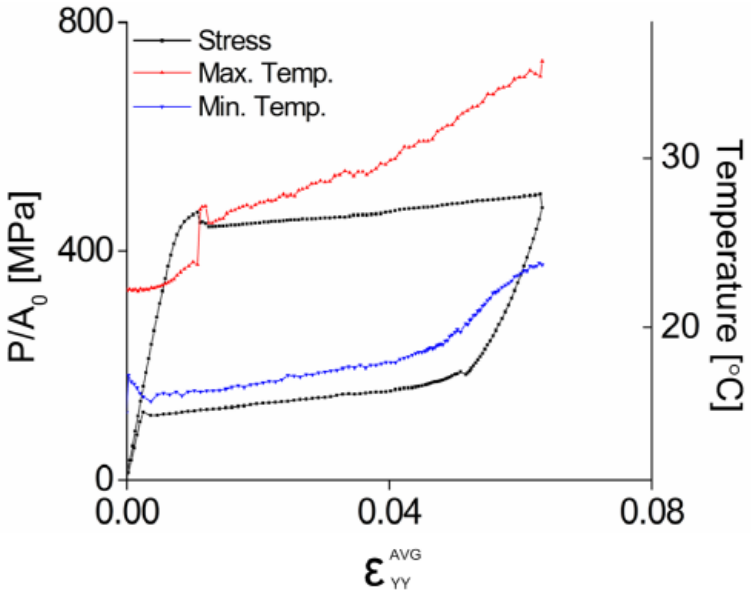
800
400
0
30
20
0.00
0.04
0.08
P/A0 [MPa]
Temperature [°C]
Stress
Max. Temp.
Min. Temp.
ε AVG YY

(b)

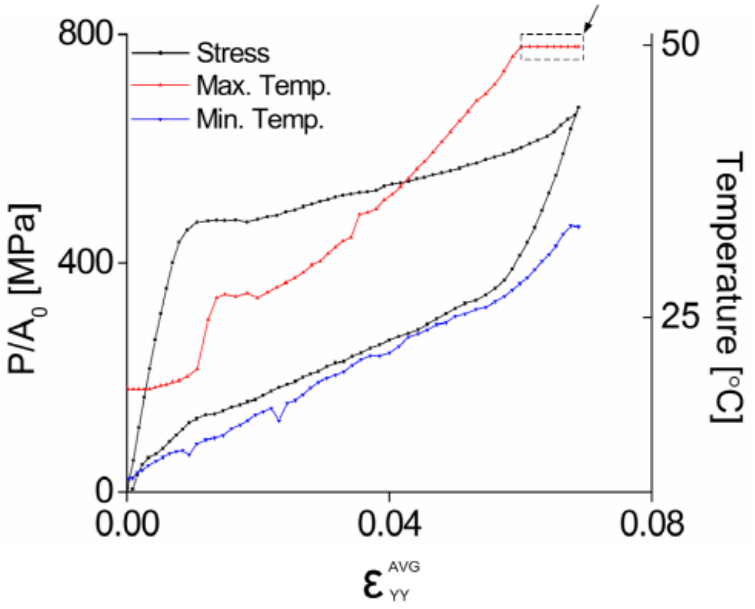

(c)

Figure 5-12 Macroscopic stress-strain curve overlaid with temperature-strain plots for the maximum (loading) and minimum (unloading) temperature at a globally applied strain rate of (a) $\dot{\varepsilon}_g = 10^{-4}\ s^{-1}$, (b) $\dot{\varepsilon}_g = 10^{-3}\ s^{-1}$ and (c) $\dot{\varepsilon}_g = 10^{-2}\ s^{-1}$. A large jump in the maximum temperature is observed at all strain rates with the nucleation of a localized martensite band. The nucleation of small branches from the primary martensite band directly corresponds to the fluctuation in stress and temperature values at the applied strain rate of $\dot{\varepsilon}_g = 10^{-4}\ s^{-1}$.

The larger amount of accumulated latent heat at faster strain rates significantly raises the stress required for phase transformation. To quantitatively investigate the relation between transformation stress and latent heat, the phase transformation stress ($\sigma^{\dagger}$) and temperature ($T^{\dagger}$) are examined, where $\sigma^{\dagger}$ and $T^{\dagger}$ refer to the global stress and the maximum temperature (corresponding to the temperature at the phase front during transformation). In order to define these variables, the 0.1 % linear offset method described in chapter 4.2 was used to determine the start and end of the transformation plateau in the stress-strain curve, and the local temperature

and global stress values of the phase transformation section were extracted from the IR imaging and load data, respectively. The $\sigma^{\dagger}$ and $T^{\dagger}$ values are plotted in figure 5-13 during loading and unloading for the applied strain rates of $\dot{\varepsilon}_g = 10^{-3}\ s^{-1}$ and $\dot{\varepsilon}_g = 10^{-2}\ s^{-1}$. The linear regions in the $\sigma^{\dagger}$ - $T^{\dagger}$ plots shown in figure 5-13 indicate macroscopic phase transformation proceeding by large localized martensitic bands, and the non-linear regions indicate microscopic phase transformation before the nucleation of large localized bands of martensite (austenite) during loading (unloading). Note that due to an IR camera limitation, a small set of the temperature data is erroneously limited to 50°C; this region is indicated by the red dotted box and arrow in figure 5-13(c). The $\sigma^{\dagger}$ - $T^{\dagger}$ slopes in figures 5-13 (a) – (d) are calculated using only the linear portion of the plot (the macroscopic phase transformation proceeding by deformation bands), and these slopes are tabulated in table 5-3. The $d\sigma^{\dagger}/dT^{\dagger}$ slope is an indicator for how much more difficult (easy) phase transformation becomes as latent heat accumulates (absorbs or escapes) during loading (unloading). Note that $d\sigma^{\dagger}/dT^{\dagger}$ during loading at $\dot{\varepsilon}_g = 10^{-3}\ s^{-1}$ is nominally the same for all cycles except the second cycle, in which its value undergoes a big drop. During the second cycle at $\dot{\varepsilon}_g = 10^{-3}\ s^{-1}$, three major martensitic bands and small offshoot branches appear, which causes the specimen temperature to increase. However, because the stress required for propagation is smaller than the stress required for nucleation, the stress reduces in value. The temperature rise from the numerous band nucleations and the simultaneous stress drop result in drop in $d\sigma^{\dagger}/dT^{\dagger}$ during the second cycle at $\dot{\varepsilon}_g = 10^{-3}\ s^{-1}$. As cycling increases, the change in maximum temperature (on the phase front) $dT^{\dagger}$ decreases because of an increased number of martensitic bands and a more spatially homogeneized transformation. However, the change in global stress required for transformation, $d\sigma^{\dagger}$, increases with cycling during loading showing

slightly inclined stress plateau as shown in figures 5-4(b) and (c). Thus, $d\sigma^{\dagger}/dT^{\dagger}$ increases as cycling increases. This cycling effect during loading is more evident at faster strain rates as shown in table 5-3 because of more residual martensite and more homogenization of macroscopic phase transformation at faster strain rates. As the applied strain rate increases, both $d\sigma^{\dagger}$ and $dT^{\dagger}$ increase during loading because greater accumulated latent heat trapped during phase transformation. During unloading, $d\sigma^{\dagger}/dT^{\dagger}$ is not affected by cycling as evidenced by the much more stable stress for reverse phase transformation under cycling.

Table 5-3 Tabulated values of $d\sigma^{\dagger}/dT^{\dagger}$ at the applied strain rate of $\dot{\varepsilon}_g = 10^{-3}\ s^{-1}$ and $\dot{\varepsilon}_g = 10^{-2}\ s^{-1}$.

	$d\sigma^{\dagger}/dT^{\dagger}$ [MPa/°C]			
Strain Rate	$10^{-3}\ s^{-1}$		$10^{-2}\ s^{-1}$	
Cycle	Loading	Unloading	Loading	Unloading
1	6.4	18.3	5.3	16.5
2	3.3	16.8	7.2	17.5
5	6.2	17.7	8.2	18.3
10	6.6	17.6	8.8	18.7
25	6.9	17.1	11.7	20.5
50	8.6	17.4	12.8	21.1

5.5. Martensitic Volume Fraction

A estimate of the evolution of the martensitic volume fraction is obtained using a rule of mixtures, where each of the nominally 600,000 strain values in the image are taken and each binned by a rule of mixtures into a percentage austenite and a percentage martensite. Note that this is an estimate of evolution, and because it relies of the local strain values as an indicator of transformation, comparing between tests on specimens with different crystallographic textures is not valid. First, four critical strain points, M_s, M_f, A_s and A_f, are calculated using a 0.1% offset

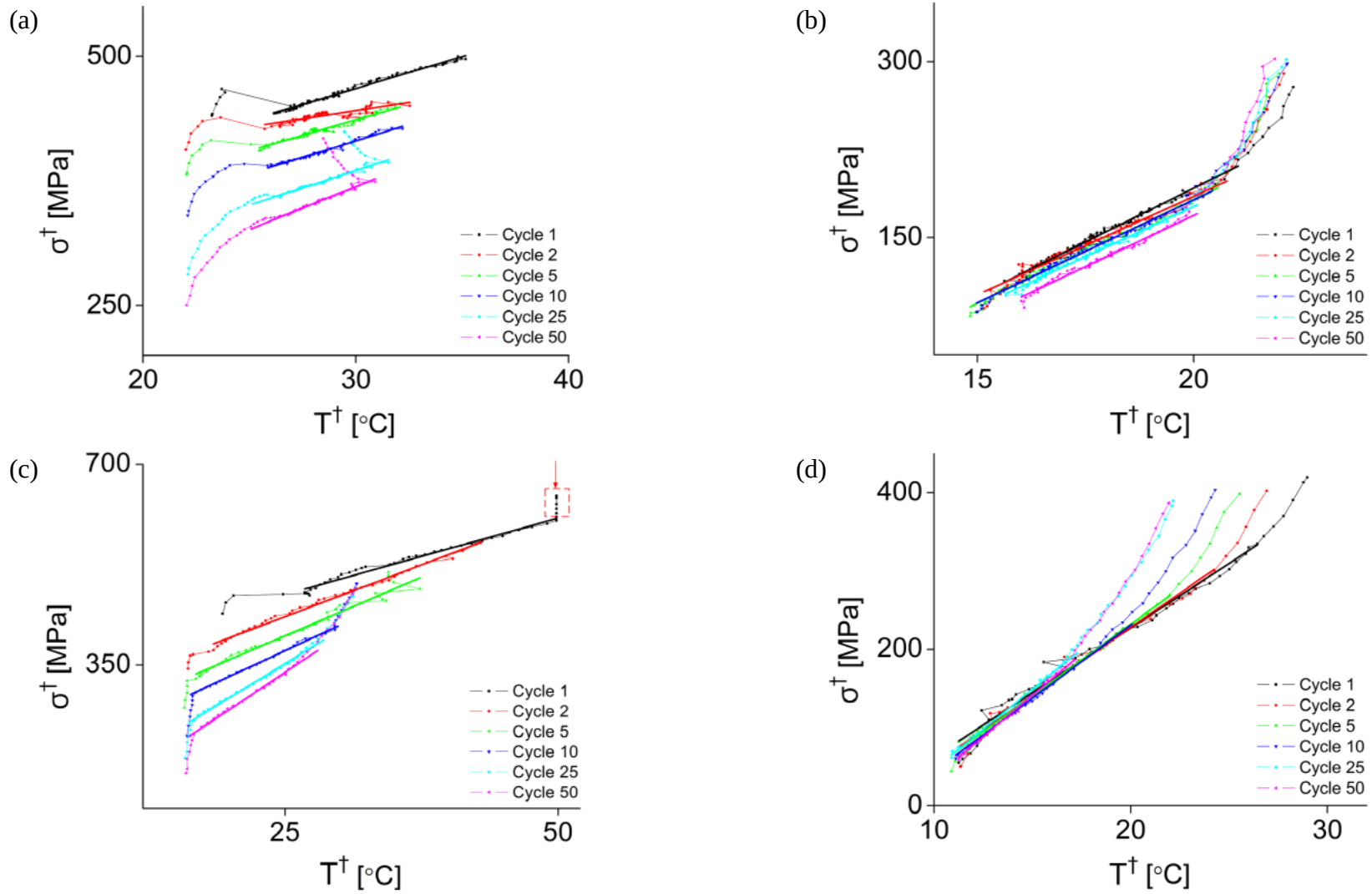

Figure 5-13 The global stress at phase transformation ($\sigma^{\dagger}$) versus maximum (minimum) temperature ($T^{\dagger}$) located at the phase boundary upon loading (unloading), plotted (a) during loading at $\dot{\varepsilon}_g = 10^{-3}\ s^{-1}$, (b) during unloading at $\dot{\varepsilon}_g = 10^{-3}\ s^{-1}$, (c) during loading at applied $\dot{\varepsilon}_g = 10^{-2}\ s^{-1}$, and (d) during unloading at $\dot{\varepsilon}_g = 10^{-2}\ s^{-1}$. The slope, $d\sigma^{\dagger}/dT^{\dagger}$, shows the effect of latent heat on the difficulty of transformation.

from the relevant linear region on the macroscopic stress-strain curve. M_s and M_f are the starting and finishing data points of martensitic phase transformation during loading, and A_s and A_f are the starting and finishing data points of austenitic phase transformation upon unloading. These four points determine whether a pixel is considered as pure austenite, pure martensite or a value between austenite and martensite. The values of M_s, M_f, A_s and A_f change with experimental conditions, such as cycling number and strain rate, and need to be redetermined. The martensitic volume fraction is obtained at each individual image, which consists of approximately 600,000 pixels of gage section, by a rule-of-mixtures approach,

$$\delta_M = \frac{N_M}{N_{Total}} \quad \text{(Eqn. 10)}$$

where N_M is the amount of martensite in all of the pixels and N_{Total} is the total number of pixels in the image. The sum amount of martensite in all of the pixels (N_M) consists of the sum of M_P and M_T, where M_P is the number of pure martensite pixels and M_T is the summed martensite fraction of the pixels that are considered as partially martensite,

$$M_T = \frac{\varepsilon - \varepsilon_{M_s}}{\varepsilon_{M_f} - \varepsilon_{M_s}} \text{ (Loading)} \quad \text{(Eqn. 11)}$$

$$M_T = \frac{\varepsilon - \varepsilon_{A_f}}{\varepsilon_{A_s} - \varepsilon_{A_f}} \text{ (Unloading)} \quad \text{(Eqn. 12)}$$

The results at $\dot{\varepsilon}_g = 10^{-4}$, 10^{-3}, and 10^{-2} s^{-1} are shown in figures 5-14 through 5-16, respectively. At each set strain rate, cycling affects the evolution of martensitic volume fraction.

The stresses required for the nucleation and propagation of martensite decrease because of increasing residual martensite nuclei and the establishment of dislocation networks, as previously discussed. However, the evolution of martensitic volume fraction during unloading is not significantly affected by cycling, consistent with the observation that the stress for M->A phase transformation during unloading stays nominally stable with cycling. An increased strain rate also decreases the slope of the stress – volume fraction curve during phase transformation. At an applied strain rate of $\dot{\varepsilon}_g = 10^{-4}\ s^{-1}$, the linear region of martensite volume fraction is nominally parallel with the y-axis, but the slope of this linear region decreases as strain rate increases due to increasing stress plateau in the stress – strain curve caused by accumulated latent heat. During loading, the nucleation stress of martensite is higher at a faster strain rate at the first cycle because of simultaneous nucleation of multiple martensitic bands due to local temperature gradient by released latent heat. However, the nucleation stress at the applied strain rate of $\dot{\varepsilon}_g = 10^{-2}\ s^{-1}$ is lower than the nucleation stress at $\dot{\varepsilon}_g = 10^{-4}\ s^{-1}$ and $\dot{\varepsilon}_g = 10^{-3}\ s^{-1}$ in cycle 50 due to more pronounced cycling effect at faster strain rates.

5.6. Velocity of Martensitic Front

The velocity of martensitic bands during loading at $\dot{\varepsilon}_g = 10^{-3}\ s^{-1}$ is obtained and compared with the previous result (chapter 3.1) for a single martensitic band during loading at $\dot{\varepsilon}_g = 10^{-4}\ s^{-1}$, as shown in figure 5-17. At a globally applied strain rate of $\dot{\varepsilon}_g = 10^{-4}\ s^{-1}$, only one front nucleated with small off shoot branches and the velocity of front was calculated as 0.04 mm/s (chapter 3.1). For the applied strain rate of $\dot{\varepsilon}_g = 10^{-2}\ s^{-1}$, because several fronts and

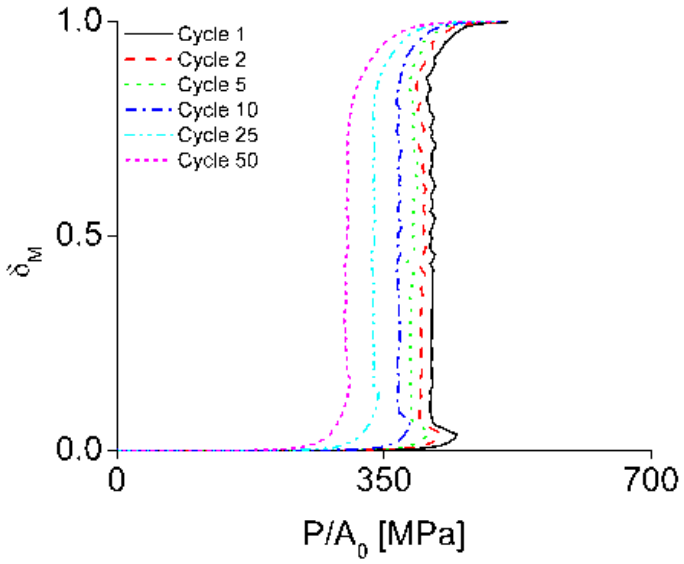

(a)

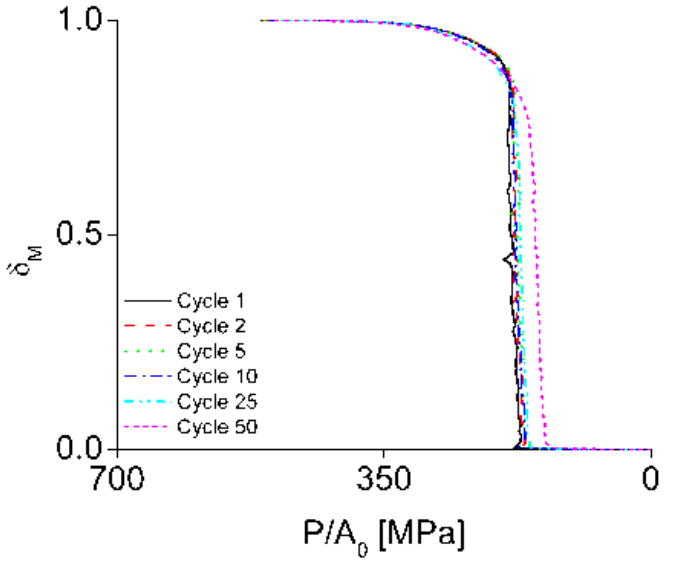

(b)

Figure 5-14 The evolution of martensite volume fraction of all cycles at the applied strain rate of $\dot{\varepsilon}_g = 10^{-4}\ s^{-1}$ upon (a) loading and (b) unloading. The linear line of martensite volume fraction is nominally parallel to the y-axis and the stress for transformation during loading decreases with cycling coinciding the macroscopic response. The evolution of martensitic volume fraction during unloading is not significantly affected by cycling.

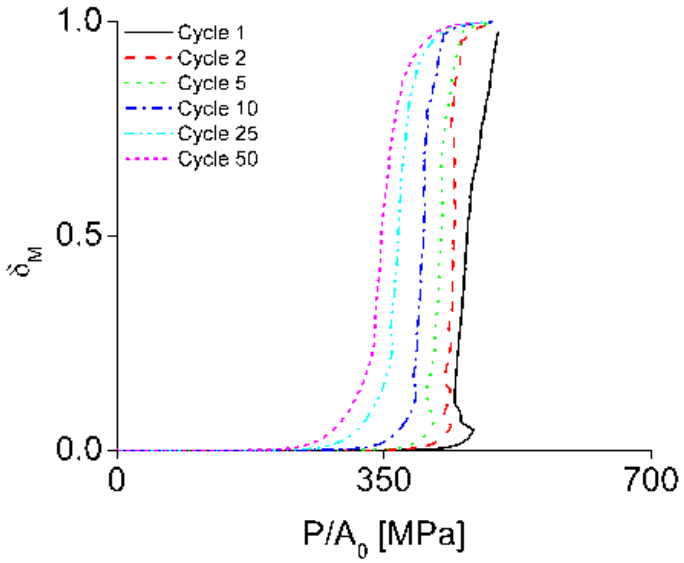

(a)

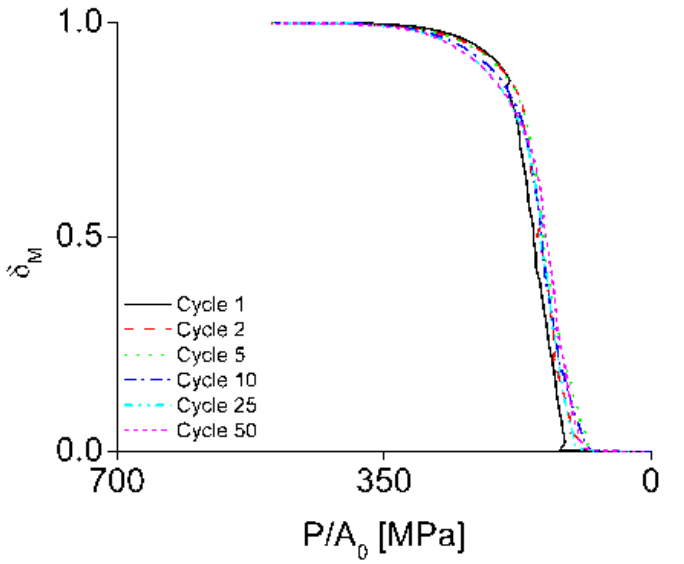

(b)

Figure 5-15 The evolution of martensite volume fraction of all cycles at the applied strain rate of $\dot{\varepsilon}_g = 10^{-3}\ s^{-1}$ during (a) loading and (b) unloading. The slope of the linear (transformation) region becomes inclined and the stress for transformation during loading decreases with cycling coinciding the macroscopic response. The evolution of martensitic volume fraction during unloading is not significantly affected by cycling.

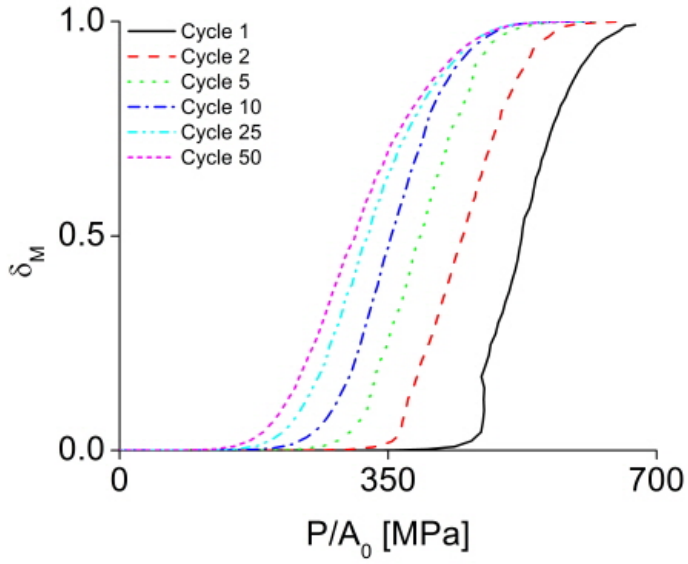

(a)

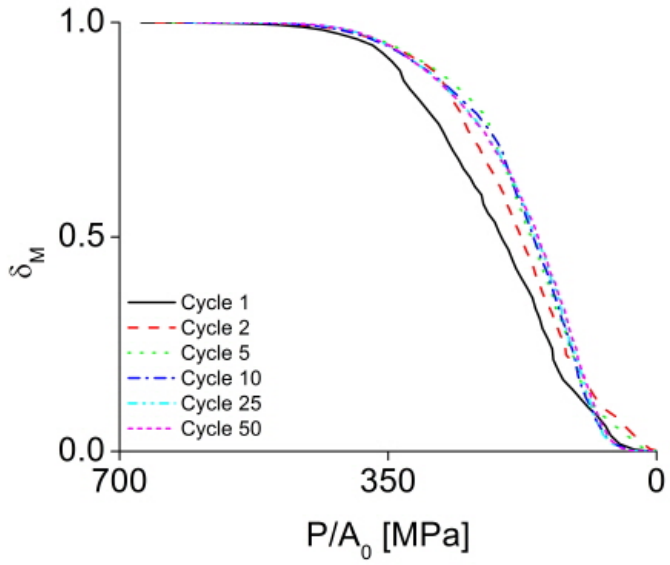

(b)

Figure 5-16 The evolution of martensite volume fraction of all cycles at the applied strain rate of $\dot{\varepsilon}_g = 10^{-2}\ s^{-1}$ during (a) loading and (b) unloading. The slope of the linear (transformation) region is further inclined from figure 5-15 due to accumulated latent heat, and the decrease in stress for transformation during loading with cycling. The evolution of martensitic volume fraction during unloading is not significantly affected by cycling.

branches nucleate and coalesce in a short amount of time, the velocity of the front at $\dot{\varepsilon}_g = 10^{-2}\ s^{-1}$ is not feasible to calculate. At the applied strain rate of $\dot{\varepsilon}_g = 10^{-3}\ s^{-1}$, two major martensitic fronts nucleate and propagate with three small off shoot branches during the first loading cycle. The schematic on the right side of figure 5-17 shows the identification of fronts and branches: the lower major front is denoted by Front A, the upper major front is denoted by Front B, the branches are denoted by Branch a, b, and c as follow the order of nucleation. There are two boundaries to each front or branch, denoted as the upper (+) and lower (-) boundary. The velocities of all boundaries are measured perpendicular to the linear line of the boundary and the front propagation direction is taken as positive. The sum of absolute values of V^- and V^+ of each front and branch are calculated as $V_i = V_i^- + V_i^+$ where *i* denotes a specific front or branch. All front and branch velocities are shown in the figure 5-17.

The major fronts (A and B) interact with each other. During the propagation of front A, which nucleates at an average strain of $\varepsilon_{YY}^{AVG} = 0.0117$, front B nucleates at the upper right of the specimen at an average strain of $\varepsilon_{YY}^{AVG} = 0.0133$. When front B nucleates, the velocity of front A immediately decreases from 0.344 mm/s to 0.058 mm/s while the starting velocity of Front B is extremely fast at 0.416 mm/s as shown in figure 5-17. During the propagation of the two fronts, this trend continues: if the velocity of one front increases, the velocity of the other decreases. After an average strain of $\varepsilon_{YY}^{AVG} = 0.0484$, which is after dash-dot line with an arrow in figure 5-17, both front A and B velocities decrease because the upper boundary of front B (V_B^+) and the lower boundary of front A (V_A^-) exit the analyzed region. Though all of the branch velocities are relatively slow in comparison to front velocities, one of the two front velocities slowed whenever

a new branch nucleated, as shown by the labeled points in ① - ③ in figure 5-17. Some velocities of branches are negative because propagation of these branches is relatively smaller compared to the displacement of the specimen. For example, while the bottom of branch c remains stable, the specimen is still elongated upwards. In this case, the velocity of branch c is expressed by negative value.

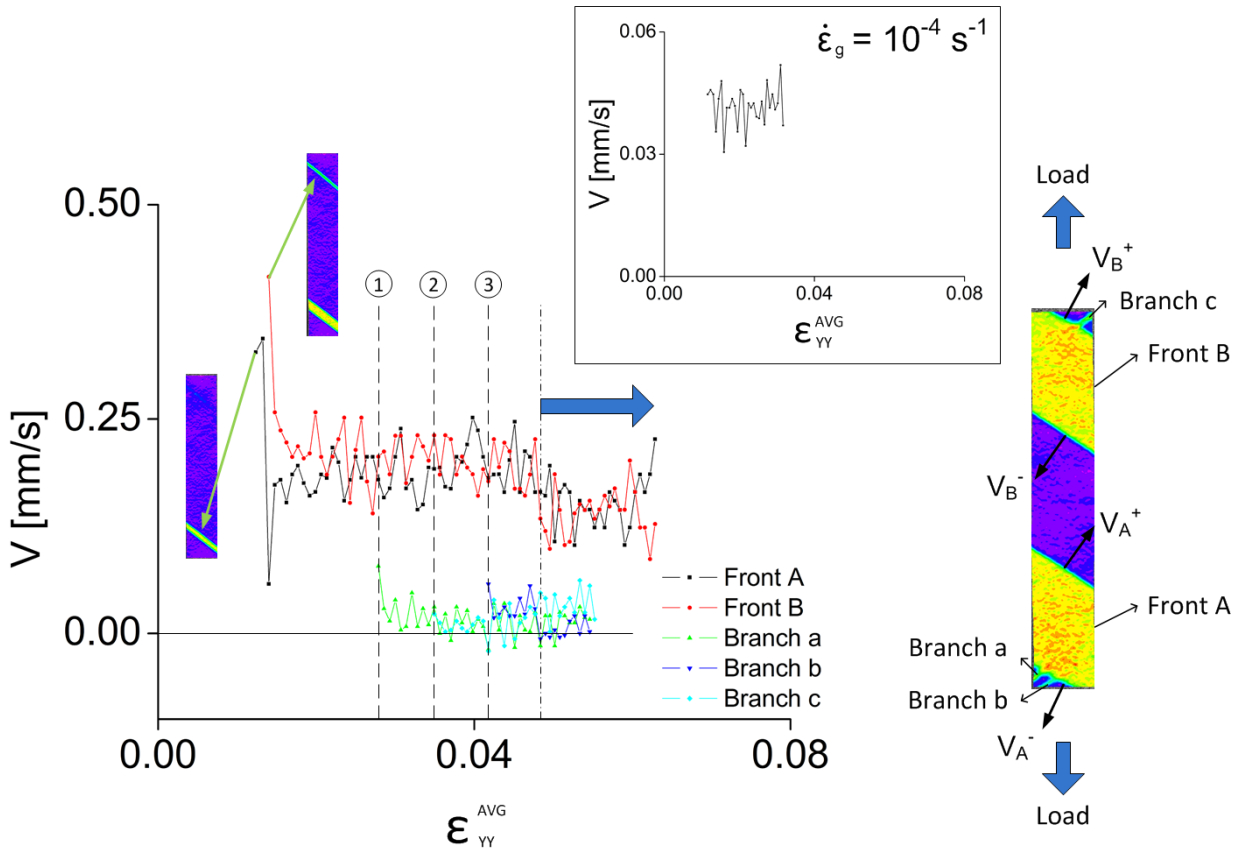

Figure 5-17 The velocities of the localized stress-induced martensitic bands and offshoot branches from the bands, during loading at the applied strain rate of $\dot{\varepsilon}_g = 10^{-3}\ s^{-1}$. During the propagation of two front, If the velocity of one front increases, the velocity of the other decreases. The nucleation of the offshoot branches will cause a decrease in one of the front velocities.

A small graph of front velocity at the applied strain rate of $\dot{\varepsilon}_g = 10^{-4}$ s^{-1} is inserted in figure 5-17 at the top right of the macroscopic stress-strain curve. The velocity of the single front that nucleates and propagates at $\dot{\varepsilon}_g = 10^{-4}$ s^{-1} is measured before the nucleation of small off shoot branches from that front. Its average velocity is 0.04 ± 0.005 mm/s. At the applied strain rate of $\dot{\varepsilon}_g = 10^{-3}$ s^{-1}, the average front velocity is 0.18 mm/s. Shaw and Kyriakides [2] defined an equation of the velocity of fronts with an assumption of propagating two fronts at the same constant velocity as

$$nc\Delta\varepsilon_t = \dot{\delta} \qquad \text{(Eqn. 13)}$$

where n is the number of fronts, c is constant speed of propagating fronts, $\Delta\varepsilon_t$ is the change of strain during the stress plateau, and $\dot{\delta}$ is the applied displacement rate. Based on the equation 13, another equation is defined considering the velocity of branches and relationship between propagating fronts and branches. Because two major bands exist at $\dot{\varepsilon}_g = 10^{-3}$ s^{-1}, the equation for velocity is defined as

$$V_2 + v_2 = \frac{N_1}{N_2} \times \frac{\dot{\varepsilon}_2}{\dot{\varepsilon}_1} \times (V_1 + v_1) \qquad \text{(Eqn. 14)}$$

where V is the average front velocity, v is the average branch velocity, N is the number of fronts, and $\dot{\varepsilon}$ is the globally applied strain rate. The subscript 1 denotes a nominally quasi-static experiment and the subscript 2 denotes an experiment at faster applied strain rate. Here, the results are fit into equation (14) as follows,

$$\frac{N_1}{N_2}\times\frac{\dot{\varepsilon}_2}{\dot{\varepsilon}_1}\times(V_1+v_1)=\frac{1}{2}\times\frac{10^{-3}}{10^{-4}}\times(0.04+0)=0.2 \qquad \text{(Eqn. 15)}$$

$$V_2+v_2=0.18+0.018=0.198 \qquad \text{(Eqn. 16)}$$

Here, the velocity of front is closely related with the number of fronts, strain rate, and nucleation of branches. This equation was verified at applied strain rate of $\dot{\varepsilon}_g = 10^{-4}$ and 10^{-3} s^{-1}. However, it is difficult to verify at applied strain rate of $\dot{\varepsilon}_g = 10^{-2}$ s^{-1} due to the limited frame rate of image at this strain rate. Thus, this equation needs to be verified with further testing at faster strain rate with enough frame rates.

5.7. Conclusions

In this chapter, phase transformation during superelastic deformation in the shape memory alloy Nitinol is examined experimentally by simultaneous strain and thermal mapping. The effect of displacement-controlled cycling (N=1, 2, 5, 10, 25, 50) and three different globally applied strain rates ($\dot{\varepsilon}_g$=10^{-2}, 10^{-3} and $10^{-4}s^{-1}$) is investigated. Full-field and quantitative measures of surface strain and temperature are analyzed to investigate the effects of cycling and strain rate on the stress required for phase transformation, amount of energy dissipation, accumulation of residual strain, and the relationship between local temperatures at the phase boundaries and the globally applied stress. During cycling, the transformation stress, hysteresis, difference between maximum and minimum temperatures, and the increment in accumulated residual strain decrease as the transformation becomes more homogeneous and stable. As the strain rate increases, the transformation stress, slope of the transformation plateau, difference

between the maximum and minimum temperatures, and accumulated residual strain increase as both the surface temperature and number of large localized martensitic bands increase. A larger impact of cycling is also observed as the strain rate is increased. Through the combination of strain and temperature mapping, latent heat released/absorbed at the boundary of the martensitic band and the peak temperatures are observed at the boundary during loading/unloading. Thus, the relation between the local temperatures at the transformation boundary and the globally applied stress can be obtained.

- The linear elastic moduli of the austenite and martensite phases, both on loading and unloading, decrease as cycling progresses. The softening of the elastic moduli can be attributed to grain reorientation and the development of defects/dislocations, and possibly the introduction of residual martensite pockets that occur during cycling.
- The amount of dissipated energy decreases and stabilizes with cycling due to a decrease of cyclic hardening and the stress required for phase transformation. Though a large amount of dissipated energy appears at the fastest strain rate, it rapidly decreases as cycling progresses. The effect of cycling increases at faster strain rates.
- Tests were undertaken to examine the effect of a set hold time in between cycles on the macroscopic stress-strain behavior. “With-hold” tests were set with a 1800 second hold time between each cycle, and “Without-hold” tests progressed continuously. At $\dot{\varepsilon}_g = 10^{-2}\ s^{-1}$, the macroscopic stress strain curves in the ‘without-hold’ tests generally had a lower stress level than those with holding in between cycles. If one attributes this difference to temperature and not plasticity, this means that the samples without holding are in fact cooler than those with

holding – thus meaning the 'with hold' samples find it easier to dissipate heat instead of absorb heat.

- The location of band nucleation was examined in both the "with-hold" and "without-hold" tests. It was found that during the "without-hold" tests, the martensitic transformation in the subsequent cycle tends to start at the position of minimum local temperature caused by transformation coalescence in the previous cycle. Consequently, at the faster strain rates, the most likely initiation location of martensitic transformation can be predicted by the location of the last reverse phase transformation in the previous cycle.
- The maximum (minimum) temperatures during loading (unloading) are located at or very near to the boundary of the martensitic band. The relation between the local temperature at/near the phase boundary ($T^{\dagger}$) and the global stress ($\sigma^{\dagger}$) was observed to be linear during macroscopic transformation (martensitic band propagation) at most conditions examined here. During loading, the slope ($dT^{\dagger}/d\sigma^{\dagger}$) increases as cycling progresses because of increasing $d\sigma^{\dagger}$ and decreasing $dT^{\dagger}$. The impact of cyclic loading is stronger at faster strain rates. As the applied strain rate increases, both $d\sigma^{\dagger}$ and $dT^{\dagger}$ increase during loading because greater accumulated latent heat trapped during phase transformation. However, during unloading, the coefficient is nominally the same in cycling.
- Quantitative, approximate estimates of the evolution of martensitic volume fraction are obtained by a rule of mixtures where every individual pixel is binned as a certain fraction of martensite and austenite, and all fractions are summed. At each set strain rate, cycling affects the evolution of martensitic volume fraction. The stresses required for the nucleation and propagation of martensite decrease because of increasing residual martensite nuclei and the establishment of dislocation networks. However, the evolution of martensitic volume fraction

during unloading is not significantly affected by cycling, consistent with the observation that the stress for M->A phase transformation during unloading stays nominally stable with cycling. An increased strain rate also decreases the slope of the stress – volume fraction curve during phase transformation.

- The velocities and behaviors of the stress-induced martensitic bands at a strain rate of 10^{-3} are calculated and compared to the velocity of the (single) band at a strain rate of 10^{-4}. The interaction of two major fronts at a strain rate of 10^{-3} is observed. Though the two fronts have different velocities, the sum of two velocities remains relatively constant. Small offshoot branches affect the velocity of the major fronts at the applied strain rate of $\dot{\varepsilon}_g = 10^{-3}\ s^{-1}$. In addition, an equation for the velocity of the fronts is postulated.

References

[1] L. C. Brinson, I. Schmidt, and R. Lammering, "Stress-induced transformation behavior of a polycrystalline NiTi shape memory alloy: micro and macromechanical investigations via in situ optical microscopy," *Journal of the Mechanics and Physics of Solids*, vol. 52, no. 7, pp. 1549-1571, Jul. 2004.

[2] J. A. Shaw and S. Kyriakides, "Thermomechanical aspects of NiTi", *J. Mech. Phys. Solids*, vol 43, no. 8, pp.1243-1281, 1995.

[3] B. Strnadel, S. Ohashi, H. Ohtsuka, T. Ishihara, and S. Miyazaki, "Cyclic stress-strain characteristics of Ti-Ni and Ti-Ni-Cu shape memory alloys," *Materials Science and Engineering A*, vol. 202, no. 1-2, pp. 148-156, Nov. 1995.

[4] B. Strnadel, S. Ohashi, H. Ohtsuka, S. Miyazaki, and T. Ishihara, "Effect of mechanical cycling on the pseudoelasticity characteristics of Ti-Ni and Ti-Ni-Cu alloys," *Materials Science and Engineering A*, vol. 203, no. 1-2, pp. 187-196, Nov. 1995.

[5] M. A. Iadicola and J. A. Shaw, "The effect of uniaxial cyclic deformation on the evolution of phase transformation fronts in pseudoelastic NiTi wire," *Journal of Intelligent Material Systems and Structures*, vol. 13, no. 2-3, pp. 143 -155, Feb. 2002.

[6] S. Nemat-Nasser and W. G. Guo, "Superelastic and cyclic response of NiTi SMA at various strain rates and temperatures," *Mechanics of Materials*, vol. 38, no. 5-6, pp. 463-474.

[7] H. Sehitoglu, R. Anderson, I. Karaman, K. Gall, and Y. Chumlyakov, "Cyclic deformation behavior of single crystal NiTi," *Materials Science and Engineering A*, vol. 314, no. 1-2, pp. 67-74, Sep. 2001.

[8] S. Miyazaki, T. Imai, Y. Igo, and K. Otsuka, "Effect of cyclic deformation on the pseudoelasticity characteristics of Ti-Ni alloys," *Metallurgical Transactions A*, vol. 17, no. 1, pp. 115-120, 1986.

[9] K. Gall and H. J. Maier, "Cyclic deformation mechanisms in precipitated NiTi shape memory alloys," *Acta Materialia*, vol. 50, no. 18, pp. 4643-4657, Oct. 2002.

[10] Y. Liu, "Mechanical and thermomechanical properties of a Ti50Ni25Cu25 melt spun ribbon", *Materials Science and Engineering A*, vol 354, pp. 286-291, 2003

[11] S. Mao, X. Han, M. H. Wu, Z. Zhang, F. Hao, D. Liu, Y. Zhang, and B. Hou, "Effect of cyclic loading on apparent Young's modulus and critical stress in nano-subgrained superelastic NiTi shape memory alloys", *Materials Transactions*, vol. 47, no. 3, pp. 735-741, 2006

[12] R. Lammering and I. Schmidt, "Experimental investigations on the damping capacity of NiTi components", *Smart Materials and Structures*, vol. 10, pp. 853-859, 2001

[13] S. Saadat, J. Salichs, M. Noori, Z. Hou, H. Davoodi, I. Bar-on, Y. Suzuki and A. Masuda, "An overview of vibration and seismic applications of NiTi shape memory alloy", *Smart Materials and Structures*, vol. 11, pp. 218-229, 2002

[14] X. Zhang, P. Feng, Y. He, T. Yu, and Q. Sun, "Experimental study on rate dependence of macroscopic domain and stress hysteresis in NiTi shape memory alloy strips", *International Journal of Mechanical Sciences*, vol. 52, no. 12, pp. 1660-1670, 2010.

[15] G. Zadno and T. Duerig, "Linear and non-linear superelasticity in NiTi", *MRS shape memory materials*, vol. 9, pp. 201-209, 1989

[16] J. A. Shaw, "Simulations of localized thermo-mechanical behavior in a NiTi shape memory alloy," *International Journal of Plasticity*, vol. 16, no. 5, pp. 541-562, Apr. 2000.

[17] J. A. Shaw and S. Kyriakides, "On the nucleation and propagation of phase transformation fronts in a NiTi alloy," *Acta Materialia*, vol. 45, no. 2, pp. 683-700, Feb. 1997.

Chapter 6

Summary and Conclusions

6.1 Summary

This thesis presents an investigation into stress-induced martensitic phase transformation in NiTi SMA thin sheet specimens and its dependence on displacement-controlled cycling, crystallographic texture and globally applied strain rate. In addition to the macroscopic stress-strain response, local full-field maps of strain and temperature were simultaneously obtained and compared under these varied conditions. The thin sheet (254 μm) NiTi test specimens were tested under ramp profile cyclic loading (up to N=50) at three different crystallographic textures (cut along the rolling direction - RD, 45°, and transverse to the rolling direction - TD) and three global strain rates ($\dot{\varepsilon}_g = 10^{-4}$,10^{-3}, and 10^{-2} s^{-1}).

First, the critical transition temperature for phase transformation (A_f = 1.29°C) was determined to ensure that the as-received specimens exhibited superelasticity upon loading. The fundamental principles of the 3D Digital Image Correlation technique used in these tests were explained, and a number of practical recommendations to obtain accurate DIC measurements were made, such as the optical camera position, camera field-of-view (FOV) selection, lighting, focusing, appropriate specimen preparation, and sensitive calibration procedures. The overall experimental setup using a load frame with the simultaneous DIC and IR imaging was reviewed.

In chapter 3, the effect of displacement-controlled cycling on the stress-induced martensitic phase transformation was investigated under uniaxial, zero-to-tension loading at the applied global strain rate of $\dot{\varepsilon}_g = 10^{-4}\ s^{-1}$. The specimen was as-received thin sheet NiTi cut along the rolling direction (all three crystallographic textures were characterized and compared in chapter 4.1). The stress-induced martensitic phase transformation was tracked utilizing DIC and IR imaging. The macroscopically martensite region was apparent through regions of high local strains in the DIC maps and by high temperature regions on the thermal IR images. The macroscopic response (stress-strain curve) was created by averaging the ~600,000 strain values in every individual DIC image and plotting those values against the globally applied stress. It became apparent through full-field strain mapping that the stress-induced martensite phase can transform either by a single front(s) or alternatively by the offshoot of small branches from the primary phase front(s). The nucleation (coalescence) of these small branches directly corresponded to the drop (rise) of the load in the macroscopic response. As cycling progressed, the stress required to nucleate and propagate the phase front decreased. From the DIC images, it was found that with cycling, the global strains where the phase transformation starts increased and the delineation of the stress-induced martensitic phase fronts decreased. Cycling appears to result in the establishment of residual pockets of martensite that cause the transformation to become increasingly spatially homogeneous. In order to see how the phase transformation propagates, the velocity of the phase front was examined. Although the top and bottom of a single phase front can propagate at different velocities, the sum of the two velocities remains nominally constant.

In this experiment, a strain similarity in the macroscopic martensite bands was found during both a single cycle and from cycle to cycle. This strain similarity was examined by extracting the strains down the centerline of the gage section from four stages which included: (1) immediately before the martensitic phase front nucleated, (2, 3) during propagation of the front(s), and (4) immediately after the phase transformation completed. These centerline strains were examined during the 1st and 50th cycle. During martensitic transformation (in a single cycle), the accommodated strain in the martensite wake remained constant even as loading increased and the phase front propagated through the gage section, that is, the additional mechanical work was spent in transformation rather than in plastic deformation of the already formed martensite. The strain similarity between cycles 1 and 50 was determined by overlaying the strains down the centerline of the gage section during the (1)-(4) points of transformation described above. The macroscopically martensite region (inside the localized band) exhibited strong cycle-to-cycle strain similarity. This similarity is much stronger in the macroscopically martensite region than in the macroscopically austenite (outside the localized band) region. This indicates that the accommodated strain in the martensite upon initial loading strongly dictates how the martensite will accommodate strain in the subsequent cycles.

Specimens with three different crystallographic texture orientations (RD of the sheet, 45° to RD, and TD of the sheet) cut from the as-received thin sheet NiTi were tested to examine the effects of crystallographic texture on the stress-induced martensitic phase transformation. These tests were performed on the same experimental setup as the previous tests, where displacement controlled cyclic loading was applied up to N=50 at globally applied strain rates of $\dot{\varepsilon}_g = 10^{-4}$,10^{-3}, and 10^{-2} s^{-1}. The crystallographic textures of the specimens were determined by

pole figures and inverse pole figures using X-ray diffraction and orientation density functions (ODF). It was observed that the TD specimen, which had a crystallographic texture (relatively) unfavorably oriented for martensitic transformation, required a higher stress to nucleate (σ_N) and propagate (σ_P) the phase front than the RD and 45° specimens, which had crystallographic textures (relatively) favorably oriented for transformation. However, the difference between the nucleation and propagation stresses (σ_N - σ_P) of the TD specimen was substantially smaller than that of the RD and 45° specimens. This smaller (σ_N - σ_P) of the TD specimen causes the nucleation of a greater number of localized bands in the TD specimen than in the RD and 45° specimens. It was also observed that in the TD specimen, a martensitic band accommodating lower strain propagated through a 'higher strained' austenite matrix during loading.

The cycle-to-cycle strain similarity was affected by crystallographic texture. Correlation coefficients between the centerline strains were calculated to quantitatively examine the degree of similarity between different cycles and its dependence on texture. It was observed that strain similarity evolved with cycling regardless of crystallographic texture and strain rate. This indicates that the dislocation networks and retention of martensite nuclei continued to evolve with cycling in every case, although at a slower rate as cycling progressed. The cycle-to-cycle strain similarity was significantly stronger in the TD specimen than in the RD and 45° specimens. This stronger strain similarity and less strained localized band in the TD specimen could be due to preferentially oriented microscale pockets of austenite transforming to martensite prior to band nucleation. These microscale pockets transforming to martensite through a matrix of heavily constrained grains could then lead to a stronger cycle-to-cycle strain similarity.

Finally, the combined effects of strain rate and cycling on the stress-induced martensitic phase transformation were examined at the globally applied strain rates of $\dot{\varepsilon}_g = 10^{-4}$,10^{-3}, and 10^{-2} s^{-1} . As the applied strain rate increased, more martensitic bands nucleated and the transformation plateau became increasingly inclined, consistent with previous observations by other researchers and due to the accumulation of latent heat. It was verified that the latent heat was released (absorbed) at the phase front during loading (unloading) by overlaying thermal and strain maps. In order to remove the effect of accumulated latent heat from the previous cycle and examine the pure strain rate dependence, additional experiments with a hold time between cycles of 1800 seconds were performed in order to allow for the equilibration of specimen temperature between cycles. The first localized band of the second cycle was found to occurr at or very near to a cold location in the gage section caused by absorbed latent heat from the end of the first cycle. Thus, if the difference of the local temperature is known on the specimen, it is possible to specify the location where transformation will likely initiate.

6.2 Future Work

To this point, this study has focused on examining the effects of displacement-controlled cycling, crystallographic texture, and globally applied strain rates on thin sheet NiTi SMA at the macro-scale. There are many opportunities for future work.

In the crystallographic texture experiments, it was determined that the TD specimen exhibited smaller strains in the localized band (as well as larger strains outside the band) and stronger cycle-to-cycle strain similarity than the more favorably oriented RD and 45° specimens.

It was postulated that the microscale pockets of transformed martensite in heavily constrained grains caused a stronger cycle-to-cycle similarity in the strain. In order to verify this hypothesis and link to the length scale of the microstructure, other microscale in-situ experiments are required. Here are few ideas for future experiments:

- While the specimens (RD, 45°, and TD) are under loading right before the martensitic transformation, we need to examine the crystal orientation and the amount of microscale pockets of transformed martensite.
- While the specimens (RD, 45°, and TD) are in the middle of phase transformation, we need to examine the amount of microscale pockets of austenite in the localized bands and the amount of microscale pockets of martensite outside the bands.
- While the specimens (RD, 45°, and TD) complete the martensitic transformation, we need to examine the amount of microscale pockets of untransformed austenite.
- Whenever the specimens (RD, 45°, and TD) complete a cyclic loading, we need to examine the amount of microscale pockets of residual martensite.

Electron backscatter diffraction (EBSD) and in-SEM strain mapping can be utilized for these experiments, which will provide a stronger understanding of the effect of crystallographic texture on stress-induced martensitic transformation and link the macroscale experiments described in this thesis to quantitative microscale observations.

Examining the impact of cycling, strain rates and crystallographic texture on fracture mechanisms in NiTi is also interesting. In my experiments, the TD specimens were successfully cycled up to 50 cycles at the applied strain rates of $\dot{\varepsilon}_g = 10^{-4}$,10^{-3}, and 10^{-2} s^{-1} in continuous

testing, with no holding applied between cycles. However, at a test applying 1800 seconds of hold between each cycle at an applied strain rate of $\dot{\varepsilon}_g = 10^{-2}\ s^{-1}$, only the TD specimen was found to consistently fracture after approximately 40 cycles. It is hypothesized that the transverse direction to the rolling direction is weaker for the cyclic loading at fast strain rates and the increased stress for phase transformation by the holding time might cause fracture. Thus, fatigue tests with different crystallographic textures and crystallographic texture analysis after cycles near the fractured cycle can be useful to determine the exact reason for the fracture in the SMAs under stress-induced martensitic phase transformation. Thus, applying the effects of cycling, crystallographic texture, strain rates, and the cycle-to-cycle strain similarity by the different crystallographic textures will result in better fatigue performance for many applications.

The crystallographic orientation of Nitinol has a substantial influence on the macroscopic responses including stress for phase transformation, the completion strain of phase transformation, the length of transformation strain and residual strain. The crystallographic orientation also strongly affects material properties in other cold-rolled alloys. In the automotive industry, though the effort to increase efficiency of automotive engines has been continuous, the effort is recently facing the limit of efficiency. Thus, an alternative method can be weight optimization of automotive vehicles to increase the efficiency. For example, if we can reduce the thickness of materials that satisfy the requirement of mechanical properties, such as stiffness, strength, or fatigue life, by changing crystallographic orientation, it will allow for significant weight reduction in the automotive industry. Thus, the examination of crystallographic orientation in other materials, which are used in the commercial automotive industry, would be interesting and practical study.

Taking a step away from academic research, an interesting application of Nitinol is found in my personal favorite sport, tennis. In the two years that I have played tennis, I have seen tennis players, both amateur and professional, suffer from tennis elbow because of repeated impact on their elbow. In order to reduce the risk of tennis elbow, many players are using arm bands to reduce the impact or stretching their elbow carefully before the match. One possible method to reduce the likelihood of tennis elbow is through the use of superelastic Nitinol string on tennis racquets due to its high damping capacity. The application and use of its high damping capacity in seismic devices is shown in chapter 1.2 and how the damping capacity is affected by cycling, strain rate, and accumulated latent heat from previous cycle is examined in chapter 5.2 and 5.3. In addition to the high damping capacity, one reason to change the racquet string due to reduced string tension after a few months. Nitinol wire can solve this problem by heating up above A_f temperature. Thus, there are two advantages using Nitinol string, preventing tennis elbow and regular replacement of racquet string. The use of Nitinol in tennis racquet was patented (publication number: US4909510 A) in 1990 and shortly mentioned by Duerig at NDC in 1995, but it has not been commercialized yet. Thus, after measuring the impact load and displacement, and applied strain rate on the string, commercialization of Nitinol tennis string would be interesting. The challenge on this task will be the superelastic response at high strain rates because the superelastic response disappears at extremely fast strain rates, such as 4200 s^{-1} as described in chapter 1.4.